UNIVERSIDADE FEDERAL DO RIO DE JANEIRO
INSTITUTO DE FÍSICA

Non-equilibrium Phenomena in Thermonuclear Supernovae: from life to death of white dwarf stars

Elvis do Amaral Soares

PhD thesis presented to the Graduate Program in Physics of the Institute of Physics of the Universidade Federal do Rio de Janeiro, as part of the requirements for obtaining the title of Doctor in Sciences (Physics).

Advisor: João R. T. de Mello Neto

Co-advisor: Takeshi Kodama

Rio de Janeiro
May 2017

CIP - Catalogação na Publicação

S676n

Soares, Elvis do Amaral
Non-equilibrium Phenomena in Thermonuclear Supernovae: from life to death of white dwarf stars / Elvis do Amaral Soares. -- Rio de Janeiro, 2017.
138 f.

Orientador: João Ramos Torres de Mello Neto.
Coorientador: Takeshi Kodama.
Tese (doutorado) - Universidade Federal do Rio de Janeiro, Instituto de Física, Programa de Pós Graduação em Física, 2017.

1. white dwarfs. 2. type ia supernovae. 3. non equilibrium thermodynamics. 4. nucleosynthesis. 5. shock waves. I. de Mello Neto, João Ramos Torres, orient. II. Kodama, Takeshi, coorient. III. Título.

Elaborado pelo Sistema de Geração Automática da UFRJ com os dados fornecidos pelo(a) autor(a).

Non-equilibrium Phenomena in Thermonuclear Supernova: from life to death of while dwarf stars

Elvis do Amaral Soares

João Ramos Torres de Melo Neto
Takeshi Kodama

Tese de Doutorado submetida ao Programa de Pós-Graduação em Física, Instituto de Física, da Universidade Federal do Rio de Janeiro – UFRJ, como parte dos requisitos necessários à obtenção do título de Doutor em Ciências (Física).
Aprovada por:

.....
Prof. João Ramos Torres de Melo Neto
(Presidente e Orientador)

.....
Prof. Takeshi Kodama
(Co-Orientador)

.....
Prof. Gabriel Silveira Denicol

.....
Prof. Rodrigo Picanço Negreiros

.....
Prof. Marcelo Chiapparini

.....
Prof. Ribamar Rondon de Rezende dos Reis

.....
Prof. Luca Roberto Augusto Moriconi

Rio de Janeiro, RJ – Brasil
Maio de 2017

Abstract

Non-equilibrium Phenomena in Thermonuclear Supernovae: from life to death of white dwarf stars

Elvis do Amaral Soares

Advisor: João Ramos Torres de Mello Neto
Co-advisor: Takeshi Kodama

Abstract of the Ph.D. Thesis presented to the Graduate Program in Physics of the Institute of Physics of the Federal University of Rio de Janeiro - UFRJ, as part of the requirements to the obtention of the title of Doctor in Sciences (Physics).

In this thesis we investigate some non-equilibrium phenomena in the dynamics of evolutional stages of white dwarfs, such as cooling and Type Ia supernova explosions.

The first part of the thesis is dedicated to introduction of the general concept of non-equilibrium thermodynamics, and its application in describing transient phenomena in systems near-equilibrium which are very common in Nature. In particular, we present the context of astrophysical systems focusing on the physical ingredients present inside white dwarf stars, which are the progenitors of type Ia supernovae.

In the second part of the thesis, we deal with white dwarf stars, more precisely their thermal evolution as a stationary state of thermodynamics. Since the nuclear fusion processes have been ceased in these stars, their thermal energy stored during the period as proto-white dwarf is the only source of their luminosity as an almost steady energy from the core region to the surface. In this thesis, we introduce a very simple model for such a process of white dwarfs cooling, and derive a simple analytic expression which constrains their radii, masses and effective temperatures, as they cool.

The third and final part of the thesis is devoted to the study of retardation effects on hydrodynamic calculations, more precisely on the delayed thermalization of the smallest fluid element considered numerically. Below the length scale defined by this element of fluid, transient phenomena are ignored by many numerical calculations. This thesis is dedicated mainly to the improvement of some numerical

methods used for the simulation of thermonuclear supernovas, taking into account a simplified model of the retardation effects coming from transient processes, well described by non-equilibrium thermodynamics. We have verified that the delayed thermalization effects in the material can be determined by its signatures on the supernova observables, such as nucleosynthesis and energy released during the explosion.

Keywords: white dwarfs - supernovae: general - shock waves - nuclear reactions, nucleosynthesis, abundances - hydrodynamics.

Resumo

Fenômenos Fora-do-Equilíbrio em Supernovas Termonucleares: da vida à morte de estrelas anãs brancas

Elvis do Amaral Soares

Orientador: João Ramos Torres de Mello Neto
Co-orientador: Takeshi Kodama

Resumo da Tese de Doutorado apresentada ao Programa de Pós-Graduação em Física do Instituto de Física da Universidade Federal do Rio de Janeiro - UFRJ, como parte dos requisitos necessários à obtenção do título de Doutor em Ciências (Física).

Nesta tese investigamos alguns fenômenos fora-do-equilíbrio na dinâmica dos estágios evolutivos de anãs brancas, tais como resfriamento e explosões de supernovas do Tipo Ia.

A primeira parte da tese é dedicada à introdução do conceito geral de termodinâmica fora-do-equilíbrio, e sua aplicação na descrição de fenômenos transientes em sistemas próximos ao equilíbrio que são bem comuns na Natureza. Em particular, apresentamos o contexto de sistemas astrofísicos focando nos ingredientes físicos presentes no interior de estrelas do tipo anã branca, que são os progenitores de supernovas do tipo Ia.

Na segunda parte da tese tratamos de estrelas anãs brancas, mais precisamente sua evolução térmica como um estado termodinâmico estacionário. Uma vez que os processos de fusão nuclear foram extintos nessas estrelas, sua energia térmica armazenada durante o período como proto-anã branca é a única fonte de luminosidade como um fluxo estacionário de energia da região central até a superfície. Nessa tese introduzimos um modelo bem simples para tal processo de resfriamento de anãs brancas e, obtemos uma expressão analítica simples que vincula seus raio, massa e temperatura efetiva, conforme elas esfriam.

A terceira e última parte da tese é dedicada ao estudo de efeitos de retardamento em cálculos hidrodinâmicos, mais precisamente na termalização atrasada do menor elemento de fluido descrito numericamente. Abaixo da escala de comprimento definida por esse elemento de fluido, os fenômenos transientes são ignorados

por muitos cálculos numéricos. Essa tese é dedicada principalmente ao aprimoramento de alguns métodos numéricos utilizados para a simulação de supernovas termonucleares, levando em conta um modelo simplificado dos efeitos provenientes de processos transientes pensando-os como fenômenos descritos a partir da termodinâmica fora-do-equilíbrio. Verificamos que os efeitos da termalização atrasada do material podem ser determinados através de suas assinaturas nos observáveis, como nucleossíntese e energia liberada na explosão.

Palavras-chave: anãs brancas - supernovae: geral - ondas de choque - reações nucleares, nucleossíntese, abundâncias - hidrodinâmica.

In memoriam of a dear cousin,
João Alfredo Neto.

Acknowledgments

This work is the result of 5 years of hard and enjoyable work, sometimes more hard than enjoyable. Therefore, the outcome express in this thesis could not be accomplished without the help and support of many people that made the way as pleasant as possible. So, I thank everyone who was part of this wonderful and challenging journey.

First of all, I would like to thank all my friends and family that got me up to this point in my life. I acknowledge my parents Maria da Conceição and João Neto for all their effort and incentives to always be the best of myself. Furthermore, I thank my brothers João Henrique and Diogo for his friendship and companionship.

I am grateful to Prof. João Torres and Prof. Takeshi Kodama who guided me throughout the whole Ph.D. I really appreciated the almost 9 years of work with Prof. João, since my undergraduation. He has been my advisor since I was 18 years old, so I could learn many subjects of life and work with him. I thank to Prof. Kodama whose the first contact was before I went to UFRJ, when I saw a beautiful but 'heavy' talk about quark-gluon plasma at National Observatory when I was 16 and was the High School. But everything changed when I was able to attend a lecture of Nuclear and Particle Physics, which was so extraordinary that made me think about the direction my career should take. I thank to the ICE group professors, as Eduardo Fraga, Carla Bonifazi, Tomoi Koide for make the discussion environment more friendly. Not forgetting, I appreciate the freedom that my advisors gave me during the Ph.D research to study and to reflect about any subject that I was interested.

I thank to my friends and officemates Maurício Hippert, Daniel Kroff, José Jimenez for interesting discussions about almost everything in physics and other subjects. Beyond them, I am glad for meeting friends like Anderson Kendi, Tiago Mendes, Márcio Taddei, Daniel Niemeyer, Carlos Zarro, Michael Moraes, Pedro Malta, Tarik Cysne, whose all nonsense and distractive conversations will be forever remembered.

I acknowledge the Graduation Secretariat Carlos José and Pedro Ribeiro for working out all kind of bureaucracy involved in the process of obtaining the Ph.D. in Sciences degree. I thank the funding agencies that have partially supported this Ph.D. work and other essential support, CNPq (Brazilian National Council for Scientific

and Technological Development) and FAPERJ (Foundation for Research Support of the State of Rio de Janeiro).

Finally, I acknowledge everyone who I forgot the name, have seen sometimes, but that important to this realization. I'm sure I do not know all those who helped me get to this moment, however, I believe it's important to thank them anyway.

Twinkle, twinkle, quasi-star
Biggest puzzle from afar
How unlike the other ones
Brighter than a billion suns
Twinkle, twinkle, quasi-star
How I wonder what you are.
– George Gamow

Contents

Contents xv

List of Figures xix

List of Tables xxv

List of Symbols xxvii

1 Prologue 1

1.1 The Life of White Dwarfs . . . 1

1.1.1 Formation . . . 1

1.1.2 Degenerate Matter . . . 2

1.1.3 Mass–radius relation and the Chandrasekhar Limit . . . 2

1.1.4 Cooling . . . 5

1.1.5 Spectra and Classification . . . 7

1.1.6 Binary systems . . . 8

1.2 The Death in a Type Ia Supernova . . . 9

1.2.1 Light Curves and Standardized Candles . . . 9

1.2.2 Nucleosynthesis and Spectra . . . 10

1.2.3 Progenitor scenario . . . 12

1.2.4 Energetics of the Explosion . . . 12

1.2.5 The state-of-art of Thermonuclear Explosions . . . 14

1.3 Objectives of this work . . . 15

1.4 Organization of this thesis . . . 15

2 Non-equilibrium Thermodynamics 17

2.1 Local Thermodynamic Equilibrium Hypothesis . . . 17

2.2 Conservation Laws . . . 19

2.2.1 Viscous and Heat-Conducting Fluids . . . 20

2.2.2 Reactive Fluids . . . 21

2.3 Entropy Production . . . 23

2.3.1 Entropy Production in Viscous, Heat-Conducting and Reactive Fluids . . . 23
2.3.2 Linear Phenomenological Coefficients . . . 25
2.4 Non-equilibrium Stationary States . . . 26
2.4.1 Mechanical Equilibrium . . . 26
2.4.2 Thermal Stationary State . . . 27
2.5 Relaxation from Near-Equilibrium States . . . 27
2.5.1 Motivation . . . 27
2.5.2 Relaxation Kernel . . . 28
2.6 Final Considerations . . . 29

3 Astrophysical Contents **31**
3.1 Equation of state: How to hold the star? . . . 31
3.1.1 Radiation gas . . . 32
3.1.2 Ionized ideal gas . . . 32
3.1.3 Semi-degenerate fermion gas . . . 32
3.2 Opacities: How does heat propagate? . . . 35
3.2.1 Radiation Opacity . . . 37
3.2.2 Conductive Opacities . . . 38
3.3 Thermonuclear Reactions: How to burn the material and change the chemical composition? . . . 39
3.3.1 Fusion Reactions . . . 40
3.3.2 Photo-disintegration Reactions . . . 41
3.3.3 Abundance Evolution and Energy Generation . . . 42
3.3.4 Thermonuclear reaction rate . . . 43
3.3.5 Nuclear Reaction Network . . . 46
3.3.6 Nuclear Statistical Equilibrium . . . 47
3.4 Gravitational Force . . . 49

4 Numerical Details **51**
4.1 One-dimensional Fluid dynamics . . . 51
4.1.1 Effective Lagrangian Description . . . 51
4.2 Artificial Viscosity . . . 57
4.3 Equation of state . . . 57
4.4 Luminosity and Opacities . . . 58
4.5 Thermonuclear reactions . . . 59
4.6 Integration and Timestepping . . . 61
4.6.1 The Runge-Kutta-Fehlberg Integrator . . . 61
4.6.2 Timestepping Criteria . . . 62
4.7 Code Validation and Verification . . . 64

4.7.1 Free fall collapse . . . 64
4.7.2 Sod's Shock Wave Problem . . . 64
4.7.3 Explosive Nuclear Burning . . . 67

5 Stationary Cooling of White Dwarfs 69
5.1 Extended Model for Outer Radiative Layers of White Dwarfs . . . 70
5.1.1 Data Set and Procedure . . . 72
5.1.2 DA white dwarfs . . . 72
5.1.3 DB white dwarfs . . . 73
5.2 Semi-Empirical Mass-Radius Relation . . . 74
5.2.1 Effective Temperature Limit . . . 77
5.3 Central Temperature and Nuclear Ignition in White Dwarfs . . . 79
5.4 Estimating Masses of Hot White Dwarfs . . . 82
5.5 Discussion and Conclusion . . . 83

6 Delayed Thermalization in Thermonuclear Supernovae 85
6.1 Retardation Effects in Hydrodynamical Calculations . . . 86
6.2 sub-Chandrasekhar Supernovae . . . 88
6.2.1 Effects on the shock wave propagration . . . 88
6.2.2 Effects on the energetics of explosion and nucleosynthesis . . . 92
6.3 Discussion and Conclusion . . . 95

7 Epilogue 99

Bibliography 101

A Semi-degenerate Equation of State 121
A.1 Evaluation of the $F_k(\eta, \beta)$ . . . 121
A.1.1 Large degeneracy ($\eta \gg 1$), arbitrarily relativistic (arbitrary β) 122
A.1.2 Small degeneracy ($\eta \leq 0$), arbitrarily relativistic (arbitrary β) . 125
A.1.3 Arbitrarily degenerate and arbitrarily relativistic . . . 127
A.2 Helmholtz Equation of State . . . 127
A.2.1 Quintic Hermite Interpolation . . . 127
A.2.2 Bi-quintic Hermite Interpolation . . . 129
A.2.3 Helmholtz free energy interpolation . . . 130
A.3 Thermodynamic Quantities . . . 132

List of Figures

1.1 Distribution of the DA-WD (*blue circles*) and DB-WD (*yellow squares*) data in the mass and radius plane. The solid (*red*) line corresponds to the analytical approximation (1.14) of the ideal WD mass-radius relation with a pure carbon composition. The data are taken from Ref.[10]. 6

1.2 Author's artistic representation of the stellar structure of white dwarfs with the spectral type DA, DB, DZ and DQ. 8

1.3 Comparison of the bolometric luminosity from the analytic model by Arnett [42] (*orange solid line*) and the SN2011fe data [43] (*blue circles*). 10

1.4 Spectrophotometry of SN 2011fe. Major ion signatures in the first two spectra are shown. The early and near-maximum spectra exhibit typical strong low- to-intermediate-mass ion signatures (O I, Mg II, Si II, S II, Ca II) at typical SN Ia ejection velocities. Two weeks after maximum, the spectrum is dominated by numerous blends from iron-peak elements (Fe II, Co II) blueward of about 5000 $\AA$. The days at right represent the time since the maximum in the light curve. Reproduced from [43]. 11

1.5 Possible models of SN I in a single-degenerate scenario, depending on the initial CO WD mass ($M_{\mathrm{C+O}}$) and on the accretion rate helium-rich material from the companion ($\dot{M}$). Figure reproduced from [57]. 13

3.1 **(a)** The occupation number q for electrons as a function of $x = \epsilon/k_B T$. **(b)** The distribution function $n_e(p)$ for great degeneracy (*red line*) and for a complete degeneracy (*darker line*). 33

3.2 Mapping of degenerate phases and relativistic regimes for an electron gas. 34

3.3 The total opacity κ_{tot} (*red solid line*) as a function of density ρ for temperature $T = 10^8$ K and pure carbon composition. The radiative κ_{rad} (*blue dashed line*) and conductive κ_{cond} (*orange dashed line*) opacity are represented as reference. 37

3.4 The electron thermal conductivity λ_e as a function of density ρ for different values of temperature T. 40

3.5 **(a)** The factor $(kT)^{-3/2}Ee^{-E/kT}$ in the expression (3.38) for fusion reaction rate at three different temperatures, $T = 1.5 \times 10^7$ K (*yellow line*), $T = 3 \times 10^8$ K (*orange line*) and $T = 1 \times 10^9$ K (*blue line*). **(b)** The factor $E^2/(e^{E/k_BT} - 1)$ in the expression (3.40) for the photo-disintegration reactions rate at three different temperatures, $T = 1 \times 10^9$ K (*blue line*), 2.5×10^9 K (*orange line*), and 5×10^9 K (*yellow line*). 41

3.6 **(a)** The Maxwell-Boltzmann factor e^{-E/k_BT} (*green line*) and the Gamow tunneling factor $e^{-bE^{-1/2}}$ (*blue line*) versus energy for the reaction $^{12}C(\alpha,\gamma)^{16}O$ at $T = 2 \times 10^8$ K. The Gamow's peak product $e^{-E/k_BT}.e^{-bE^{-1/2}}$ (*red line*) is also represented. **(b)** The Gamow peak for the reaction $C^{12}(\alpha,\gamma)O^{16}$ at $T = 0.2$ GK. The curve (*blue dashed line*) is asymmetric about E_0, but it is adequately approximated by a Gaussian (*red solid line*). The width of the Gaussian is presented by Δ. 44

3.7 The mass fractions under nuclear statistical equilibrium as a function of temperature for different values of density. The point here is that, with rising temperatures at a given density, or with decreasing densities at a given temperature, an increasing fraction of the composition resides in light particles and that this transformation absorbs a large amount of energy. 48

4.1 Representation of stellar interior using shells. The radii R_i and R_{i-1} are the outer and inner radius of the shell, respectively. 52

4.2 **(a)** Simulation of the free-fall collapse of a homogeneous sphere. Note the agreement between the analytical solution (*red line*) and the numerical results (*blue points*). Simulation performed with the *ELcode*, with $N = 100$ shells. **(b)** Evolution of the central density as a function of time for the free-fall collapse. **(c)** Density profile versus radius for the free-fall collapse. The blue dashed line represents the relation $\rho \propto R^{-3}$ to the outer shell. 65

4.3 **(a)** Density profiles at times t = 0, 0.125, and 0.25 s, in Sod's shock wave problem, using *ELcode* with 1000 shells. **(b)** Pressure profiles. **(c)** Velocity profiles. 66

4.4 **(a)** Evolution of the mass fractions under adiabatic expansion using the *iso7* reaction network. The initial conditions are $T = 3 \times 10^9$ K and $\rho = 1 \times 10^8$ g cm^{-3} with a pure ^{4}He composition. The sum of the intermediate-mass fractions are plotted as silicon-group [^{28}Si], and the sum of the nickel-mass fractions are plotted as nickel-group [^{56}Ni]. **(b)** The energy generation rate under adiabatic expansion. Helium burning under these conditions is exothermic. 67

4.5 **(a)** Evolution of the mass fractions under adiabatic expansion using the *iso7* reaction network. The initial conditions are $T = 3 \times 10^9$ K and $\rho = 1 \times 10^9$ g cm^{-3} with a mixture half ^{12}C-half ^{16}O composition. **(b)** The energy generation rate under adiabatic expansion. Carbon-oxygen burning under these conditions is exothermic. 68

4.6 **(a)** Evolution of the mass fractions under adiabatic expansion using the *iso7* reaction network. The initial conditions are $T = 5 \times 10^9$ K and $\rho = 1 \times 10^9$ g cm^{-3} with a pure ^{28}Si composition. **(b)** The energy generation rate under adiabatic expansion. Silicon burning under these conditions is endothermic before $t \sim 10^{-5}$ s and exothermic afterward. The transition point is marked with the black vertical line. 68

5.1 Parameters μ and ξ as a function of mass for DA-WD. The top panel shows two references for μ as dotted lines, a pure ionized He gas and a pure ionized H gas. In the bottom panel we represent the case where $R_{\rm eff} = R_{\rm ch}$ as dotted line. 73

5.2 Semi-empirical radius-effective temperature relation for DA-WD with different masses. The orange circles represent some values of mass and the blue lines are their correspondent fits. The light gray circles are the available data for DA-WD from the SDSS-DR7. 74

5.3 Parameters μ and ξ as a function of mass for DB-WD. The top panel shows two references for μ as dotted lines, a pure ionized He gas and a pure ionized H gas. In the bottom panel we represent the case where $R_{\rm eff} = R_{\rm ch}$ as dotted line. 75

5.4 Semi-empirical radius-effective temperature relation for DB-WD with different masses. The red circles represent some values of mass and the green lines are their correspondent fits. The light gray circles are the available data for DB-WD from the SDSS-DR7. 75

5.5 Semi-empirical mass-radius relation for DA-WD with different effective temperatures. The orange circles represent some values of effective temperature and the blue lines are their correspondent fits. The light gray circles are the available data for DA-WD from the SDSS-DR7. The dashed line corresponds to the Chandrasekhar model for ideal white dwarfs stars. 77

5.6 Semi-empirical mass-radius relation for DB-WD with different effective temperatures. The red circles represent some values of effective temperature and the green lines are their correspondent fits. The light gray circles are the available data for DB-WD from the SDSS-DR7. The dashed line corresponds to the Chandrasekhar model for ideal white dwarfs stars. 78

5.7 Semi-empirical mass-radius relation for DA-WD with different effective temperatures (blue lines). The purple solid circles correspond to the directly observed DA-WD and the yellow open circles are the DA-WD observed in wide binaries from the *Gaia* DR1. The dashed line is the Chandrasekhar mass-radius relation for ideal WD. 79

5.8 Effective temperature limit as a function of mass for DA-WD (blue line). The blue region represents the forbidden region of the effective temperature to the correspondent mass of DA-WD. The light gray circles are the available data for DA-WD from the SDSS-DR7. The dot line corresponds to the temperature threshold for ideal white dwarfs stars. 80

5.9 Central temperature as a function of the effective temperature for DA-WD with different masses (blue lines). The gray circles represent the central temperature to each DA-WD star in the available data from the SDSS-DR7, and the orange circles are the highest central temperature for WD from these data. The dashed lines are the ignition curves for carbon and oxygen fusions. The dotted line is our effective temperature threshold for hot white dwarfs. 81

6.1 The generated heat as a function of time. The original distribution is a Gaussian centered at 0.4 s with width 0.03 s, represented as the dashed blue line. The orange and yellow lines represent the delayed distributions with $\tau = 100$ ms and $\tau = 200$ ms, respectively. 88

6.2 Propagation of the double detonation waves *(dashed lines)* and the corresponding changes of the radial coordinates of the Lagrangian shells *(solid lines)* as a function of time without time delay ($\tau = 0$ ms). The blue lines represent the helium accreted shells and the orange lines represent the CO core. 90
6.3 Propagation of the double detonation waves *(dashed lines)* and the corresponding changes of the radial coordinates of the Lagrangian shells *(solid lines)* as a function of time for time delay $\tau = 2$ ms. The color scale is the same as Figure 6.2. 90
6.4 The temperature, pressure and radial velocity profiles at time (1) t = 0, (2) t = 92 ms, (3) t = 151 ms, (4) t = 201 ms, (5) t = 280 ms without time delay ($\tau = 0$). 91
6.5 Propagation of the double detonation waves *(dashed lines)* and the corresponding changes of the radial coordinates of the Lagrangian shells *(solid lines)* as a function of time for time delay $\tau = 4$ ms. The red circle represents the Lagrangian shell $M(r) = 1.0\ M_{\odot}$ where the detonation ceases. The shock wave *(light dotted line)* which propagates inward into the CO core is not able to induce a carbon detonation. The color scale is the same as Figure 6.2. 92
6.6 The temperature, pressure and radial velocity profiles at time (1) t = 0, (2) t = 120 ms, (3) t = 233 ms, (4) t = 333 ms, (5) t = 495 ms with time delay $\tau = 4$ ms. 93
6.7 The final mass fractions of the seven isotopes for different values of time delay parameter τ. 94
6.8 The mass fractions of silicon-group elements (*blue solid line*) and nickel-group elements (*red solid line*) and the nuclear energy released during the explosion (*orange dashed line*) versus the delay time parameter τ. The dotted line represents the binding energy. 96

A.1 Pressure as a function of density for different temperatures and a pure ^{12}C composition. 132
A.2 Internal energy per unit mass as a function of density for different temperatures and a pure ^{12}C composition. 133
A.3 Entropy per unit mass as a function of density for different temperatures and a pure ^{12}C composition. 133
A.4 Partial derivative of the pressure with respect to the density for different constant values of temperature. 134
A.5 Partial derivative of the pressure with respect to the temperature for different constant values of density. 134

A.6 Partial derivative of the specific internal energy with respect to the density for different constant values of temperature 135
A.7 Partial derivative of the specific internal energy with respect to the temperature for different constant values of density. 135
A.8 Numerical deviation of the thermodynamic relation $P = \rho^2 \partial u/\partial \rho + T\partial p/\partial T$. The smaller the deviation, with zero deviation being the perfect case, the closer the equation of state comes to satisfying thermodynamic consistency. 136
A.9 Numerical deviation of the thermodynamic relation $\partial u/\partial T = T\partial s/\partial T$. 137
A.10 Numerical deviation of the thermodynamic relation $\partial s/\partial \rho = -\rho^{-2}\partial p/\partial T$.138

List of Tables

5.1 The estimated radii for the observed DA white dwarf stars from Eclipsing Binaries. 78
5.2 The highest estimated central temperature determined for the observed DA white dwarf stars from *SDSS*-DR7. 82
5.3 The estimated masses for the directly observed DA white dwarf stars from the *Gaia*-DR1. 83

6.1 Nucleosynthetic yields of selected species and nickel radial velocity for different values of the time delay parameter τ. 95
6.2 Energetics of explosion for different values of the time delay parameter τ. 95

List of Symbols

Physics Constants (CODATA)

a	Radiation density constant	7.5646×10^{-15} erg cm^{-3} K^{-4}
c	Speed of light in a vacuum	$2.99792458 \times 10^{10}$ cm s^{-1}
e	Elementary charge	$4.8032068 \times 10^{-10}$ esu
G	Gravitational constant	$6.67259(85) \times 10^{-8}$ cm^3 g^{-1} s^{-2}
h	Planck's constant	$6.6260755(40) \times 10^{-27}$ erg s
k_B	Boltzmann's constant	$1.380658(12) \times 10^{-16}$ erg K^{-1}
m_e	Mass of electron	$9.1093897(54) \times 10^{-28}$ g
N_A	Avogadro's number	6.0221367×10^{23} mol^{-1}

Common Abbreviations

$\odot$	solar
$\oplus$	earth
$M_{\rm Ch}$	Chandrasekhar's mass limit
LTE	Local Thermodynamic Equilibrium
SNe Ia	Type Ia Supernovae
WD	White Dwarf

Other Symbols

$\epsilon_{\rm nuc}$	nuclear energy generation rate per unit mass
κ	opacity
$\tau_{\rm dyn}$	dynamical timescale

τ_{nuc}	nuclear burning timescale
c_p	specific heat at constant pressure
c_s	speed of sound
c_v	specific heat at constant volume
L	luminosity
${}^{A}\text{Z}$	isotope Z with number mass A

Chapter 1

Prologue

Stars have a life cycle much like animals. They get born, they grow, they go through a definite internal development, and finally they die, to give back the material of which they are made so that new stars may live.

– Hans Bethe (1906-2005)

1.1 The Life of White Dwarfs

The vast majority (of the order of 90%, see [1]) of all stars in our galaxy, including our sun, will evolve toward the final state of a white dwarf. Many of them are members of binary systems, being able to capture appreciable amounts of matter from their companions. The accreting matter process leads to the compression and heating of the ingoing material, and its ignition can lead to a beautiful and violent explosion, the Type Ia supernova.

1.1.1 Formation

After the hydrogen-burning period of a main-sequence (MS) star with masses from about 0.07 to 11 $M_{\odot}$ [2], such a star will expand to a red giant during helium (He) burning to carbon (C) and oxygen (O) in its core by the two-step triple-alpha fusion process. If the red giant has insufficient mass to achieve the core temperatures around 10^9 K required to carbon fusion, an inert core of carbon and oxygen will build up at its center. After such a star ejects off its outer layers forming a planetary nebula, it will leave behind the core, i.e., the remnant white dwarf (WD)) [e.g., 3]. If the mass of the progenitor is between 8-11 $M_{\odot}$, the core temperature will be

sufficient to fuse carbon but not neon, forging an oxygen–neon–magnesium white dwarf [4]. Stars of very low mass will not be able to burn helium, hence, a helium white dwarf [5] may form by mass loss in binary systems.

1.1.2 Degenerate Matter

Although the material in a white dwarf still keeps very high temperature, it is not enough to provoke the fusion reactions of heavy elements such as C and O, so the star has no source of energy. As a result, it cannot keep the quasi-stationary hydrostatic equilibrium through the balance of the energy production of thermonuclear reactions and cools down slowly due to the energy loss as luminosity (see Section 1.1.4). As a consequence, the gravitational collapse advances, until the pressure of high electron density due to the Pauli principle becomes dominant. In fact, an Earth-sized white dwarf with Sun mass has a density of the order of 10^6 g/cm^3 while the Earth itself has an average density of only 5.4 g/cm^3. That means a white dwarf is a million times denser than Earth and can be supported only by electron degeneracy pressure, as first resolved by Fowler [6].

Under high densities and/or temperature, the matter becomes a completely ionized gas when the electrons are all forced to be apart from their parent atoms. For instance, in the core of a WD there is a collection of positively charged ions, largely carbon and oxygen nuclei, surrounded by an electron sea. In a relatively low density and very high temperature, ionized gas thermal motions of the electrons (which move faster than the ions, and hence collide more frequently) provide the pressure support, because most of the available electron energy levels are unfilled and the electrons are free to switch from one energy state to another. But as the density increases, the lower levels of electrons start to be fulfilled and the remaining electrons are forced to occupy states of higher energy than the thermal kinetic energy, due to the Pauli's exclusion principle[1]. Such states of a fermion gas are called *degenerated*. Increasing the density, the electron gas becomes strongly degenerate and produce the pressure against compression because when compressed, the energy levels of occupied states becomes higher. Hence the high momentum electrons contribute to increase the internal pressure, known as degeneracy pressure. The degeneracy pressure is the reason why white dwarfs are also called degenerate stars.

1.1.3 Mass–radius relation and the Chandrasekhar Limit

The gravity force and the degeneracy pressure can keep a white dwarf stable forever. This hydrostatic equilibrium state may exist for billions of years. To illustrate

[1] Two fermions cannot exist in identical quantum energy state.

the fundamental problem of obtaining the equilibrium configuration of a WD star, we can calculate the mass-radius relation based on a dimensional argument [7]. Let consider a white dwarf of mass M and radius R composed only by a degenerate electron gas. We approximate the internal energy U by the form

$$U = m_e c^2 N \left\{ \left[\left(\frac{p}{m_e c} \right)^2 + 1 \right]^{1/2} - 1 \right\} \tag{1.1}$$

where p is an average momentum over the star electrons, and N is the total number of electrons, such that this internal energy can be associated to the relativistic Fermi energy if p is related to the Fermi momentum. In fact, we can associate this average momentum to the appropriate average electron density n_e according to

$$p = \hbar (3\pi^2 n_e)^{1/3}, \tag{1.2}$$

and

$$n_e = \zeta N / R^3, \tag{1.3}$$

where ζ is a dimensionless parameter. If n_e corresponded to the mean electron density in whole star, we would expect $\zeta = 3/4\pi$, but we shall leave its value undetermined at this point.

The gravitational potential energy can be written as

$$\Omega = -\nu \frac{GM^2}{R}, \tag{1.4}$$

where ν is a second dimensionless parameter. For a homogeneous sphere, as is well-known, $\nu = 3/5$. We can introduce two new dimensionless variables n and r, such that $N = nN_0$ and $R = rR_0$, with the requirement that the relativity parameter $x = p/m_e c$ have the form $x = n^{1/3}/r$ and that the potential energy have the form $\Omega = -m_e c^2 N_0 n^2 / r$, so that

$$N_0 = \frac{(3\pi^2\zeta)^{1/2}}{\nu^{3/2}} \left(\frac{\hbar c}{G m^2} \right)^{3/2} \tag{1.5}$$

and

$$R_0 = (3\pi^2\zeta)^{1/3} \left(\frac{\hbar}{m_e c} \right) N_0^{1/3}. \tag{1.6}$$

where $m = M/N = m_u \mu_e$, m_u is the atomic unit mass and μ_e the mean molecular

weight per electron. The total energy, $E = U + \Omega$, now takes the form

$$E = m_e c^2 n N_0 \left\{ \left[\left(\frac{n^{2/3}}{r} + 1 \right) \right]^{1/2} - 1 - \frac{n}{r} \right\}. \tag{1.7}$$

In terms of these variables the variational principle requires that the partial derivative $\partial E/\partial r$ must vanish, for low temperatures approximation ($T \sim 0$). Hence we obtain

$$r = \frac{(1 - n^{4/3})^{1/2}}{n^{1/3}}. \tag{1.8}$$

For small values of n, corresponding to non-relativistic electrons, (1.8) reduces to

$$\lim_{p \ll m_e c} R M^{1/3} = \frac{(3\pi^2 \zeta)^{2/3}}{\nu} \left(\frac{\hbar}{m_e c} \right) \left(\frac{\hbar c}{G m^2} \right) m^{1/3}, \tag{1.9}$$

which is the analytical form of the exact solution of the Lane-Emden equation[2] with polytropic index 3/2, where

$$\frac{(3\pi^2 \zeta)^{2/3}}{\nu} = \frac{1}{2} \left(\frac{3\pi}{4} \right)^{2/3} \xi_1^{5/3} \left(\frac{\mathrm{d}\theta_{3/2}}{d\xi} \right)_{\xi_1}^{1/3} = 4.512. \tag{1.10}$$

This implies that when the mass M increases the radius R decreases to keep the star in hydrostatic equilibrium, with the total energy (1.7) negative. However for large M, the gravitational potential energy becomes more relevant than the internal energy and E decreases without bound at the same time as R decreases. No equilibrium exists, and gravitational collapse sets in. So, there is a mass limit value at which equilibrium is maintained with total energy $E = 0$ and R goes to zero. This situation corresponds to electrons in the extreme relativistic limit, with $n = 1$ and $r = 0$, resulting in a maximum mass M of

$$\lim_{p \gg m_e c} M = \frac{(3\pi^2 \zeta)^{1/2}}{\nu^{3/2}} \left(\frac{\hbar c}{G m^2} \right)^{3/2} m, \tag{1.11}$$

which can also be related to the exact solution of the Lane-Emden equation now

[2]The Lane–Emden equations describe self-graviting spherical polytropes in hydrostatic equilibrium as simple models of stars. The Lane-Emden equations combine the polytropic equation of state and the equation of hydrostatic equilibrium in a simplest form written as

$$\frac{1}{\xi^2} \frac{\mathrm{d}}{\mathrm{d}\xi} \left(\xi^2 \frac{\mathrm{d}\theta}{\mathrm{d}\xi} \right) + \theta^n = 0,$$

which, in the general case, must be solved numerically for each polytropic index n.

with polytropic index 3, where

$$\frac{(3\pi^2\zeta)^{1/2}}{\nu^{3/2}} = \left(\frac{3\pi}{4}\right)^{1/2} \left(-\xi_1^2 \left.\frac{\mathrm{d}\theta_3}{d\xi}\right|_{\xi_1}\right) = 3.098. \tag{1.12}$$

Solving equations (1.10) and (1.12) to obtain the best approximation for ζ and ν, we get

$$\zeta = 0.323 \quad \text{and} \quad \nu = 1.00. \tag{1.13}$$

Substituting these values for ν and ζ in equations, we obtain the mass-radius relation for ideal white dwarfs

$$R = \frac{2.45354}{\mu_e} \left(\frac{M}{M_{\mathrm{ch}}}\right)^{-1/3} \left[1 - \left(\frac{M}{M_{\mathrm{ch}}}\right)^{4/3}\right]^{1/2} R_{\oplus} \tag{1.14}$$

and the *Chandrasekhar's limit* [8] for the mass of ideal white dwarfs[3]

$$M_{\mathrm{Ch}} = \left(\frac{2}{\mu_e}\right)^2 1.459\ M_{\odot} \tag{1.15}$$

If the $M \leq M_{\mathrm{Ch}}$ the white dwarf gravity can be supported by the relativistic electron pressure, but for $M > M_{\mathrm{Ch}}$ the white dwarf collapses into itself. If we compare the obtained radius R from (1.14) with the numerical values obtained by Chandrasekhar [9, Chapter 11], the agreement is excellent and the correction is under 10%. The Figure 1.1 presents the Eq.(1.14) and it is compared to the DA-WD and DB-WD data from the Data Release 7 of Sloan Digital Sky Survey [10], with DA and DB indicating their spectral type, which is described in Section 1.1.5.

Many works have been developed since the discovery of the Chandrasekhar's mass limit [8] in the field of finite temperature corrections to the degenerate equation of state (EoS) [e.g., 11, 12, 13]. However empirical mass-radius relations obtained from the spectroscopic or photometric measurements of masses and radii are still needed and used to understand the structure and the cooling dynamics of WDs.

1.1.4 Cooling

A white dwarf is very hot when it forms with core temperature (T_c) from 10^8 K to 10^9 K being more luminous than the Sun although 100 times smaller, but without no nuclear energy generation it will gradually radiate its energy over 5 to 10 billion years like a blackbody. This means that the emitting radiation, which initially has a high color temperature (white), will lessen and redden with time. Over a very long

[3] For the white dwarf structure and the limiting mass from the Chandrasekhar's theory, we suggest the [3, § 37.1] and the [9, Chapter 11].

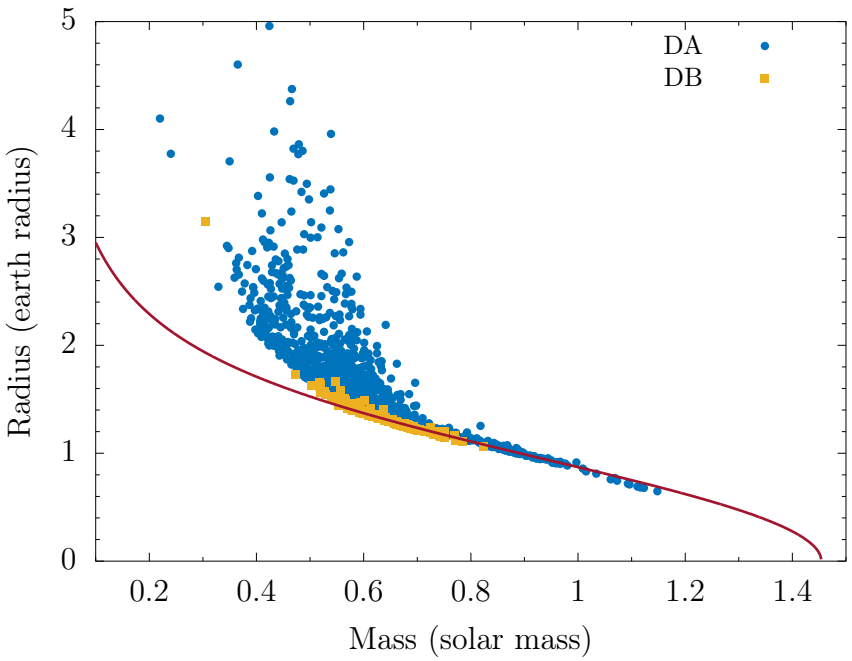

Figure 1.1: Distribution of the DA-WD (*blue circles*) and DB-WD (*yellow squares*) data in the mass and radius plane. The solid (*red*) line corresponds to the analytical approximation (1.14) of the ideal WD mass-radius relation with a pure carbon composition. The data are taken from Ref.[10].

time, a white dwarf will cool and its material will begin to crystallize the core. The star's low temperature means it will no longer emit significant heat or light, and it will become a cold black dwarf into the darkness. Because the length of time it takes for a white dwarf to reach this state is calculated to be longer than the current age of the universe (approximately 13.8 billion years [14]), it is thought that no black dwarfs yet exist [15]. The oldest white dwarfs still radiate at temperatures of a few thousand kelvins.

The zero temperature approximation of highly degenerate electron gas pressure provides an adequate description of the stellar structure as a whole since the kinetic energy associated with the Fermi momentum is dominant compared to the thermal energy in the bulk domain. While the area close to the surface (outer layers) has considerable high effective temperature T_{eff} (from 5,000 K to over 100,000 K) and commands the thermal evolution of the whole white dwarf. The bulk degenerate electrons have high thermal conductivity and keep the star's core essentially isothermal, but the radiative opacity in the outer layers prevents the white dwarf to cool quickly. This mechanism is similar to the cooking with a clay pot: the cooking food is almost isothermal and the clay wall difficults the heat transfer to the outside world.

The hotter outer layers behave like an ideal gas and stretch the WD radius. This

mechanism is more relevant as lower is the WD mass, as we can see for the hot DA and DB WDs in Figure 1.1, which are classes of WDs. The cooling physics of white dwarfs can be found in many textbooks as Shapiro and Teukolsky [16, Chapter 4] or in a very useful review by Koester and Chanmugam [17].

1.1.5 Spectra and Classification

According to the WD formation, they are mainly composed of carbon (C) and oxygen (O) in its core and have atmospheres dominated by hydrogen (H) and helium (He). All other elements are only small traces, much less abundant than in the Sun. The reason for this separated pattern is the strong gravitational field [18], because the present lightest elements rapidly float to the surface once the white dwarf cools below about $T_{\rm eff} \sim 100,000K$. This atmosphere is a residue of the star's envelope in the red giant phase and can also contain material accreted from the interstellar medium.

The system currently used to classify the WDs atmosphere was introduced by Sion *et al.* [19] and has been subsequently revised several times [e.g., 20]. It classifies the spectra by a symbol which consists of an initial D ("dwarf"), a letter describing the primary feature of the spectrum followed by an optional sequence of letters describing secondary features of the spectrum (as the presence of magnetic field (H) or variable star (V)). The primary feature is classified as

- *A:* H lines present; no He I or metals present;
- *B:* He I lines; no H or metals present;
- *C:* continuous spectrum; no lines;
- *O:* He II strong; HeI or H present;
- *Z:* metal lines only; no H or He I lines;
- *Q:* carbon lines present;
- *X:* unclear or unclassifiable spectrum.

Therefore, WDs classified as DA have hydrogen-dominated atmospheres and make up the majority (approximately 80%) of all observed white dwarfs. The next class in number is of DBs (approximately 16%) which have helium-dominated atmospheres [21]. The hot ($T_{\rm eff} > 15,000$ K) DQ class (roughly 0.1%) have carbon-dominated atmospheres [22]. Assuming that carbon and metals are not present, which spectral classification is seen depends on the effective temperature. Between approximately 100,000 K to 45,000 K, the spectrum will be classified DO, dominated

by singly ionized helium. From 30,000 K to 12,000 K, the spectrum will be DB, showing neutral helium lines, and below about 12,000 K, the spectrum will be featureless and classified DC. The Figure 1.2 represents the stellar structure of some different classifications following the spectral type.

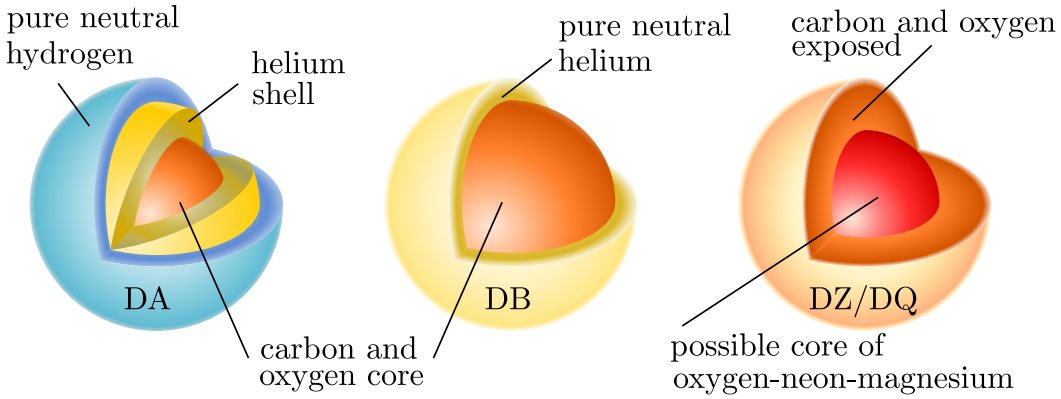

Figure 1.2: Author's artistic representation of the stellar structure of white dwarfs with the spectral type DA, DB, DZ and DQ.

Between 22,000 K to 18,000 K, there is a small group of stars, the DQ white dwarfs [23], which have C-dominated atmospheres. Their origin stills uncertain but a likely scenario is that the carbon is dredged up from below the atmosphere once the convection zone reaches deep enough. More recently, Kepler *et al.* [24] reported a WD star with oxygen 25 times more abundant than any other element in its atmosphere, and the fact that no hydrogen or helium is so far unknown.

Beyond that, from the astrophysical point of view, the hot WDs are important: (i) to elucidate the evolutionary links between WDs and their pre-white dwarf progenitors, i.e., whether they are from the asymptotic giant branch (AGB), binary evolution, or stellar mergers. (ii) to understand their significance in the process of chemical evolution of the Galaxy, because white dwarf progenitors lose their outer layers which are carbon, nitrogen, and oxygen rich at the top of the asymptotic giant branch (AGB) (iii) to improve our knowledge of type Ia supernova events, with important underlying implications for cosmology [e.g., 25].

1.1.6 Binary systems

The main stellar systems are binary, and our lonely Sun is a rare exception. The white dwarfs born in binary systems can capture appreciable amounts of matter from their companions. The accreted matter is compressed and heated, and its ignition can leads the WD to a powerful explosion.

Before accretion of material pushes a white dwarf close to the Chandrasekhar limit, accreted hydrogen-rich material on the surface may ignite in a less destructive

type of thermonuclear explosion powered by hydrogen fusion, called *nova*. The WD surface explosions can be repeated as long as the white dwarf's core remains intact, and mass transfer will occur gradually between novae explosions at a low rate, generating only weak X-ray emission. The nova outburst will increase the apparent brightness of the binary star system by 10^4 to 10^6 times (an increase in stellar magnitude of 10 to 15).

Carbon-oxygen white dwarfs accreting mass from a neighboring star may undergo a runaway nuclear fusion reaction, which leads to a Type Ia supernova explosion in which the white dwarf may be destroyed, before it reaches the limiting mass [e.g., 26]. If a white dwarf were to exceed the Chandrasekhar limit, and nuclear reactions did not take place (neon or magnesium-rich core), the pressure exerted by electrons would no longer be able to balance the force of gravity, and it would collapse into a denser object called a neutron star [e.g., 27].

1.2 The Death in a Type Ia Supernova

Type Ia supernovae (SNe Ia) are among the most powerful explosions in the Universe and have high scientific values in cosmology, being used to determine the cosmological parameters due to their high luminosity and remarkable uniformity [28, 29]. They are also a predominant synthesis of chemical elements in their host galaxies, especially for the contribution of iron [30, 31, 32].

In the last decade, the interest in SNe Ia has risen dramatically with their application to cosmological problems. Their unique capabilities as distance indicators on the cosmic scale have pushed them as a bright constraint of ΛCDM cosmology, with almost all Hubble constant determinations involving SNe Ia somehow. They provide the main route to the current expansion rate [33] and the acceleration of the universe [34, 35].

1.2.1 Light Curves and Standardized Candles

Type I Supernovae exhibit a sudden rise in luminosity, up to a maximum visual absolute magnitude of $M_V \sim -19.3$ ($L_{\text{peak}} \sim 10^{10} L_\odot$) in about 20 days. This phase is followed by a steep decline in brightness by about 3 magnitudes in ∼30 days, and later by a second, smoother decline over a period of ∼70 days [36].

Peak luminosities depend basically on the amount of ^{56}Ni synthesized, which can be inferred from models of the late-time, nebular spectra and through application of Arnett's rule [37]: the peak luminosity is proportional to the energy released by radioactive decays within the expanding ejecta. The Arnett's rule yields a value of $L_{\text{peak}} = 2 \times 10^{43} (M_{\text{Ni}}/M_\odot)$ erg/s such that the estimated ^{56}Ni masses from some

observed SNe Ia range between $0.1 - 1 M_{\odot}$ [38]. For the SN2011fe, the Arnett analytical formula fits the light curve data and gives a $M_{^{56}\mathrm{Ni}} = 0.6 M_{\odot}$ for this supernova, see Figure 1.3.

Another characteristic of SN I is the exponential tail of their light curve powered by the radioactive decay chain $^{56}\mathrm{Ni}(\beta^{+}\nu)^{56}\mathrm{Co}(\beta^{+}\nu)^{56}\mathrm{Fe}$ [39], with two different slopes attributed to the different half-lives of the decaying species, $T_{1/2}(^{56}\mathrm{Ni}) = 6.1$ days and $T_{1/2}(^{56}\mathrm{Co}) = 77.2$ days [40]. It has been shown that the energy deposition of γ-rays and positrons emitted from the decays of ^{56}Ni and ^{56}Co can produce a good fit to the observed light curves of SN I [e.g., 41].

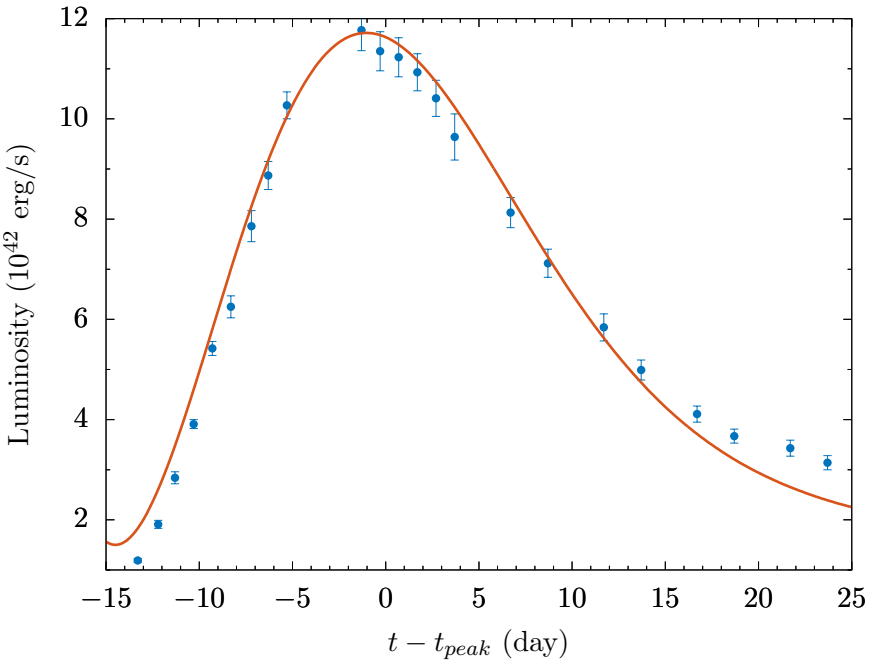

Figure 1.3: Comparison of the bolometric luminosity from the analytic model by Arnett [42] (*orange solid line*) and the SN2011fe data [43] (*blue circles*).

The observed photometric correlation between the peak luminosity and the timescale over which the light curve decays from its maximum [44] is understood physically as having both the luminosity and opacity being set by the mass of ^{56}Ni synthesized in the explosion [37, 45]. When corrected for the correlation between peak luminosity and light curve decay timescale, the intrinsic dispersion in SNIa light curves is ~ 0.14 mag [46, 47].

1.2.2 Nucleosynthesis and Spectra

Type Ia supernovae are spectroscopically identified by the absence of hydrogen emission Balmer lines and the presence of a prominent P Cygni Si II emission feature

near maximum light, due to the doublet $\lambda\lambda$ 6347 and 6371 $\AA$ with the blue-shifted absorption centered at about 6150 $\AA$.

The optical spectrum at maximum light is dominated by the presence of neutral or singly ionized lines of intermediate-mass elements (IMEs) as Si, Ca, Mg, S and O, moving at high speeds (in the range of $v \sim 8000 - 30000$ km s^{-1}). These absorptions are consistent with a structure of outer layers mainly composed by intermediate-mass elements [48]. Around two weeks after peak luminosity the spectrum is dominated by Fe II lines, which indicates an iron-rich core. Finally, a month after maximum, the spectrum is dominated by the presence of forbidden emission lines from Fe II, Fe III and Co III. These signatures are represented in Figure 1.4.

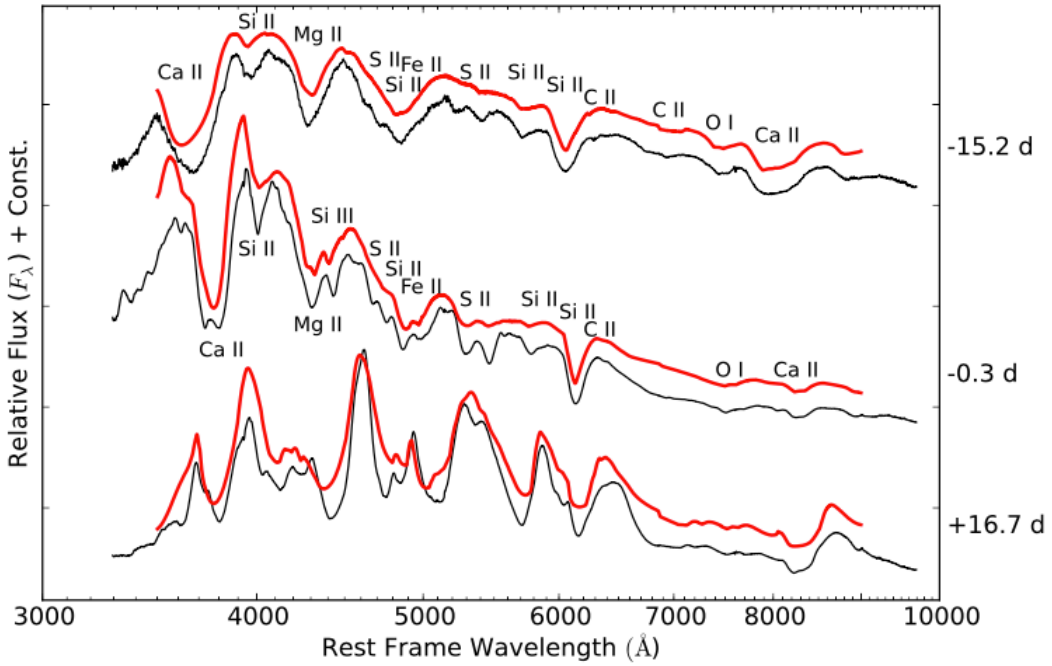

Figure 1.4: Spectrophotometry of SN 2011fe. Major ion signatures in the first two spectra are shown. The early and near-maximum spectra exhibit typical strong low- to-intermediate-mass ion signatures (O I, Mg II, Si II, S II, Ca II) at typical SN Ia ejection velocities. Two weeks after maximum, the spectrum is dominated by numerous blends from iron-peak elements (Fe II, Co II) blueward of about 5000 $\AA$. The days at right represent the time since the maximum in the light curve. Reproduced from [43].

The overall picture clearly stresses key nuclear physics issues: the presence of intermediate-mass elements in the early spectra, when only emission from the outermost ejected layers is seen, reveals that the thermonuclear explosion did not completely incinerate the star. This, in turn, provides clues on the flame propagation regime, since the presence of intermediate-mass elements rules out a pure detonation (Section 1.2.5). In sharp contrast, when inner regions of the star become accessible, the presence of the Fe lines clearly points toward complete nuclear processing of

matter to Fe-peak elements. Finally, the presence of Co lines at late stages strongly supports the hypothesis of a light curve tail powered by the ^{56}Ni decay.

1.2.3 Progenitor scenario

The absence of hydrogen lines into the spectra implies that the progenitor stars of SN Ia should be hydrogen-deficient stars. Additionally, SNe Ia have been observed in elliptical galaxies as well as in irregular and spiral galaxies, where they are not concentrated in spiral arms. These facts have led to the ideas that the progenitor stars of SNe Ia are white dwarfs or helium stars [49].

We already know that WDs can be composed of He, C, O, Ne and Mg. However, a pure helium WD with the initial mass smaller than $\sim 0.45 M_{\odot}$ has no coherent scenario with the explosion of SN Ia [50]: such system would explode during the accretion, at $M_{\rm WD} \sim 0.7 M_{\odot}$ [51], leaving ejecta composed only of He and ^{56}Ni, in contrast to the observed spectral signatures of IME elements. White dwarfs with O-Ne-Mg-rich material would rather collapse to a neutron star than explode because of the large electron capture effects [e.g., 52, 27]. Therefore, the only viable channel are the carbon-oxygen (CO) WDs.

Over the past four decades, two ways for leading a CO WD to an SN Ia explosion have been discussed frequently:

(i) *The single-degenerate (SD) scenario* [e.g., 53, 54]. In this scenario, a CO WD accretes hydrogen- or helium-rich matter from a non-degenerate star to increase its mass close to the Chandrasekhar limit and then results in a SN Ia explostion

(ii) *The double-degenerate (DD) scenario* [e.g., 55, 56]. In this scenario, a CO WD merges with another CO WD, their merging of which is due to the gravitational wave radiation which drives orbital inspiral to merger, resulting in a SN Ia explosion.

These scenarios have good observational clues as commented in a excellent review by Maoz *et al.* [58].

1.2.4 Energetics of the Explosion

The energy required to power a supernova explosion $\sim 10^{51}$ erg, obviously requires a powerful source. Early models attributed it to the thermonuclear processing of CO-rich material into Fe-peak elements inside a white dwarf [59]. Indeed, the incineration of $\sim 1 M_{\odot}$ of a C-O mixture, which releases $\sim 10^{18}$ erg.g^{-1}, accounts for the required 10^{51} erg. So SNe Ia arise from thermonuclear runaway explosions

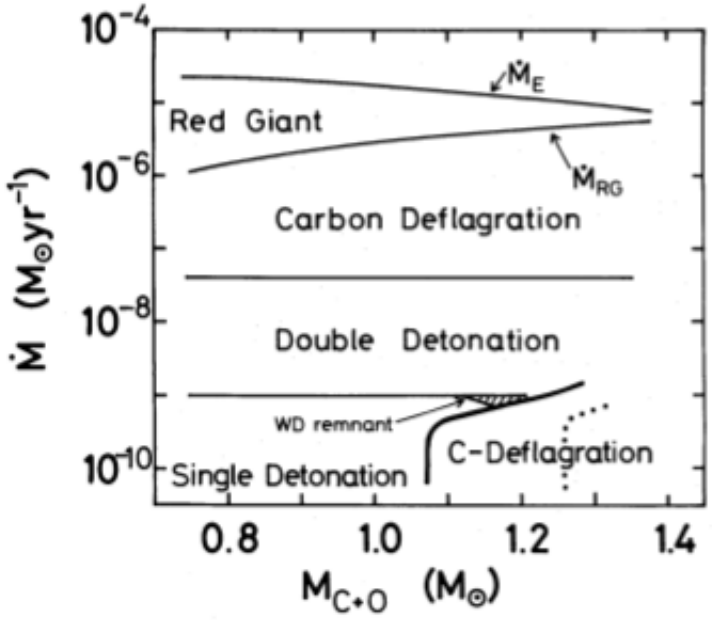

Figure 1.5: Possible models of SN I in a single-degenerate scenario, depending on the initial CO WD mass ($M_{\mathrm{C+O}}$) and on the accretion rate helium-rich material from the companion ($\dot{M}$). Figure reproduced from [57].

of carbon–oxygen white dwarfs (CO WDs) in binaries, although their progenitor systems and explosion mechanisms are still need to be understood.

Looking at energetics, the nuclear binding energy released by burning $0.6M_\odot$ of C and O into ^{56}Ni is 1.1×10^{51} erg. A comparable mass of C and O burning to intermediate-mass elements releases additional energy. The gravitational binding energy of a WD with mass close to M_{Ch} is $\sim 0.5 \times 10^{51}$ erg. The thermonuclear energy release is thus sufficient to unbind the WD and to give the ejecta the kinetic energy indicated by the observed expansion velocities, of order 10^4 km/s, i.e., $\sim 10^{51}$ erg.

Furthermore, the equation of state of the degenerate electron gas in a WD is just what is needed for an unstable thermonuclear runaway. An increase of some combination of density and temperature ignites the carbon-rich material. The temperature rapidly increases due to exothermic carbon burning but the highly degenerate matter remains static, i.e., it does not expand and cool as a classical gas would. As a result, an explosive burning front can, in principle, quickly consume a WD. The density or temperature increase has generally been attributed to the accumulation of accreted mass on the WD, up to the neighborhood of M_{Ch}, with a corresponding decrease in radius. Specifically, the carbon in the core of a non-rotating CO WD ignites at a WD mass of $\sim 0.8M_\odot$ [60]. The evidence that the bomb is always a CO WD with $M \sim M_{\mathrm{Ch}}$ would naturally explain the limited range of SN Ia luminosities, as employed by cosmology.

1.2.5 The state-of-art of Thermonuclear Explosions

Many types of combustion can occur in astrophysical problems, the particularity depends on the time scales. Therefore, the combustion can be controlled in regular process as hydrostatic burning (as in the sun core), but can be violent in explosive process (as in supernovae). Our understanding of nucleosynthesis and flame propagation in these explosive events is based on decades of modeling and nucleosynthesis calculations in spherically symmetric models [e.g., 36, 54, 57, 61, 62]. In recent years, detailed estimates of the nucleosynthetic yields for multidimensional explosion models have become possible [e.g., 63, 64, 65].

In a thermonuclear supernova the explosion is triggered by carbon burning as a thermal runaway, due to the high densities $\sim 10^9$ g.cm^{-3}. Because of the high sensitivity of the ^{12}C+^{12}C reaction rate on temperature ($\approx T^{12}$ at $T \sim 10^{10}$ K [66]), the carbon burning length scale is microscopic and there are two mechanisms for the propagation of these burning fronts [67]: the front propagates by shock compression, at a sonic or supersonic speed as a detonation wave; the front propagates by thermal conduction as a deflagration wave. In principle, both modes can be present in thermonuclear supernova depending on the ignition details.

One-dimensional numerical models of SNe Ia have been extensively used to test general ideas about those possible explosion mechanisms. The most influential are the phenomenological model W7 by Nomoto *et al.* [54, 62, 57, 68] and similar explosions models [69, 70] which enjoy a great popularity as the explosive input model for spectral calculations since they seemed to reproduce the element distribution fairly accurately [e.g., 71, 72]. The burning speed in this model has, however, never been understood in physical terms.

The initiation of the burning in the degenerate star remains, however, a puzzle. For many years it was clear that a pure detonation [e.g., 61] of CO WDs burns the entire star to nuclear statistical equilibrium and fail to synthesize the intermediate-mass elements (IMEs), such as Ne, Mg, Si, S, and Ca, at high velocities needed to reproduce SN Ia spectra [e.g., 33]. A pure deflagrations [e.g., 73] achieve adequate amounts of IMEs but produce less ^{56}Ni masses, being considered a feasible mechanism only for the least luminous events.

A possible alternative is the pre-expansion of the white dwarf with an initial deflagration stage followed by a detonation wave producing intermediate mass elements in the low density material, as in the deflagration-to-detonation transition model from Khokhlov *et al.* [74, 75]. The critical parameters in these models are the density at the transition from deflagration to detonation, the pre-explosion density, the chemical composition (mostly C/O ratio), and the deflagration speed at the beginning of the burning. The transition density has been proposed as the critical

parameter for the nucleosynthesis and hence the amount of Ni produced in the explosion. These delayed-detonation models can reproduce some of the observations [76]. However, their consistency has been questioned recently [77, 78].

Another different explosion mechanism on sub-Chandrasekhar mass white dwarfs has been proposed [62, 69, 79, 80, 81]. The main idea is that the explosion must be generated at the surface of the white dwarf due to a detonation of He near the bottom of the accretion layer, depending on the accretion rate as represented in Figure 1.5. This model solved the progenitor problem by allowing explosions well below the Chandrasekhar mass near the peak of the white dwarf mass distribution. Difficulties here are the initiation of the explosion and the subsequent ignition of the whole star by a pressure wave. Many of these calculations are still parametric and the details have to be worked out [c.f., 82].

It is customary nowadays to explore several of these explosion models to explain the observations [e.g., 82, 83, 84].

1.3 Objectives of this work

As motivated in the previous sections, the objectives of this work are concentrated in the non-equilibrium phenomena that can be separated into two main groups: the quasi-stationarity of the cooling process of white dwarfs; and the possible retardation in thermalization processes within the framework of hydrodynamic calculations of thermonuclear supernovae on the deflagration-detonation transition scenario.

The main questions to be answered here are:

(i) Can the thermal evolution of white dwarfs be modeled as a stationary state of non-equilibrium thermodynamics?

(ii) What numerical method of hydrodynamics is appropriated to the study of transient process in thermonuclear supernova?

(iii) Does the retardation effects modify the nuclear energy generation and the nucleosynthesis of type Ia supernovae? How can we model them in a simplified approach?

1.4 Organization of this thesis

This thesis is organized as follows. In Chapter 2 we introduce the physical description of non-equilibrium phenomena by the non-equilibrium thermodynamics. In Chapter 3 we describe the astrophysical environment and present the ingredients

for the interior of white dwarfs and thermonuclear supernovae. The Chapter 4 is the more technical and mathematical, where we present the numerical methods used to simulate the thermonuclear supernovae. In Chapter 5, we present a phenomenological approach to the thermal evolution as a stationary state for white dwarfs, and we obtain a semi-empirical effective temperature-mass-radius relation for hot white dwarfs recent data. In Chapter 6 we introduce a model for non-equilibrium delayed thermalization in thermonuclear supernovae and analyze its effects in the nucleosynthesis and nuclear energy releasing. Finally, in Chapter 7, we remark some points and reflect on future applications of the present results.

Chapter 2

Non-equilibrium Thermodynamics

Nothing is more practical than a good theory.

– L. Boltzmann (1844-1906)

We live in a Universe that is not in thermodynamic equilibrium. The 2.8 K cosmic microwave background thermal radiation that fills the universe is not in thermal equilibrium with the matter in the galaxies. On a smaller scale, the Earth, its atmosphere, biosphere and the oceans are out of equilibrium state due to the constant influx of energy from the Sun. In resume, we encounter non-equilibrium phenomena everywhere while equilibrium systems are the exception.

2.1 Local Thermodynamic Equilibrium Hypothesis

Equilibrium thermodynamics describes ideal processes taking place at infinitely slow rate, considered as a sequence of equilibrium states. For arbitrary processes, it may only compare the initial and final equilibrium states but it cannot describes the processes themselves. But in the more realistic situations involving processes with finite velocities or inhomogeneous situations, the basic physical quantities like mass, temperature, pressure, and others are not only allowed to change from place to place, but also in the course of time.

A macroscopic system can be thought as composed by cells, which are sufficiently large to neglect the microscopic fluctuations but sufficiently small so that equilibrium is realized to a good approximation in each individual cell. In other words, the time and length scales associated with the macroscopic inhomogeneities, e.g., of the pressure

$$\left|\frac{1}{p}\frac{\partial p}{\partial t}\right| \simeq \frac{1}{\tau_p} \quad \text{and} \quad \left|\frac{1}{p}\nabla p\right| \simeq \frac{1}{\lambda_p} \tag{2.1}$$

must be much larger than the microscopic scales, as typical collision time τ_{micro} and typical mean free path λ_{micro},

$$\tau_p \gg \tau_{\text{micro}} \quad \text{and} \quad \lambda_p \gg \lambda_{\text{micro}} \tag{2.2}$$

to consider that matter within the cell is locally in equilibrium. This approach composes the most important hypothesis underlying the non-equilibrium phenomena, the local thermodynamic equilibrium (LTE) hypothesis: *the local and instantaneous relations between thermodynamics quantities in a system out of equilibrium are the same as for a uniform system in equilibrium*. The concept of locality is misleading, since the spatial region considered infinitesimal is physical fluid element that have a lot of particles inside it, but it is small enough to (2.2) become valid.

A important consequence of the LTE hypothesis is that all the thermodynamic quantities well defined in equilibrium as internal energy, temperature, chemical potential, etc. are univocally defined out of equilibrium and they may vary with time and space. All the intensive thermodynamic quantities are now functions of the fluid element position and time as

$$T = T(\boldsymbol{x}, t), \quad p = p(\boldsymbol{x}, t), \quad \mu_k = \mu_k(\boldsymbol{x}, t), \tag{2.3}$$

where T is the equilibrium temperature, p is the equilibrium pressure, and μ_k the thermodynamic or chemical potential of component k. The extensive variables are replaced by their densities

$$u = u(\boldsymbol{x}, t), \quad \rho = \rho(\boldsymbol{x}, t), \quad n_k = n_k(\boldsymbol{x}, t). \tag{2.4}$$

where u is the internal energy per unit mass, ρ the mass density, and n_k the number component k per unit mass.

From equilibrium thermodynamics we know that the entropy s is, for a system in equilibrium, a well-defined function of the various parameters which are necessary to define the macroscopic state of the system completely. Considering the macroscopic state defined by u, ρ and n_k, we get

$$s = s(u, \rho, n_k). \tag{2.5}$$

Although the total system is not in equilibrium, there is within small fluid elements a state of local equilibrium for which the local entropy s is the same function of u, ρ and n_k as in real equilibrium. In such a way the Gibbs relation

$$T\frac{\mathrm{d}s}{\mathrm{d}t} = \frac{\mathrm{d}u}{\mathrm{d}t} + \frac{p}{\rho^2}\frac{\mathrm{d}\rho}{\mathrm{d}t} - \sum_{k=1}^{N} \mu_k \frac{\mathrm{d}n_k}{\mathrm{d}t} \tag{2.6}$$

remains valid within the fluid element. The relation (2.6) to the equilibrium entropy, but when there are irreversible process inside the fluid element the concept of equilibrium entropy has to be modified or extended.

2.2 Conservation Laws

When a system is disturbed from its equilibrium state, quantities which are not conserved decay rapidly to their equilibrium values while the quantities which are conserved remain out of equilibrium. The densities of conserved quantities characterize the non-equilibrium behavior of the fluid after long times [85]. The equations of motion for the densities of the conserved quantities are the hydrodynamic equations, which describe the long-wavelength (low-frequency) phenomena in a large variety of systems, including dilute gases, liquids, solids, superfluids and chemically reacting systems [e.g., 67].

Based on the LTE hypothesis, the first law of thermodynamics applied to a fluid element is

$$\frac{\mathrm{d}E}{\mathrm{d}t} = \frac{\mathrm{d}W}{\mathrm{d}t} + \frac{\mathrm{d}Q}{\mathrm{d}t} \tag{2.7}$$

and it express the change of total energy E due to the external or internal work W and heat Q. More explicitly, the total energy is equal to the sum of the internal energy U and the kinetic energy K, i.e., $E = K + U$ and it is given by

$$U = \int_{V(t)} \rho u \, \mathrm{d}V \quad \text{and} \quad K = \frac{1}{2} \int_{V(t)} \rho \boldsymbol{v} \cdot \boldsymbol{v} \, \mathrm{d}V, \tag{2.8}$$

with $\boldsymbol{v}$ being the velocity field.

The rate of work done by the body forces $\boldsymbol{f}$ and the contact forces $\boldsymbol{\pi}$ is given by

$$\frac{\mathrm{d}W}{\mathrm{d}t} = -\int_{A(t)} \boldsymbol{\pi} \cdot \boldsymbol{v} \, \mathrm{d}A + \int_{V(t)} \rho \boldsymbol{f} \cdot \boldsymbol{v} \, \mathrm{d}V, \tag{2.9}$$

where $\boldsymbol{\pi}$ is related to the stress tensor $\boldsymbol{P}$ by the Cauchy's relation $\boldsymbol{\pi} = -\boldsymbol{P} \cdot \boldsymbol{n}$ [e.g., 86, § 22].

The rate of heat exchange is given by

$$\frac{\mathrm{d}Q}{\mathrm{d}t} = -\int_{A(t)} \boldsymbol{q} \cdot \boldsymbol{n} \, \mathrm{d}A, \tag{2.10}$$

and $\boldsymbol{q}$ is the heat flux vector.

Using the Reynolds transport theorem[1] and substituting (2.8), (2.9) and (2.10) in

[1] Let $A(\boldsymbol{x}, t)$ be any single-valued scalar, vector, or tensor field, and choose $\mathcal{V}(t)$ to be some finite volume composed of several fluid elements. Then, clearly $\mathcal{A}(t) = \int_{\mathcal{V}} A(\boldsymbol{x}, t) \, \mathrm{d}V$ is a defined function

the first law (2.7), we can obtain the local form of the energy balance equation

$$\rho(\dot{u} + \boldsymbol{v}\cdot\dot{\boldsymbol{q}}) + \left(u + \frac{1}{2}\boldsymbol{v}\cdot\boldsymbol{v}\right)(\dot{\rho} + \rho\boldsymbol{\nabla}\cdot\boldsymbol{v}) = -\boldsymbol{\nabla}\cdot\boldsymbol{q} - \boldsymbol{\Pi}\colon\boldsymbol{\nabla}\boldsymbol{v} - \boldsymbol{v}\cdot(\boldsymbol{\nabla}\cdot\boldsymbol{P}) + \rho\boldsymbol{f}\cdot\boldsymbol{v}, \tag{2.12}$$

where the upper dot stands for the Lagrangian time derivative, i.e., $\dot{u} \equiv \mathrm{d}u/\mathrm{d}t$. According to the Galileo principle, (2.12) must be invariant for inertial frames, i.e., must be invariant with respect to the transformation $\boldsymbol{v} \to \boldsymbol{v} + \boldsymbol{v}_0$, where $\boldsymbol{v}_0$ is an uniform and constant velocity. Making this transformation and subtracting the (2.12), we obtain

$$\frac{1}{2}\boldsymbol{v}_0\cdot\boldsymbol{v}_0(\dot{\rho} + \rho\boldsymbol{\nabla}\cdot\boldsymbol{v}) + \boldsymbol{v}_0\cdot[(\dot{\rho} + \rho\boldsymbol{\nabla}\cdot\boldsymbol{v}) + \rho\dot{\boldsymbol{v}} + \boldsymbol{\nabla}\cdot\boldsymbol{P} - \rho\boldsymbol{f}] = 0. \tag{2.13}$$

This relation should be independent of the choice of $\boldsymbol{v}_0$, so that the relations

$$\dot{\rho} = -\rho\boldsymbol{\nabla}\cdot\boldsymbol{v}, \tag{2.14}$$

$$\rho\dot{\boldsymbol{v}} = -\boldsymbol{\nabla}\cdot\boldsymbol{P} + \rho\boldsymbol{f}, \tag{2.15}$$

could be satisfied independently. With these results, (2.12) reduces to

$$\rho\dot{u} = -\boldsymbol{\nabla}\cdot\boldsymbol{q} - \boldsymbol{P}\colon\boldsymbol{\nabla}\boldsymbol{v}. \tag{2.16}$$

Relations (2.14), (2.15) and (2.16) are the laws of balance of mass, momentum, and internal energy respectively, written in the Lagrangian viewpoint, which consider a fluid element in time at a point that moves with the fluid at velocity $\boldsymbol{v}$. The Lagrangian time derivative operator is related to the usual derivative operators by

$$\frac{\mathrm{d}}{\mathrm{d}t} = \frac{\partial}{\partial t} + \boldsymbol{v}\cdot\boldsymbol{\nabla} \tag{2.17}$$

2.2.1 Viscous and Heat-Conducting Fluids

All real fluids have internal processes that may lead to transport of momentum and energy from one fluid element to another on a microscopic level.

The momentum transport mechanisms give rise to internal forces which contribute to the stress tensor $\boldsymbol{P}$. The form of P_{ij} may be deduced from the following physical considerations: (i) internal forces exist only when one element of fluid

of time. Its time derivative can be written as

$$\frac{\mathrm{d}\mathcal{A}}{\mathrm{d}t} = \int_{\mathcal{V}}\left[\frac{\partial A}{\partial t} + \boldsymbol{\nabla}\cdot(\boldsymbol{v}A)\right]\mathrm{d}V \tag{2.11}$$

where the first term in parenthesis came from the direct derivative of A and the second term came from the change in the fluid element volume [e.g., 86, § 18]

moves relative to another; hence viscous terms must depend on the space derivatives of the velocity field, $\partial v_i/\partial x_j$. (ii) the stress tensor reduce to its hydrostatic form when fluid is at rest or translate uniformly (Galilean transformation). We therefore write

$$P_{ij} = -p\delta_{ij} + \Pi_{ij} \tag{2.18}$$

where Π_{ij} is the viscous stress tensor, which accounts for the internal frictional forces in the flow. (iii) viscous forces must be zero within an element of fluid in rigid rotation (because there is no slippage then). The most general symmetrical tensor of rank two satisfying the above conditions can be written in a convenient form as

$$\Pi_{ij} = \eta\left(\frac{\partial v_i}{\partial x_j} + \frac{\partial v_j}{\partial x_i} - \frac{2}{3}\delta_{ij}\frac{\partial v_k}{\partial x_k}\right) + \zeta\delta_{ij}\frac{\partial v_k}{\partial x_k} \tag{2.19}$$

where η is identified as the coefficient of shear viscosity and ζ is known as the coefficient of bulk viscosity.

The balance of momentum equation (2.15) is extremely general because it makes no particular assumptions about the form of the stress tensor. If we specialize this equation to the case of a viscous fluid by using the equations (2.18) and (2.19), we obtain the *Navier-Stokes equation*, which are the equations employed to describe the flow of a viscous fluid. We find by direct substitution,

$$\rho\frac{\mathrm{d}\boldsymbol{v}}{\mathrm{d}t} = \boldsymbol{f} - \boldsymbol{\nabla}p + \eta\nabla^2\boldsymbol{v} + (\zeta + \tfrac{1}{3}\eta)\boldsymbol{\nabla}(\boldsymbol{\nabla}\cdot\boldsymbol{v}) \tag{2.20}$$

For a heat-conducting fluid, apart from the energy transport mechanisms due to the momentum transport there is energy transport coming from the energy conducting from one fluid element in the flow to another. Therefore, the (2.16) can be written as

$$\rho\dot{u} = \boldsymbol{\nabla}\cdot(\lambda\boldsymbol{\nabla}T) - p\boldsymbol{\nabla}\cdot\boldsymbol{v} + 2\eta\boldsymbol{\nabla}\boldsymbol{v}\colon\boldsymbol{\nabla}\boldsymbol{v} + \zeta(\boldsymbol{\nabla}\cdot\boldsymbol{v})^2. \tag{2.21}$$

The Navier-Stokes equation and its extension to the relativistic case can be obtained by a more fundamental derivation from the relativistic Boltzmann equation, as presented by Denicol *et al.* [87, 88].

2.2.2 Reactive Fluids

A system composed by n different constituents, each species k in the fluid may be characterized by the atomic number Z_k, the mass number A_k and its mass density

ρ_k. The balance equation of species density can be written as

$$\dot{\rho_k} = -\rho_k \nabla \cdot \boldsymbol{v}_k + \sum_{j=1}^{r} \nu_{kj} \Lambda_k \tag{2.22}$$

where $\boldsymbol{v}_k$ is the velocity of species k, $\nu_{kj}\Lambda_k$ is a source term giving the production (or destruction) of k per unit volume by the j-th reaction, and r is the number of reactions involving the component k.

Since mass is conserved in each separate chemical reaction we have

$$\sum_{k=1}^{n} \nu_{kj} = 0, \tag{2.23}$$

and hence the equation (2.22) summed over all substances k returns the conservation of mass (2.14). The total density may be now described by

$$\rho = \sum_{k=1}^{n} \rho_k \tag{2.24}$$

and the center-of-mass velocity by

$$\boldsymbol{v} = \frac{\sum_{k=1}^{n} \rho_k \boldsymbol{v}_k}{\rho} \tag{2.25}$$

The abundance of component k can be expressed by the mass fraction X_k, defined as

$$X_k = \frac{\rho_k}{\rho} \tag{2.26}$$

subject to the normalization condition $\sum_{k=1}^{n} X_k = 1$. In terms of X_k equations (2.22) take the simple form

$$\rho \frac{\mathrm{d}X_k}{\mathrm{d}t} = -\nabla \cdot \boldsymbol{j}_k + \sum_{j=1}^{r} \nu_{kj} \Lambda_k, \tag{2.27}$$

where $\boldsymbol{j}_k = \rho_k(\boldsymbol{v}_k - \boldsymbol{v})$ is the diffusion flow with respect to the barycentric motion. We note that it follows from (2.25) that $\sum_{k=1}^{n} \boldsymbol{j}_k = 0$, which means that only $n-1$ of the n diffusion flows are independent.

The external force term $\boldsymbol{f}$ in (2.15) must be modified since the external force may vary for different species (for example, the electromagnetic force in different ions), i.e., $\boldsymbol{f}_k$ is the external force applied to the component k, so we must write the balance of momentum as

$$\rho \frac{\mathrm{d}\boldsymbol{v}}{\mathrm{d}t} = -\nabla \cdot \boldsymbol{P} + \sum_{k=1}^{n} \rho_k \boldsymbol{f}_k, \tag{2.28}$$

and the balance of internal energy (2.16) now has to add this external force term in

the form

$$\rho \dot{u} = -\boldsymbol{\nabla} \cdot \boldsymbol{q} - \boldsymbol{P} \colon \boldsymbol{\nabla} \boldsymbol{v} + \sum_{k=1}^{n} \boldsymbol{j}_k \cdot \boldsymbol{f}_k \tag{2.29}$$

and when the external force is identical for all species, i.e., $\boldsymbol{f}_k = \boldsymbol{f}$, the last parcel (2.29) in vanishes.

2.3 Entropy Production

An important question is whether a precise definition can be attached to the notion of entropy when the system is out of equilibrium. However, thanks to the local equilibrium hypothesis, entropy remains a valuable state function even in non-equilibrium situations.

The change of the total entropy with the time in a region is the sum of the internal entropy generation inside this region and the total entropy flux exchanged with the neighborhood through the region boundary, i.e.,

$$\frac{\mathrm{d}}{\mathrm{d}t} \int_{\mathcal{V}} \rho s \, \mathrm{d}V = \int_{\mathcal{V}} \epsilon_s \, \mathrm{d}V - \int_{A} \boldsymbol{j_s} \cdot \mathrm{d}\boldsymbol{A}, \tag{2.30}$$

with the entropy flux $\boldsymbol{j_s}$ and the rate of entropy production ϵ_s conveniently defined. Using the Gauss and Reynolds theorems, we write the following local balance relation of entropy

$$\rho \frac{\mathrm{d}s}{\mathrm{d}t} = \epsilon_s - \boldsymbol{\nabla} \cdot \boldsymbol{j_s}. \tag{2.31}$$

The second law of thermodynamics applied to a closed system implies that

$$\frac{\mathrm{d}}{\mathrm{d}t} \int_{\mathcal{V}} \rho s \, \mathrm{d}V \geq 0, \tag{2.32}$$

and since there is no change of entropy with the external environment the (2.32) results in

$$\epsilon_s \geq 0 \tag{2.33}$$

where the equality holds for reversible processes or for equilibrium states.

2.3.1 Entropy Production in Viscous, Heat-Conducting and Reactive Fluids

In order to find the explicit form of the entropy balance equation (2.31) for a viscous, heat-conducting and reactive fluid, we have to insert the appropriate combination of the balance of internal energy for viscous and heat-conducting fluid (2.21)

and for reactive fluid (2.29) into the Gibbs relation (2.6). This gives

$$\rho\frac{\mathrm{d}s}{\mathrm{d}t} = -\frac{1}{T}\boldsymbol{\nabla}\cdot\boldsymbol{q} - \frac{1}{T}\boldsymbol{\Pi}\colon\boldsymbol{\nabla}\boldsymbol{v} + \frac{1}{T}\sum_{k=1}^{n}\boldsymbol{j}_k\cdot\boldsymbol{f}_k + \frac{1}{T}\sum_{k=1}^{n}\mu_k\boldsymbol{\nabla}\cdot\boldsymbol{j}_k - \frac{1}{T}\sum_{j=1}^{r}\Lambda_j A_j \tag{2.34}$$

where we have introduced the chemical affinities of the r reactions for the species j defined by

$$A_j = \sum_{k=1}^{r}\nu_{kj}\mu_k \tag{2.35}$$

and used the (2.22) to simplify the $n_k = N_A\rho_k/A_k$ derivative.

From comparison with (2.31) it follows that the expressions for the entropy flux and the entropy production are given by

$$\boldsymbol{j}_s = \frac{1}{T}\left(\boldsymbol{q} - \sum_{k=1}^{n}\mu_k\boldsymbol{j}_k\right) \tag{2.36}$$

$$\epsilon_s = -\frac{1}{T^2}\boldsymbol{q}\cdot\boldsymbol{\nabla}T - \frac{1}{T}\boldsymbol{\Pi}\colon\boldsymbol{\nabla}\boldsymbol{v} - \frac{1}{T}\sum_{k=1}^{n}\boldsymbol{j}_k\cdot\left[T\boldsymbol{\nabla}\left(\frac{\mu_k}{T}\right) - \boldsymbol{f}_k\right] - \frac{1}{T}\sum_{j=1}^{r}\Lambda_j A_j \tag{2.37}$$

Let us consider in more detail the expressions (2.36) and (2.37). The first formula shows for open systems the entropy flow consists of two parts: one is the strict heat flow $\boldsymbol{q}$, the other is connected with the diffusion flows of matter $\boldsymbol{j}_k$. The second formula demonstrates that the entropy production contains four different contributions. The first term at the right-hand side of (2.37) arises from heat conduction, the second is connected to the gradients of the velocity field, the third from diffusion, and the fourth is due to chemical reactions. The structure of the expression for ϵ_s is that of a bilinear form: it consists of a sum of products of two factors. One of these factors in each term is a flow quantity (heat flow, diffusion flow, momentum of a viscous flow, and chemical "flow" reactions) already introduced in the conservation laws of Section 2.2. The other factor in each term is related to a gradient of an intensive state variable (gradients of temperature, chemical potential and velocity) and can also be a difference of thermodynamic state variables, e.g., the chemical affinity A_j. In terms of them the source of entropy can be written as

$$\epsilon^s = \sum_{\alpha} J_\alpha F_\alpha \tag{2.38}$$

and in equilibrium state each individual flux and force vanishes.

2.3.2 Linear Phenomenological Coefficients

The non-equilibrium processes in nature are very often described using the so-called linear non-equilibrium thermodynamics. This theory has been developed since the pioneering works by Onsager [89, 90] and Prigogine [91], who won the Nobel Prize in Chemistry in 1968 and 1977, respectively. Other important and influential contributions are also found in the works of Meixner and Reik [92], de Groot and Mazur [93], Gyarmati [94], and many others, which have enlarged the theory to a wider number of applications and have clarified its foundations and its limits of validity.

The fluxes are unknown quantities, in contrast to the forces, which are known functions of the state variables or their gradients. It has been found experimentally that fluxes and forces have a relationship with each other. In general, a given flux does not only depend on its own conjugated force but my depend on the every set of forces acting on the system. Furthermore, the flux may depend on all thermodynamic state variables ρ, u and n_k as

$$J_\alpha = J_\alpha(F_1, F_2, \ldots, F_\alpha, \ldots, \rho, u, n_k). \tag{2.39}$$

A relation like (2.39) among fluxes and forces is called a constitutive equation, which express specific properties of the thermodynamic system in an irreversible process. An expansion around the equilibrium values $J_\alpha^{\text{eq}} = 0$ and $F_\alpha^{\text{eq}} = 0$ gives

$$J_\alpha = \sum_\beta \left(\frac{\partial J_\alpha}{\partial F_\beta}\right)_{\text{eq}} F_\beta + \mathcal{O}(F_\beta F_\gamma) + \ldots \tag{2.40}$$

and keeping just the first terms we find

$$J_\alpha = \sum_\beta L_{\alpha\beta} F_\beta \tag{2.41}$$

setting

$$L_{\alpha\beta} = \left(\frac{\partial J_\alpha}{\partial X_\beta}\right)_{\text{eq}} \tag{2.42}$$

which are Onsager's phenomenological coefficients [89, 90]. and depend generally on ρ, u, and n_k. This idea is based upon the empirical laws (of J. Fourier [95], G. Ohm [96], A. Fick [97], and others) that have a linear relationship between the thermodynamic fluxes J_α (e.g., the heat flux) and the thermodynamic forces F_α (e.g., the

temperature gradient). By substitution of (2.41) into (2.38) we get

$$\epsilon^s = \sum_{\alpha\beta} L_{\alpha\beta} F_\alpha F_\beta \geq 0 \tag{2.43}$$

The fact that $\epsilon^s \geq 0$ implies the necessary and sufficient conditions that the determinant of the symmetric part of $L_{\alpha\beta}$ and all its principal minors are positive, in particular,

$$L_{\alpha\alpha} \geq 0, \tag{2.44}$$

$$L_{\alpha\alpha} L_{\beta\beta} \geq \tfrac{1}{4}(L_{\alpha\beta} + L_{\beta\alpha}). \tag{2.45}$$

These coefficients, in Navier-Stokes theory, are linearly proportional to the thermodynamic forces, such as gradients of fluid velocity, temperature, and chemical potential. The constants of proportionality are the bulk viscosity, the shear viscosity, and the heat conductivity and they are all semi-positive definite quantities. Navier-Stokes theory can be extended by considering higher-order gradients of fluid velocity, temperature, or chemical potential, leading to the Burnett equations (including second-order gradients), the super-Burnett equations (including third-order gradients) etc. [98].

2.4 Non-equilibrium Stationary States

Stationary states are state states in which the state parameters are independent of time. Such state cannot be confused with an equilibrium state, which is characterized by a uniform temperature field, no heat flow, and a zero entropy production. These stationary states can be either equilibrium or non-equilibrium states depending on the boundary conditions imposed on the system.

2.4.1 Mechanical Equilibrium

The mechanical equilibrium state is the state in which the acceleration $\mathrm{d}\boldsymbol{v}/\mathrm{d}t$ vanishes. This concept of mechanical equilibrium may be extended to consider states in which not only the acceleration vanishes, but in which velocity gradients may be neglected. For such states the equation of motion gets the form

$$0 = -\boldsymbol{\nabla} p + \sum_k \rho_k \boldsymbol{f}_k. \tag{2.46}$$

In a number of important cases the mechanical equilibrium state described by (2.46) is established very quickly in comparison to other thermodynamic processes. For instance, in the cases of diffusion or thermal diffusion phenomena in closed

system can safely assume that a state of mechanical equilibrium is a sufficient approximation [see, 93, Ch. V, § 2].

2.4.2 Thermal Stationary State

The thermal stationary state is the state in which the entropy production $\mathrm{d}s/\mathrm{d}t$ vanishes. For such states the equation of entropy balance gets the form

$$0 = \boldsymbol{\nabla} \cdot \boldsymbol{j}_s + \epsilon_s. \tag{2.47}$$

More explicitly, with considerable generality, we might write

$$\boldsymbol{j}_s = \boldsymbol{j}_{\mathrm{rad}} + \boldsymbol{j}_{\mathrm{cond}} + \boldsymbol{j}_{\mathrm{conv}} + \boldsymbol{j}_{\mathrm{mass}} \tag{2.48}$$

where the first three terms on the right denote the radiative, conductive, and convective fluxes, respectively. The last term $\boldsymbol{j}_{\mathrm{mass}}$ represents a flux of energy resulting from the net transfer of matter.

We might also write

$$\epsilon_s = \epsilon_{\mathrm{rea}} + \epsilon_{\mathrm{vis}} \tag{2.49}$$

where the first term denote the rates of entropy production per unit mass from reactions, and the second term from viscous heating arising from fluid motions.

It should be noted that even in the case without entropy sources ($\epsilon_s = 0$), the system will not be precisely in thermal equilibrium. In the simplest case, the $\boldsymbol{\nabla} \cdot \boldsymbol{j}_s = 0$ becomes the Poisson's equation and its solution depends on the boundary conditions.

2.5 Relaxation from Near-Equilibrium States

2.5.1 Motivation

Onsager [89] noted that Fourier's model contradicts the principle of microscopic reversibility, but it may be removed when we recognize that Fourier's law is only an approximate description of the process of conduction, neglecting the time needed for acceleration of the heat flow. In other words, Fourier's law has an nonphysical property: if a sudden temperature perturbation is applied at one point in the solid, it will be felt instantaneously and everywhere at distant points. Moreover, Fourier's model is not adequate for describing heat transport at very high frequencies and short wavelengths, when the phenomena are very fast or very steep (as ultrasound propagation, heat propagation at low temperatures, shock waves, etc.) or when the

relaxation times of the fluxes are very long (as in superfluids).

Historically, Maxwell [99] and Cattaneo [100] were the first to introduce inertia in transport equations to eliminate these anomalies. They proposed a damped version of Fourier's law by introducing a heat flux relaxation term, namely

$$\frac{\partial \boldsymbol{q}}{\partial t} = -\frac{1}{\tau_q}\left(\boldsymbol{q} + \lambda \boldsymbol{\nabla} T\right). \tag{2.50}$$

The relaxation time τ_q is the response time for the onset of heat flow after a temperature gradient is suddenly imposed. When τ_q is negligible or when the time variation of the heat flux is slow, (2.50) reduces to Fourier's law. The expression for the entropy production (2.37) is now written as

$$\epsilon_s = \frac{\lambda}{T^2}(\boldsymbol{\nabla} T)^2 + \frac{\tau_q}{T^2}\frac{\partial \boldsymbol{q}}{\partial t} \cdot \boldsymbol{\nabla} T \tag{2.51}$$

which is no longer definite positive because of the second term.

2.5.2 Relaxation Kernel

To avoid this problem, the inertial effects can be extended by a relaxation kernel which relates the heat flux with the temperature gradient

$$\boldsymbol{q}(t) = \int_{-\infty}^{t} G(t, t'; \tau)[-\lambda \boldsymbol{\nabla} T](t')\, \mathrm{d}t', \tag{2.52}$$

and for $G(t, t'; \tau) = \exp\left[(t - t')/\tau\right]/\tau$ we recover the Maxwell-Cattaneo equation (2.50).

In the linear non-equilibrium thermodynamic, other thermodynamic fluxes and forces can be present and the generalization of the (2.52) for (2.41) will be

$$J_\alpha(t) = \sum_\beta \int_{-\infty}^{t} G(t, t'; \tau_\beta) L_{\alpha\beta}(t') F_\beta(t')\, \mathrm{d}t', \tag{2.53}$$

with the entropy source term still given by (2.38). Of course, this entropy source term remains no longer definite positive when $G(t, t'; \tau) = \exp\left[(t - t')/\tau\right]/\tau$ as in the Maxwell-Cattaneo framework.

The (2.53) introduce new parameters τ_β which can be associated with the relaxation time of the thermodynamic forces to appear as thermodynamic fluxes in the system. We will use this framework to treat transient phenomena with near-equilibrium thermodynamic.

2.6 Final Considerations

We have formulated the partial differential equations governing the flow of an viscous, heat-conducting and reactive fluid: the balance equations for mass (2.14), momentum (2.15), chemical abundances (2.22), and entropy (2.31). These equations are related to the following dependent variables: the density ρ, the specific entropy s, the velocity field v and the density of species n_k.

To close the system we require the *constitutive equations*, the *transport coefficients* and the *reaction rates* that specify the thermodynamic properties, the intensity of the transport phenomena and the change of the chemical abundances, respectively. In a system with total number of particles fixed, any thermodynamic quantity can be expressed as a function of two variables. Therefore, all quantities are written as function of mass density ρ and temperature T as the equation of state $p = p(\rho, T)$ and the thermodynamic entropy $s = s(\rho, T)$. The transport coefficients are condensed in a single opacity coefficient, $\kappa = \kappa(\rho, T)$. The reaction rates and the heat generation are given as $\Lambda = \Lambda(\rho, T)$ and $\epsilon = \epsilon(\rho, T)$. All these quantities and relations will be presented in Chapter 3 for the stellar plasma which we will consider in this work.

We then have a total of four equations and four unknowns variables[2]: ρ, s, v and n_k . This system of equations can be solved for the spatial variation of all unknowns variables as a function of time. Besides that, we have to specify the initial conditions that determine the state and motion of the fluid at a particular time, plus a set of boundary conditions which constrains the flow. The approach used to solve this problem is presented in Chapter 4 where we discuss the additional physics needed in the context of white dwarfs and thermonuclear supernovae.

[2]Of course, velocity is a vector and it has 3 spatial component. We know it. But we simplify the discussion to just ρ, s, v and n_k as a single variable each one.

Chapter 3

Astrophysical Contents

Our sun, by the way... may become a white dwarf some day but apparently will never become a supernova.

– Isaac Asimov (1919-1992)

After the establishment of the theoretical fundamentals of hydrodynamics as a non-equilibrium phenomena in the last chapter we now turn to the synthesis of the astrophysics of white dwarf matter focusing on the practical aspects relevant to the objective of this work: the equation of state, the transport coefficients and the fusion reaction rates.

3.1 Equation of state: How to hold the star?

The equation of state of white dwarf matter is essentially governed by the degenerate electron gas. Further contributions come from the photon gas, the nuclei, and from electron-positron pair creation at high temperatures. We will neglect solidification effects, allowing the treatment of the nuclei as an ideal gas. Corrections due to Coulomb interaction between electrons and baryons are only marginal and thus will be neglected here. This leads to the following equation of state:

$$p(\rho, T) = p_{\mathrm{rad}} + p_{\mathrm{ion}} + p_{\mathrm{ele}} + p_{\mathrm{pos}}, \tag{3.1}$$

where the subscripts *rad*, *ion*, *ele* and *pos* represent the contributions due to radiation, ions, electrons and positrons, respectively.

3.1.1 Radiation gas

The radiation parcel is that of a thermal radiation in local thermodynamic equilibrium with matter, whose the pressure and specific internal energy are

$$p_{\text{rad}} = \frac{aT^4}{3} \tag{3.2}$$

$$u_{\text{rad}} = \frac{3p_{\text{rad}}}{\rho} \tag{3.3}$$

where a is the radiation density constant.

3.1.2 Ionized ideal gas

For a completely ionized material, the number density of free ions in the material is given by

$$n_{\text{ion}} = \rho N_A \sum_k \frac{X_k}{A_k} \tag{3.4}$$

where X_k is the mass fraction of a given isotope. We can define the mean molecular weight per ion μ as

$$\frac{1}{\mu} = \sum_k \frac{X_k}{A_k}. \tag{3.5}$$

The ion parcel is that of an ideal gas, whose the pressure and specific internal energy are

$$p_{\text{ion}} = n_{\text{ion}} kT \tag{3.6}$$

$$u_{\text{ion}} = \frac{3}{2}\frac{p_{\text{ion}}}{\rho} \tag{3.7}$$

where k is the Boltzmann's constant.

3.1.3 Semi-degenerate fermion gas

According to the Pauli principle, each quantum level is either occupied by one electron or is vacant. Thus, non-interacting electrons (or only weakly interacting) obey the Fermi-Dirac distribution function [e.g., 101]. From statistical mechanics, the number density of electrons having momenta between p and $p + dp$ is

$$n_{\text{ele}}(p)\mathrm{d}p = \frac{8\pi^2 \mathrm{d}p}{h^3} \frac{1}{e^{-(\mu+\epsilon)/k_B T} + 1} = \frac{8\pi^2 \mathrm{d}p}{h^3} q(\eta, x), \tag{3.8}$$

where $x = \epsilon/k_B T$ and $\eta = \mu/k_B$, with μ being the chemical potential and ϵ the kinetic energy (not including the rest mass energy). The Figure 3.1a represents the occupation number q for electrons as a function of x for different values of η.

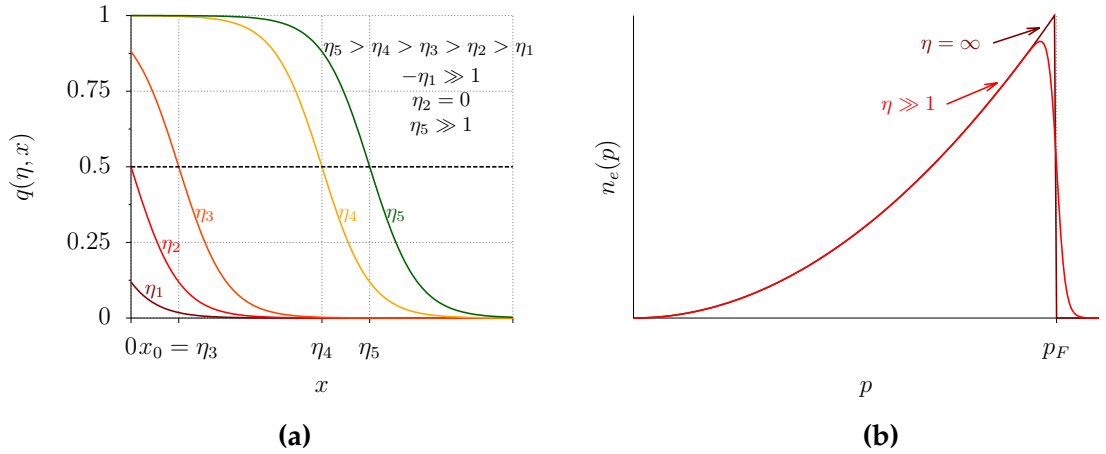

Figure 3.1: (a) The occupation number q for electrons as a function of $x = \epsilon / k_B T$. **(b)** The distribution function $n_e(p)$ for great degeneracy (*red line*) and for a complete degeneracy (*darker line*).

A most significant property of a electron gas is that at $T = 0$ (i.e., a completely degenerate gas[1]), $n_{\text{ele}}(p) > 0$ for $p \leq p_F$ and $n_{\text{ele}}(p) = 0$ otherwise, so that particle motion no cease at $T = 0$. This is completely different of a ideal gas, which the particle motion ceases at the absolute zero of temperature. Therefore, in a white dwarf star at zero temperature (or temperature below the Fermi energy) the velocities of the electrons are great enough to supply the pressure required to keep the star from collapsing under its own gravity.

As presented by Cox & Giuli [102] (where many useful tables and others references can be found) the general expressions for electron density, pressure, internal energy can be write, in terms of dimensionless variables η and the relativistic parameter $\beta = k_B T / m_e c^2$, in parameterized form

$$n_{\text{ele}} = \frac{8\pi\sqrt{2}}{h^3} m_e^3 c^3 \beta^{3/2} \left[F_{1/2}(\eta, \beta) + \beta F_{3/2}(\eta, \beta) \right] \tag{3.9}$$

$$p_{\text{ele}} = \frac{16\pi\sqrt{2}}{3h^3} m_e^4 c^5 \beta^{5/2} \left[F_{3/2}(\eta, \beta) + (1/2)\beta F_{5/2}(\eta, \beta) \right] \tag{3.10}$$

$$u_{\text{ele}} = \frac{8\pi\sqrt{2}}{h^3} \frac{m_e^4 c^5}{\rho} \beta^{5/2} \left[F_{3/2}(\eta, \beta) + \beta F_{5/2}(\eta, \beta) \right] \tag{3.11}$$

where p_{ele} and u_{ele} are the electrons pressure and the electrons energy density. The functions F_k are the generalized Fermi-Dirac integrals defined by

$$F_k(\eta, \beta) = \int_0^\infty \frac{x^k (1 + (\beta/2)x)^{1/2}}{\exp(-\eta + x) + 1} dx \tag{3.12}$$

[1] Nuclei and nucleons have effects of degeneracy in most higher densities, about $\sim 10^{14}$ g/cm^3 due to their high mass.

and can be calculated from approximated expansions for high- and non-degenerate regimes or numerically, as presented in Appendix A.

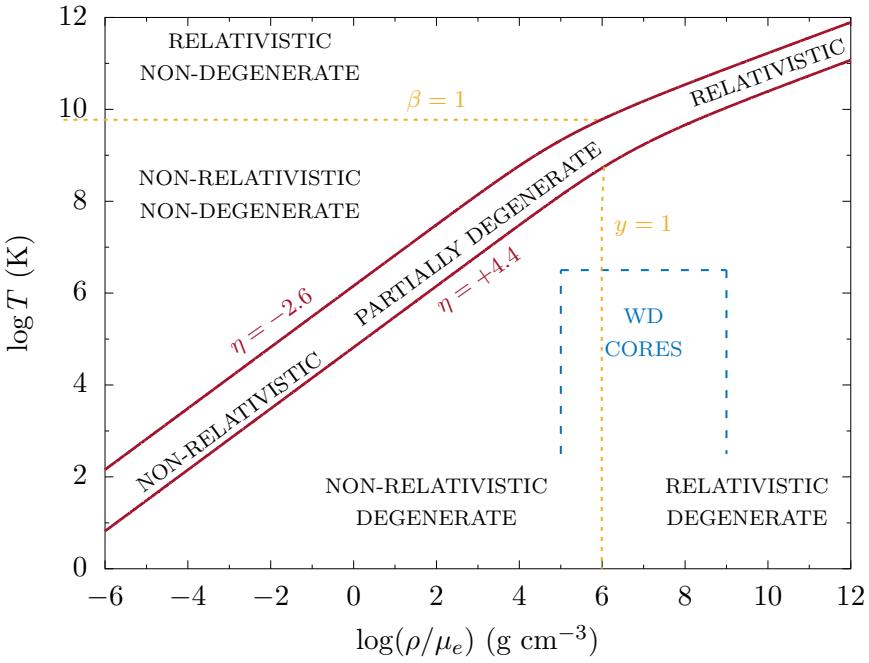

Figure 3.2: Mapping of degenerate phases and relativistic regimes for an electron gas.

At sufficiently high temperatures ($\gtrsim 10^9$ K) an appreciable fraction of photons in the Planckian distribution will have energies in excess of $2m_ec^2$, the necessary energy to create an electron-positron ($e^{\pm}$) pair. Additionally, the finite cross section for pair production and annihilation, represented by the reaction

$$e^- + e^+ \rightleftarrows \gamma, \tag{3.13}$$

cause the equilibrium concentration of $e^{\pm}$ pairs be very large, especially at very high temperatures. The condition for chemical equilibrium establishes that

$$\eta + \eta_+ = 0 \tag{3.14}$$

since $\eta_{\rm pho} = 0$ and η_+ is the reduced chemical potential for positrons. The expression for the number density of positrons is then

$$n_{\rm pos} = \frac{8\pi}{h^3} \int_0^\infty \frac{p^2 \mathrm{d}p}{e^{+\eta + (2mc^2+\epsilon)/k_BT} + 1} \tag{3.15}$$

where we add to the positron energy ϵ the pair rest mass energy $2mc^2$.

Just as before, the general expressions for the number density, the pressure and

the specific internal energy of positrons can be written in the parameterized form

$$n_{\rm pos} = \frac{8\pi\sqrt{2}}{h^3} m_e^3 c^3 \beta^{3/2} \left[F_{1/2}(-\eta - 2/\beta, \beta) + \beta F_{3/2}(-\eta - 2/\beta, \beta)\right], \tag{3.16}$$

$$p_{\rm pos} = \frac{16\pi\sqrt{2}}{3h^3} m_e^4 c^5 \beta^{5/2} \left[F_{3/2}(-\eta - 2/\beta, \beta) + (\beta/2) F_{5/2}(-\eta - 2/\beta, \beta)\right], \tag{3.17}$$

$$u_{\rm pos} = \frac{8\pi\sqrt{2}}{h^3} \frac{m_e^4 c^5}{\rho} \beta^{5/2} \left[F_{3/2}(-\eta - 2/\beta, \beta) + \beta F_{5/2}(-\eta - 2/\beta, \beta)\right] + \frac{2mc^2 n_{\rm pos}}{\rho}. \tag{3.18}$$

If ions are present in the mixture, then some electrons present are ionization electrons and others are from $e^{\pm}$ pairs. The requirement of electron neutrality leads to the condition

$$n_{\rm ele}^{\rm (m)} = N_A \rho / \mu_e = n_{\rm ele} - n_{\rm pos} \tag{3.19}$$

which permits η to be calculated as a function of $n_{\rm ele}^{\rm (m)}$ (or ρ) and T using the Eq.(3.9) and Eq.(3.16). Then $\eta = \eta(n_{\rm ele}^{\rm (m)}, T)$ is given, in general, in tabular form by numerical calculations. The mean molecular weight per free electron μ_e present in (3.19) is defined by

$$\frac{1}{\mu_e} = \sum_k \frac{X_k Z_k}{A_k} \tag{3.20}$$

The various regions of degeneracy of the electron gas on the $\rho - T$ plane are represented in Figure 3.2. The lines of constant η correspond to the band demarcation between non-degenerate and degenerate phases, whose the range $-2.6 \leq \eta \leq 4.4$ (solid lines) represent the partial degeneracy. The regions of non-degenerate and degenerate phases, as well as non-relativistic and relativistic regime, are indicated explicitly. The horizontal line along which $\beta = k_B T / mc^2 = 1$ divide the N.R. ($\beta \ll 1$) from E.R. ($\beta \gg 1$) regimes in the non-degenerate phase. The vertical line along which $y = p_F / mc = 1$ divide the N.R. ($y \ll 1$) from E.R. ($y \gg 1$) regimes in the degenerate phase. The location of the white dwarf cores is also indicated roughly in Figure 3.2.

3.2 Opacities: How does heat propagate?

In the stellar plasma, the internal energy may be transported independently of the flow of the medium. Under the conditions encountered in WD cores, the transport of energy by photons (radiative) and electrons (conductive) may be the dominant mechanisms.

In the radiative diffusion approximation [e.g., 103, Ch. 4], the radiative flux at

any point is related to the photon energy density u_ν by the Fick's law

$$\boldsymbol{j}_\nu = -\frac{1}{3}\frac{c}{\kappa_\nu \rho}\boldsymbol{\nabla} u_\nu, \tag{3.21}$$

with the energy density given by the Planck photon frequency distribution, since photons are in LTE with the material temperature T, written as

$$u_\nu = \frac{4\pi}{c}B_\nu(T) = \frac{4\pi}{c}\frac{2h\nu^3}{c^2}\left(\frac{1}{e^{h\nu/k_BT}-1}\right). \tag{3.22}$$

The radiative flux integrated over all frequencies is then

$$\boldsymbol{q}_{\text{rad}} = \int_0^\infty \boldsymbol{j}_\nu \, \mathrm{d}\nu = -\frac{4\pi}{3\rho}\boldsymbol{\nabla} T \int_0^\infty \frac{1}{\kappa_\nu}\frac{\mathrm{d}B_\nu}{\mathrm{d}T}\, \mathrm{d}\nu, \tag{3.23}$$

and with the help of the Rosseland mean radiative opacity definition, i.e., the average opacity harmonically weighted over the temperature derivative of the Planck curve,

$$\frac{1}{\kappa_{\text{rad}}} = \frac{\int_0^\infty \frac{1}{\kappa_\nu}\frac{\mathrm{d}B_\nu}{\mathrm{d}T}\, \mathrm{d}\nu}{\int_0^\infty \frac{\mathrm{d}B_\nu}{\mathrm{d}T}\, \mathrm{d}\nu} = \frac{\pi}{ac}\frac{1}{T^3}\int_0^\infty \frac{1}{\kappa_\nu}\frac{\mathrm{d}B_\nu}{\mathrm{d}T}\, \mathrm{d}\nu, \tag{3.24}$$

the radiative flux can be expressed as

$$\boldsymbol{q}_{\text{rad}} = -\frac{4acT^3}{3\kappa_{\text{rad}}\rho}\boldsymbol{\nabla} T. \tag{3.25}$$

Heat transported by electrons is defined by Fourier's Law, which states that heat flows in a medium from higher to lower temperatures at a rate proportional to the temperature gradient

$$\boldsymbol{q}_{\text{cond}} = -\lambda_e \boldsymbol{\nabla} T \tag{3.26}$$

where λ_e is the thermal conductivity by the electrons in the medium. To put this equation in the form analogous to the radiative diffusion equation, one defines the electron conductive opacity, κ_{cond}, such that

$$\kappa_{\text{cond}} = \frac{4acT^3}{3\lambda_e \rho}, \tag{3.27}$$

and the conductive heat flow is then

$$\boldsymbol{q}_{\text{rad}} = -\frac{4acT^3}{3\kappa_{\text{cond}}\rho}\boldsymbol{\nabla} T. \tag{3.28}$$

Since the total energy flux is the sum of the radiative (3.25) and heat flux by

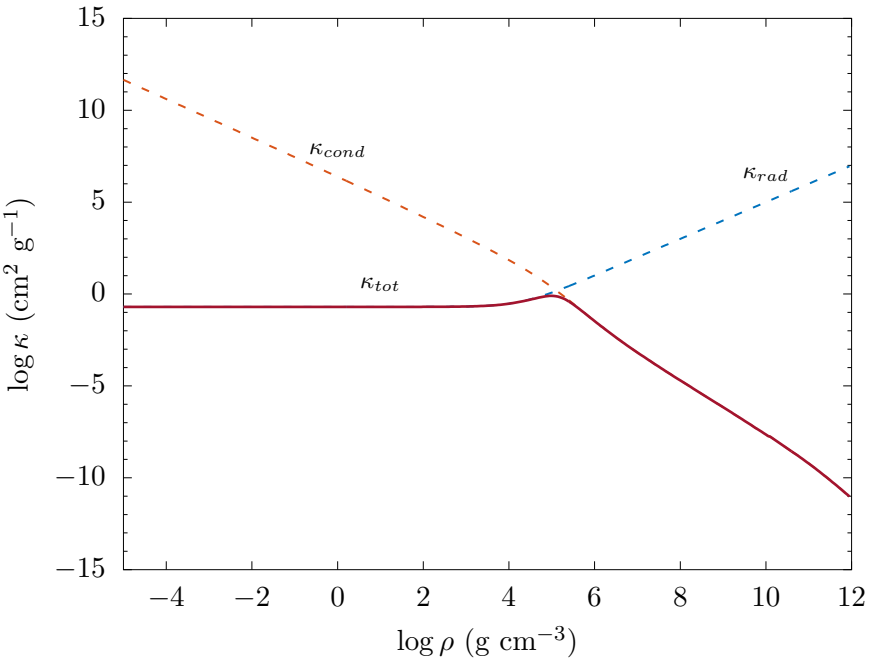

Figure 3.3: The total opacity κ_{tot} (*red solid line*) as a function of density ρ for temperature $T = 10^8$ K and pure carbon composition. The radiative κ_{rad} (*blue dashed line*) and conductive κ_{cond} (*orange dashed line*) opacity are represented as reference.

---

electron conduction (3.28),

$$\boldsymbol{q} = -\frac{4acT^3}{3\kappa_{\text{tot}}\rho}\boldsymbol{\nabla} T, \tag{3.29}$$

the energy transport by electron conduction and by photon radiation are competing processes, with the most energy transported by the process encountering the smallest resistance. Therefore the total opacity of stellar matter [e.g., 11] can be written as

$$\frac{1}{\kappa_{\text{tot}}} = \frac{1}{\kappa_{\text{rad}}} + \frac{1}{\kappa_{\text{cond}}}, \tag{3.30}$$

where κ_{rad} and κ_{cond} are the radiative and conductive opacities, respectively. The Figure 3.3 represents the total κ_{tot}, the radiative κ_{rad} (*blue dashed line*) and conductive κ_{cond} opacities as a function of density ρ for temperature $T = 10^8$ K and pure carbon composition. The radiative opacity is dominant at low density and the conductive opacity is dominant at high densities. A good description and review of opacity can be seen in Ref.[104].

3.2.1 Radiation Opacity

For typical stellar densities and temperatures, the main radiative processes are: the scattering of photons by free electrons, in Thomson or Compton scattering; and

the absorption of photons by free electrons and electrons bound in atoms, as inverse bremsstrahlung, photoelectric absorption and line absorption. In much higher densities and temperatures, as in compact stars or supernovae, other processes such as pair production and photo-nuclear absorption may become important.

At low density and low temperature, the fully ionized gas has opacity dominated by Thompson electron scattering. This is given for electron or photon with thermal energies below the rest mass energy of electron where the Thomson scattering describes the process very well. The opacity in this case is

$$\kappa_{es} = \frac{n_e \sigma_e}{\rho} \tag{3.31}$$

where σ_e is the Thomson cross-section of the electron

$$\sigma_e = \frac{8\pi}{3}\left(\frac{e^2}{m_e c^2}\right) \tag{3.32}$$

and n_e is the electron density given by (3.19). The associated electron scattering opacity is then

$$\kappa_{es} = N_A \sigma_e / \mu_e = 0.4/\mu_e \text{ cm}^2 \text{ g}^{-1} \tag{3.33}$$

in cgs units.

Indeed, free electrons can absorb a photon in the vicinity of an ion, the inverse of normal bremsstrahlung process. The opacity due to free-free electronic transitions can be approximated with the Kramers formula, $\kappa = \kappa_0 \rho^n T^{-s}$, more explicitly as

$$\kappa_{\text{ff}} \approx 10^{23} \frac{\bar{Z}^2}{\mu_e \mu} \rho T^{-7/2} \tag{3.34}$$

where $\bar{Z}$ is the mean charge of the stellar plasma.

Therefore, the total radiative opacity may be well approximated by the following sum

$$\kappa_{\text{rad}} = \kappa_{es} + \kappa_{\text{ff}}, \tag{3.35}$$

because each parcel contributes incoherently.

3.2.2 Conductive Opacities

At very high density and low temperature, as in WD degenerate core, the radiative opacity becomes very high and the electron thermal conductivity becomes a much more efficient heat carrier.

Using the kinetic method [105] in which the effective electron scattering rate ν

does not depend on the electron velocity, one can write

$$\lambda_e = \frac{\pi^2 n_e k_B T}{3 m_e^* \nu} \tag{3.36}$$

where $m_e^* = m_e \gamma$, and $\gamma = \sqrt{1 + (p_F / m_e c)^2}$ is the relativistic density parameter.

In a fully ionized plasma, ν is determined by electron-ion and electron-electron Coulomb collisions. The effective frequencies of different kinds of collisions simply add up following the *Matthiessen rule* [106], i.e., $\nu = \nu_{ei} + \nu_{ee}$ [e.g., 105, 107]. Although the electron-ion *ei* and electron-electron *ee* collision frequencies can be calculated from the kinetic theory. The recent development in this area is beyond the scope of this thesis.

We use the recent results from Cassisi *et al.* [108] that update the previous calculations by Hubbard & Lampe [106], Itoh and coworkers [109, 110, 111, 112, 113, 114], and Yakovlev and coworkers [115, 116, 117, 118], extensively used in the literature. They improve upon Hubbard & Lampe by including an updated treatment of both the *ei* scattering and the *ee* scattering for strongly coupled and relativistic plasma, and are not restricted to the specific mixtures published by Hubbard & Lampe. The enhancements are mainly the *ee* scattering, accurate treatment of the *ei* scattering at high densities, and the fact that their results extend to the regimes of partial degeneracy ($T > T_F$) and weak ion coupling. The Figure 3.4 represent the resulting electron thermal conductivity for different values of temperature.

3.3 Thermonuclear Reactions: How to burn the material and change the chemical composition?

Nuclear reactions are very important in cataclysmic events [e.g., 119]. They determine nucleosynthesis in stellar explosions, such as type I supernovae, as well as ignition and burning in accreting stars [120]. The ignition conditions are sensitive to the ^{12}C and ^{16}O abundance and to thermonuclear reaction rates [70]. Recent advances have been made to determine the astrophysical S-factor at stellar energies, typically lower than the current accessible range of low-energy fusion experiments [121, 122, 123, 124].

Although we know that in high-density cores of white dwarfs thermonuclear reactions are strongly affected by plasma effects [125], we shall concentrate our efforts just on the thermonuclear reaction network to decrease the amount of ingredients considered. Especially because there is a current discussion about reaction rates at very high densities [e.g., 126, 127, 128, 129]. There are several books that present the classic treatment of thermonuclear reaction. The following explanation is based on

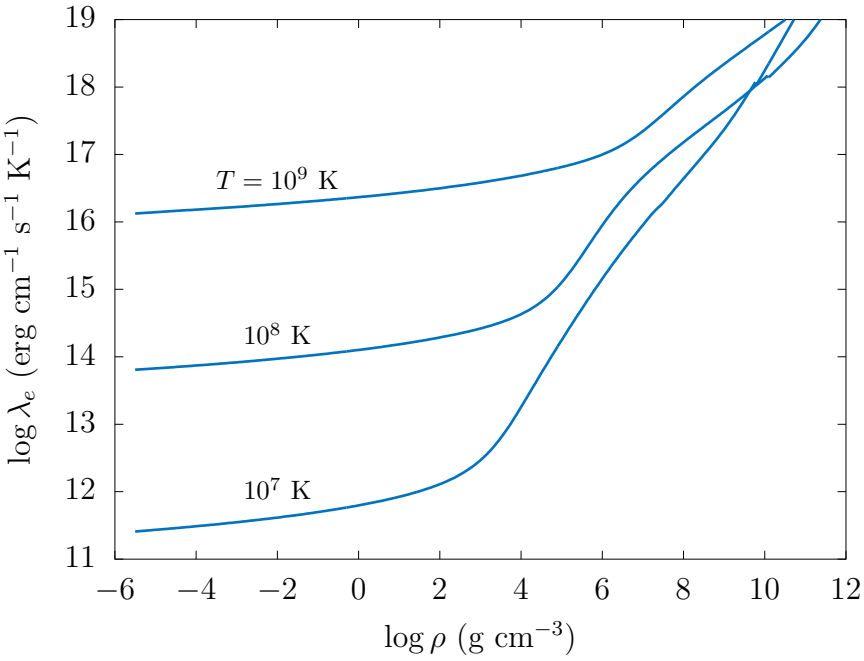

Figure 3.4: The electron thermal conductivity λ_e as a function of density ρ for different values of temperature T.

the excellent description by Iliadis [130] and Clayton [131].

3.3.1 Fusion Reactions

In a reaction involving four species, $a(b,c)d$, where both projectile a and target b are represented by particles with rest mass, the reaction rate is well described by

$$r_{ab} = (1+\delta_{ab})^{-1} n_a n_b \langle \sigma v \rangle_{ab} \tag{3.37}$$

where $\langle \sigma v \rangle_{ab}$ is the pair reaction rate, n_a and n_b are the number densities of the interacting particles, and δ_{ab} is the Kronecker delta to avoid counting each pair of identical particles twice.

The nuclei in stellar plasma, with the exception of neutron stars, are always non-degenerate. In thermodynamic equilibrium, the nuclei are non-relativistic with the distribution of relative velocities well described by a Maxwell-Boltzmann distribution [e.g., 131, § 4-2]. Then, we may write the reaction rate per particle pair $\langle \sigma v \rangle_{ab}$ more explicitly in the form

$$\lambda_{ab} \equiv \langle \sigma v \rangle_{ab} = \left(\frac{8}{\pi m_{ab}} \right)^{1/2} \frac{1}{(k_B T)^{3/2}} \int_0^\infty E \sigma(E) e^{-E/(k_B T)} dE \tag{3.38}$$

where E is the center-of-mass energy. Clearly, the reaction rate depends critically on

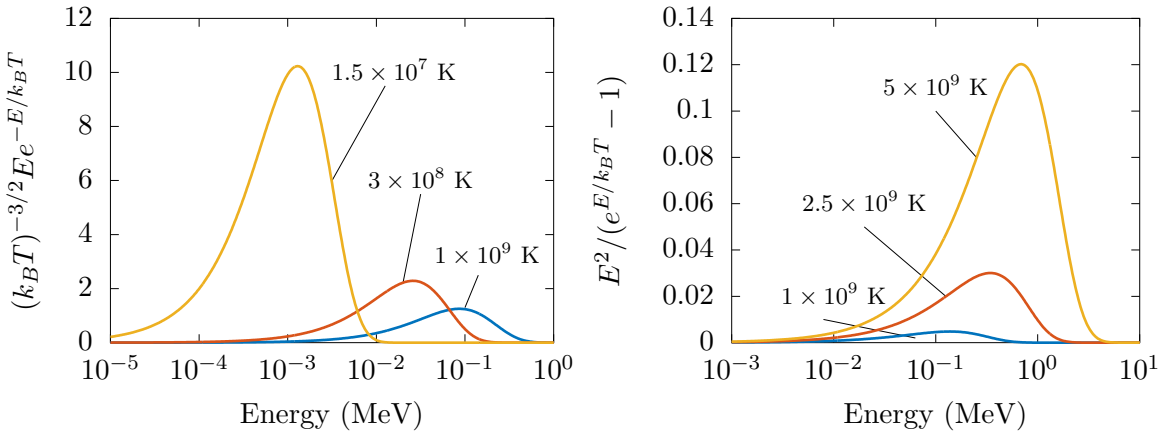

Figure 3.5: (a) The factor $(kT)^{-3/2}Ee^{-E/kT}$ in the expression (3.38) for fusion reaction rate at three different temperatures, $T = 1.5 \times 10^7$ K (*yellow line*), $T = 3 \times 10^8$ K (*orange line*) and $T = 1 \times 10^9$ K (*blue line*). **(b)** The factor $E^2/(e^{E/k_BT} - 1)$ in the expression (3.40) for the photo-disintegration reactions rate at three different temperatures, $T = 1 \times 10^9$ K (*blue line*), 2.5×10^9 K (*orange line*), and 5×10^9 K (*yellow line*).

the cross section σ which differs for each nuclear reaction.

The Figure 3.5a shows the factor $(kT)^{-3/2}Ee^{-E/kT}$ versus energy E for three different scenarios: (i) the Sun core ($T = 1.5 \times 10^7$ K), (ii) a nova ($T = 3 \times 10^8$ K), and (iii) a supernova ($T = 1 \times 10^9$ K). Each curve increases linearly at small energies, reaches a maximum at $E = k_BT$, and then decreases exponentially and approaches zero for large values of E. The maxima of the curves occur at $E_{\max} = k_BT = 1.3$ keV, 26 keV, and 86 keV.

3.3.2 Photo-disintegration Reactions

If the reaction involves a photon, then the process $a(\gamma, c)d$ is denominated a photo-disintegration reaction. The reaction rate in this case is given by

$$r_{a\gamma} = n_a \int_0^\infty c n_\gamma(E)\sigma(E)\, \mathrm{d}E \tag{3.39}$$

since the number density of photons is not constant, but depends on the stellar temperature and on the γ-ray energy.

The number of photon is given by the Planck radiation law, such that the photo-disintegration decay constant at a given temperature is

$$\lambda_{a\gamma} = \frac{r_{a\gamma}}{n_a} = \frac{8\pi}{h^3c^2}\int_{E_t}^\infty \frac{E}{e^{E/k_BT} - 1}\sigma(E)\, \mathrm{d}E \tag{3.40}$$

where E is the photon energy, and E_t is the threshold energy $E_t = -Q_{a(\gamma,c)d}$ since most photo-disintegration reactions are endothermic ($Q_{a(\gamma,c)d} < 0$). We can note that $\lambda_{a\gamma}$ does not depend on the stellar density.

The Figure 3.5b shows the factor $E/(e^{E/k_BT} - 1)$ versus γ-ray energy for three different scenarios: (i) $T = 1.5 \times 10^9$, (ii) $T = 2.5 \times 10^9$ K, and (iii) $T = 5 \times 10^9$ K. The maxima of the curves occur at $E_{\gamma,\max} \approx 1.6 k_B T = 140$ keV, 349 keV and 700 keV. The number of photons is not conserved, but is determined by the conditions of local thermal equilibrium.

3.3.3 Abundance Evolution and Energy Generation

For a single reaction involving two nuclei a and b in the stellar plasma, the rate of change of the number density of nucleus a due to reaction with nucleus b can be expressed as

$$\frac{\mathrm{d}n_a}{\mathrm{d}t} = -(1 + \delta_{ab}) r_{a(b,c)d} = -n_a n_b \langle \sigma v \rangle_{ab} = -\frac{n_a}{\tau_a} \tag{3.41}$$

and the Kronecker delta appears since for identical nuclei each reaction destroys two particles. The quantity τ_a is the mean lifetime of the nuclear species a in the stellar plasma.

Since the nuclear energy released per reaction is given by the Q-value, the energy production per unit time and unit mass is then expressed by

$$\epsilon_{a(b,c)d} = \frac{Q_{a(b,c)d} \lambda_{a(b,c)d}}{\rho} \tag{3.42}$$

or, using the (3.41), in terms of the number density

$$\epsilon_{a(b,c)d} = -\frac{Q_{a(b,c)d}}{\rho(1 + \delta_{ab})} \left(\frac{\mathrm{d}n_a}{\mathrm{d}t} \right)_b . \tag{3.43}$$

The total releases energy during a time interval is obtained from

$$\int \epsilon_{a(b,c)d} \, \mathrm{d}t = -\int_{n_a^{(\mathrm{ini})}}^{n_a^{(\mathrm{fin})}} \frac{Q_{a(b,c)d}}{\rho(1 + \delta_{ab})} \left(\mathrm{d}n_a \right)_b = \frac{Q_{a(b,c)d}}{\rho(1 + \delta_{ab})} \left(\Delta n_a \right)_b \tag{3.44}$$

where $(\Delta n_a)_b = n_a^{(\mathrm{ini})} - n_a^{(\mathrm{fin})}$ is the change in the number density of nucleus a due to the reaction with nucleus b.

In general, there are several nuclear processes (reactions, photo-disintegration, β-decays) influencing together on the abundance evolution of a particular nucleus in a stellar plasma. Then, in this case, the abundance evolution of nucleus a is given

by the differential equation

$$\begin{aligned}\frac{\mathrm{d}n_a}{\mathrm{d}t} = & \left[\sum_{c,d} n_c n_d \langle\sigma v\rangle_{c(d,b)a} + \sum_f \lambda_{f(\beta,)a} n_f + \sum_g \lambda_{g(\gamma,)a} n_g\right] \\ & - \left[\sum_b n_b n_a \langle\sigma v\rangle_{a(b,x)y} + \sum_h \lambda_{a(\beta,)h} n_a + \sum_k \lambda_{a(\gamma,)k} n_a\right]\end{aligned} \tag{3.45}$$

The three terms in the first parenthesis represent all processes producing nucleus a: the sum over all reactions producing nucleus a via fusion reactions between c and d; the sum over all β-decays of nuclei f leading to a; and the sum over all photo-disintegration of nuclei g leading to a. The terms in the second parenthesis stand for all processes destroying nucleus a: the sum over all fusion reactions between a and b; the sum over all β-decays of nuclei a; and the sum over all photo-disintegration of nuclei a.

If the mass density changes during the nucleosynthesis, it is more advantageous to express (3.46) in terms of the abundance of species a, X_a. In our simulations we will treat the problem of explosive nucleosynthesis being more appropriate to work with the evolution of the abundance X_a instead of number density n_a.

Another important consideration is that if reactions produce electrons, positrons, or γ-rays, then their energy is retained in the stellar plasma. On the other hand, neutrinos are weakly interacting with the medium that they must escape from the site of thermonuclear burning, with the important exceptions for big bang and core collapse supernovae. Since the neutrino energy is usually not deposited in the star, it has to be subtracted from the Q-value when calculating the nuclear energy generation.

3.3.4 Thermonuclear reaction rate

At low energy, typical for astrophysical conditions, the fusion cross section $\sigma(E)$ can be written as a product of three separate energy-dependent factors

$$\sigma(E) = \frac{e^{-bE^{-1/2}}}{E} S(E), \tag{3.46}$$

where $b \equiv \frac{2\pi}{\hbar} Z_a Z_b e^2 \sqrt{m_{ab}/2}$ is the Gamow parameter, E is the center-of-mass kinetic energy of the nuclei, Z_a and Z_b are the charge numbers of the nuclei, and $m_{ab} = m_a m_b/(m_a + m_b)$ is the reduced mass. This parametrization for the fusion cross section removes the strong non-nuclear energy dependence associated with Coulomb barrier penetration by the Gamow factor, $e^{-bE^{-1/2}}$, and the geometrical factor, $1/E$.

The factor $S(E)$ represents the intrinsically nuclear parts of the probability for the occurrence of a nuclear reaction. This factor is a slowly varying function of E

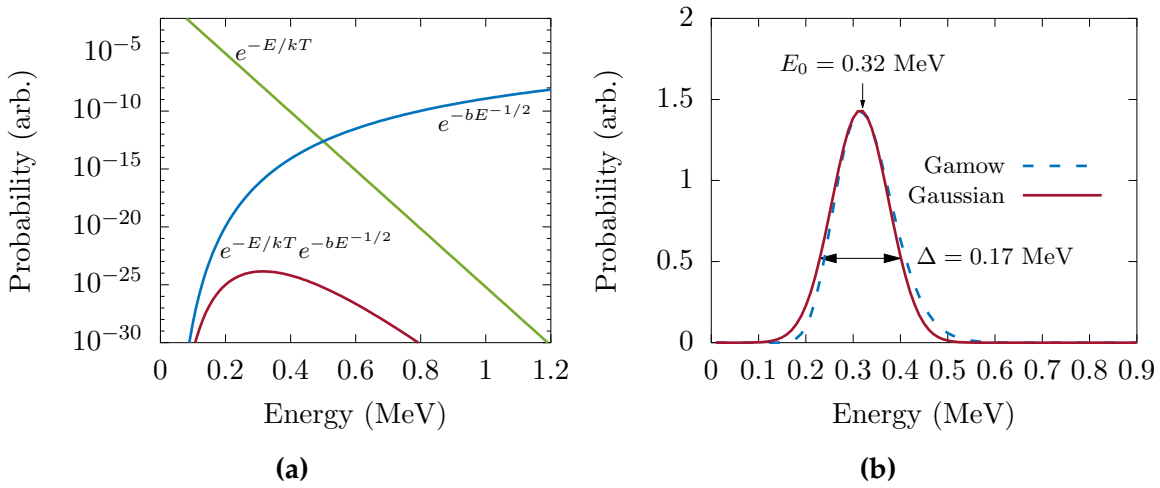

Figure 3.6: (a) The Maxwell-Boltzmann factor e^{-E/k_BT} (*green line*) and the Gamow tunneling factor $e^{-bE^{-1/2}}$ (*blue line*) versus energy for the reaction $^{12}C(\alpha,\gamma)^{16}O$ at $T = 2 \times 10^8$ K. The Gamow's peak product $e^{-E/k_BT}.e^{-bE^{-1/2}}$ (*red line*) is also represented. **(b)** The Gamow peak for the reaction $C^{12}(\alpha,\gamma)O^{16}$ at $T = 0.2$ GK. The curve (*blue dashed line*) is asymmetric about E_0, but it is adequately approximated by a Gaussian (*red solid line*). The width of the Gaussian is presented by Δ.

which can be extrapolated to lower energies relevant to stellar burning, being therefore called astrophysical S-factor. With this definition, we write the non-resonant reaction rate as

$$\langle \sigma v \rangle_{ab} = \left(\frac{8}{\pi m_{ab}}\right)^{1/2} \frac{1}{(k_B T)^{3/2}} \int_0^\infty S(E) e^{-bE^{-1/2}} e^{-E/(k_B T)} \mathrm{d}E \tag{3.47}$$

The integrand in (3.47) has an interesting energy dependence. The factor e^{-E/k_BT} from the Maxwell-Boltzmann distribution goes to zero at large energies, while the term $e^{-bE^{-1/2}}$ from the Gamow factor approaches to zero for small energies. Therefore, the major contribution to the integral comes from energies where the product is near its maximum. The Figure 3.6a illustrates this situation for the reaction $^{12}C(\alpha,\gamma)^{16}O$ at $T = 2 \times 10^8$ K. The green line shows the Maxwell-Boltzmann factor e^{-E/k_BT} and the blue line represents the Gamow factor $e^{-bE^{-1/2}}$. The red line shows the product $e^{-E/k_BT}.e^{-bE^{-1/2}}$ in the integrand of (3.47).

The Gamow peak is appropriately approximated by a Gaussian, as presented in Figure 3.6b for the reaction $C^{12}(\alpha,\gamma)O^{16}$ at $T = 2 \times 10^8$ K. The Gaussian approximation is obtained by a series expansion of the exponential argument

$$\exp\left(-\frac{b}{\sqrt{E}} - \frac{E}{k_B T}\right) \approx \exp\left(-\frac{3E_0}{k_B T}\right) \exp\left[\left(\frac{E - E_0}{\Delta/2}\right)^2\right] \tag{3.48}$$

around the peak energy E_0, energy in which the first derivative with respect to E vanishes,

$$E_0 = \left(\frac{b}{2}\right)^{2/3} (k_B T)^{2/3}, \tag{3.49}$$

with a Gaussian width Δ, obtained from the requirement that the second derivatives match at E_0, written as

$$\Delta = \frac{4}{\sqrt{3}} \sqrt{E_0 k_B T}. \tag{3.50}$$

Since $k_B T \ll E_0$ in astrophysical situations, it is apparent that the width Δ of the Gamow peak is smaller than E_0. The Figure 3.6b shows the Gamow peak and its approximation for the reaction $C^{12}(\alpha, \gamma)O^{16}$ at $T = 2 \times 10^8$ K.

The energy E_0 is the most effective energy for non-resonant thermonuclear reactions.

$$N_A \langle \sigma v \rangle = N_A \left(\frac{2}{m_{ab}}\right)^{1/2} \frac{(k_B T)^{1/2} \Delta}{9 E_0^2} S_0 \tau^2 e^{-\tau} \tag{3.51}$$

with $\tau = 3E_0/(k_B T)$.

The presence of resonances can fully dominate a nuclear cross-section. This occurs at an energy of the incident projectile that matches the energy of an excited state in the compound nucleus. Isolated and narrow resonances are frequently described by means of the Breit–Wigner formula

$$\sigma(E) = \frac{\lambda^2 \omega}{4\pi} \frac{\Gamma_i \Gamma_o}{(E_r - E)^2 + \Gamma^2/4}, \tag{3.52}$$

with

$$\omega = \frac{(2J+1)(1+\delta_{ab})}{(2J_a+1)(2J_b+1)}, \tag{3.53}$$

where J_a and J_b the total spins of the interacting particles a and b, and J the spin of the resonance state in the compound nucleus, E_r is the resonance energy, λ is the de Broglie wavelength.

The reaction rates for a single narrow resonance can be calculated putting (3.52) into (3.38). For narrow resonances, the Maxwell-Boltzmann factor and the partial widths are approximately constant over the total width of the resonance, such that

$$N_A \langle \sigma v \rangle = N_A \left(\frac{2\pi}{m_{ab} k_B T}\right)^{3/2} \hbar^2 e^{-E_r/k_B T} \omega \frac{\Gamma_a \Gamma_b}{\Gamma}. \tag{3.54}$$

The reaction rates for narrow resonances depend only on the energy and the strength of the resonance, $\omega \Gamma_a \Gamma_b / \Gamma$, but not on the exact shape of the cross section curve. This is excellent because for most narrow resonances the partial and total widths are experimentally not known. Indeed, if several narrow and isolated resonances

contribute to the cross section, their contributions to the reaction rate add incoherently.

Two corrections to the non-resonant reaction rate must be considered. The first correction comes from the difference between the area of the asymmetric Gamow peak and the area of the symmetric Gaussian (see Figure 3.6b), being corrected by a multiplicative factor that represents the ratio of the areas under these two curves. A second correction is necessary since for many non-resonant reactions the S-factor is not constant, but varies with energy. As a result of these corrections, one has to replace in (3.51) the constant S_0 by an effective S-factor [132] given by

$$S_{\text{eff}}(E_0) = S(0)\left[1 + \frac{5}{12\tau} + \frac{S'(0)}{S(0)}\left(E_0 + \frac{35}{36}k_BT\right) + \frac{1}{2}\frac{S''(0)}{S(0)}\left(E_0^2 + \frac{89}{36}E_0k_BT\right)\right] \tag{3.55}$$

where $S(0)$ is the S-factor at $E = 0$ and the primes indicate derivatives with respect to E. The first terms in the square bracket correspond to the factor caused by the asymmetry of the Gamow peak, while the other terms arise from corrections caused by the S-factor variation with energy. Explicitly, one finds

$$N_A\langle\sigma v\rangle = \frac{C_1}{T_9^{2/3}}e^{-C_2/T_9^{1/3}}\left(1 + C_3T_9^{1/3} + C_4T_9^{2/3} + C_5T_9 + C_6T_9^{4/3} + C_7T_9^{5/3}\right) \tag{3.56}$$

as a suitable analytic expression for the pair reaction rate.

For the calculation of the total reaction rates, all processes contributing significantly to the reaction mechanism in the effective stellar energy range have to be taken into account. The effective energy range is given by the Gamow peak for reactions induced by charged particles. The various contributions to the total reaction rates can be added incoherently since interferences are negligible, so that

$$N_A\langle\sigma v\rangle_{\text{total}} = \sum_i N_A\langle\sigma v\rangle^i_{\text{resonant}} + N_A\langle\sigma v\rangle_{\text{non-resonant}} \tag{3.57}$$

In this work, we use the total pair reaction rates $N_A\langle\sigma v\rangle_{\text{total}}$ described by (3.57) and tabulated in Table II from Caughlan & Fowler in Ref.[133].

3.3.5 Nuclear Reaction Network

In stellar situations, we have to consider the evolution of not just one nucleus, but of several species simultaneously. For each nuclide we can set up an expression of the form given by (3.46). Such a system of coupled, nonlinear ordinary differential equations is called a nuclear reaction network. There is simplest cases where we may solve the reaction network analytically, but most of the cases this reaction network must be solved numerically [e.g., 120, 134].

The simplest nuclear reaction network is the α-chain only composed of (α, γ) and (γ, α) links among the 13 isotopes ^{4}He, ^{12}C, ^{16}O, ^{20}Ne, ^{24}Mg, ^{28}Si, ^{32}S, ^{36}Ar, ^{40}Ca, ^{44}Ti, ^{48}Cr, ^{52}Fe, and ^{56}Ni. Although very simple an α-chain network gives a thermonuclear energy generation rate that is generally close of the generation rate given by much larger nuclear reaction networks.

3.3.6 Nuclear Statistical Equilibrium

Sometimes the solutions of nuclear reaction networks reveal certain fundamental properties which simplify the interpretation of the results. The most important of these properties are called steady state and equilibrium. A steady-state solution exists if for some part of the reaction network the time derivative of all abundances $\mathrm{d}X_i/\mathrm{d}t$, are zero or nearly zero. This implies that in (3.46) the sum of all destruction terms is balanced by the sum of all creation terms.

At high temperatures and densities, thermonuclear reactions will proceed rapidly and an equilibrium can be established between the various nuclear species present in the medium. Every nuclei in the network is now in equilibrium via strong and electromagnetic interactions and one large quasi-equilibrium group stretches from p, n, α to the iron peak nuclei. The weak interaction do not participate in the equilibrium due to the large mean free path of the neutrinos. This situation is referred to as *nuclear statistical equilibrium* (NSE) [135].

At temperatures $T \gtrsim 3 \times 10^9$ K, the photo-disintegration of silicon will proceed rapidly, releasing protons, neutrons, and alpha particles. In NSE, the decomposition of ^{28}Si during the silicon burning has mainly produced ^{56}Ni (see Figure 4.6a), which is the most tightly bound species with $N = Z$. Therefore, the stellar plasma consists entirely of ^{4}He, ^{28}Si and ^{56}Ni at nuclear statistical equilibrium, with weak interactions neglected. The balance between helium and silicon is given by the Saha equation as

$$\frac{X_{^4\mathrm{He}}^7}{X_{^{28}\mathrm{Si}}} = \left(\frac{\theta}{\rho N_A}\right)^6 \left(\frac{4^7}{28}\right)^{5/2} e^{[7B(^4\mathrm{He}) - B(^{28}\mathrm{Si})]/k_B T} \tag{3.58}$$

and balance between helium and nickel can be written as

$$\frac{X_{^4\mathrm{He}}^{14}}{X_{^{56}\mathrm{Ni}}} = \left(\frac{\theta}{\rho N_A}\right)^{13} \left(\frac{4^{14}}{56}\right)^{5/2} e^{[14B(^4\mathrm{He}) - B(^{56}\mathrm{Ni})]/k_B T} \tag{3.59}$$

with the total mass fraction constraint $\sum_a X_a = 1$, the parameter $\theta = (2\pi k_B T/(N_A h^2))^{3/2}$ and $B(X_a)$ being the binding energy of the isotope X_a.

For a given density, in the lower temperature region ^{56}Ni dominates the composition as displayed in Figure 3.7. However, at higher temperatures ^{4}He is the dominant nucleus. Then as the temperature increases at a given density, an increasing

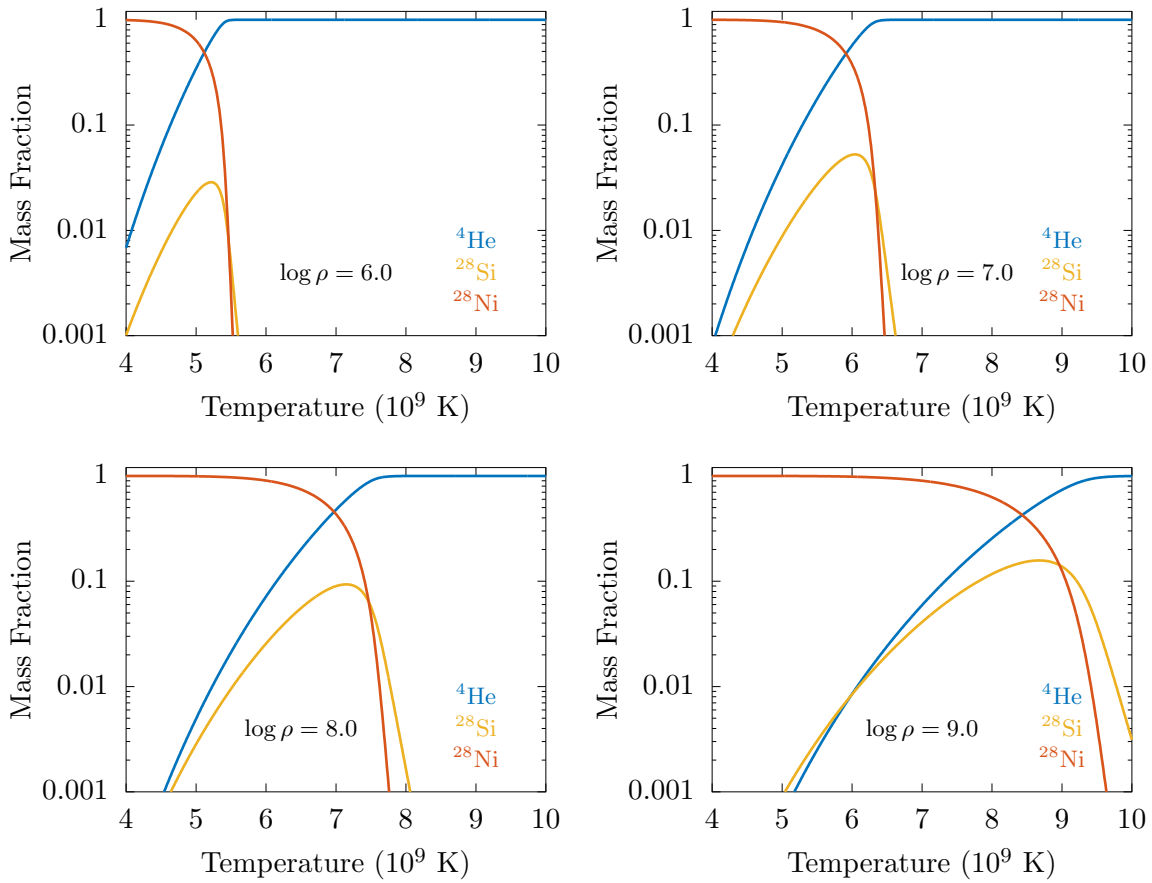

Figure 3.7: The mass fractions under nuclear statistical equilibrium as a function of temperature for different values of density. The point here is that, with rising temperatures at a given density, or with decreasing densities at a given temperature, an increasing fraction of the composition resides in light particles and that this transformation absorbs a large amount of energy.

fraction of the composition resides in α, and the same occurs for decreasing densities at a given temperature.

When we say that at a particular temperature the nuclear reactions are in equilibrium, we mean that this temperature exists long enough for a good approximation to equilibrium to occur. The nuclear gas requires a finite amount of time to adjust to equilibrium. The approximate time (in seconds) to reach nuclear statistical equilibrium for given values of T and ρ can be estimated from the numerical expression [74]

$$\tau_{NSE} = \rho^{0.2} e^{179.7/T_9 - 40.5}. \tag{3.60}$$

At $T = 4 \times 10^9$ K, for example, nuclear statistical equilibrium is established in about 1 h, while at $T = 6 \times 10^9$ K the time is only $\approx 10^{-3}$ s. The high temperatures and densities achieved in the thermonuclear explosion imply that most nuclear re-

actions will take part in nuclear statistical equilibrium or quasi-NSE. Therefore, the nucleosynthesis and nuclear energy generation will in general not be sensitive to individual reaction rates but will depend on reaction Q-values, whose the masses of the nuclides taking part in the nucleosynthesis are well known. We expect current reaction rate uncertainties to play a role only during the ignition phase, mainly due to $^{12}\mathrm{C} + {}^{12}\mathrm{C}$ and $^{12}\mathrm{C} + {}^{16}\mathrm{O}$ reaction rates.

3.4 Gravitational Force

Since $GM_\odot / R_\oplus c^2 \sim 10^{-4}$, general relativistic effects are not relevant to our physical modeling of white dwarfs. Therefore, the self-gravity of the white dwarf star introduces an external force to the hydrodynamical equations:

$$f = -\boldsymbol{\nabla}\Phi \tag{3.61}$$

where Φ is the gravitational potential given by Poisson's equation $\nabla^2\Phi = 4\pi G\rho$. In the one-dimensional simulations, this Poisson's equation can be solved together with the hydrodynamics equations in a beautiful variational principle method.

Chapter 4

Numerical Details

There's no sense in being precise when you don't even know what you're talking about.

– J. von Neumann (1903-1957)

In principle, a full numerical implementation of a system describing the explosive nucleosynthesis and the propagation of shock waves in white dwarf matter would require to solve concomitantly the hydrodynamics equations (Section 2.2) with nuclear reactions (Section 3.3), together with the appropriate transport properties (Section 3.2) and equation of state (Section 3.1).

4.1 One-dimensional Fluid dynamics

We shall concentrate our efforts in one-dimensional simulations. Although, multidimensional simulations are feasible with current computer power, we will not focus on this application because those do not solve the full scale space problem in numerical simulations without approximations. Indeed, we are interested in the best simulation we can do with a one-dimensional hydrodynamic calculations but with the best physical and astrophysical ingredients we can put in this simulation.

4.1.1 Effective Lagrangian Description

Our one-dimensional hydrodynamic calculations use the Effective Lagrangian Method [136] instead of the finite elements method or other standard hydrodynamics algorithms. This formulation is adequate to investigate the formation and propagation of a shock wave as accurate as possible, and it has the advantage of keeping a complete control of the physical quantities, as the balance of energy during the explosion.

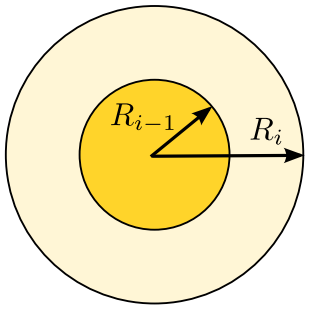

Figure 4.1: Representation of stellar interior using shells. The radii R_i and R_{i-1} are the outer and inner radius of the shell, respectively.

We consider the stellar interior make of N homogeneous spherical shells, so that the dynamics coordinates of the system should be the radial coordinates of the shell surface, $\{R_i\} = \{R_0, R_1, R_2, \ldots, R_N\}$, and $R_0 = 0$ for convention, as represented in Figure 4.1. Physical quantities associated with the shell between R_i and R_{i-1} are characterized by the index i, so the density of such shell is ρ_i, the temperature is T_i, the abundance of isotopes is $\boldsymbol{X}_i$, and others.

The mass of each shell is keep constant over time, and it can be write simply as

$$m_i = \frac{4\pi}{3}\rho_i \left(R_i^3 - R_{i-1}^3\right), \tag{4.1}$$

and the density ρ_i will be uniform within each shell.

The Lagrangian of the system is expressed as

$$\mathcal{L}(\{R_i\}, \{T_i\}, \{\boldsymbol{X}_i\}) = K - \Omega - U \tag{4.2}$$

where K is the total kinetic energy, Ω is the gravitational potential energy and U the internal energy of the fluid.

The kinetic energy can be expressed as a function of R_i and $\dot{R}_i$. The continuity equation gives

$$\frac{1}{r^2}\frac{\mathrm{d}}{\mathrm{d}r}\left(r^2 v(r)\right) = -\frac{\dot{\rho}}{\rho}, \tag{4.3}$$

where $v_i(r)$ is the velocity field and for the spherical shell we found

$$v_i(r) = Ar + B/r^2, \tag{4.4}$$

with the boundary conditions

$$v_i(R_i) = \dot{R}_i \quad \text{and} \quad v_i(R_{i-1}) = \dot{R}_{i-1} \tag{4.5}$$

so

$$A = \frac{R_i^2 \dot{R}_i - R_{i-1}^2 \dot{R}_{i-1}}{R_i^3 - R_{i-1}^3} \tag{4.6}$$

$$B = -\frac{R_i^2 R_{i-1}^2 \left(\dot{R}_i R_{i-1} - \dot{R}_{i-1} R_i\right)}{R_i^3 - R_{i-1}^3}. \tag{4.7}$$

Therefore, the kinetic energy of the shell i is

$$\begin{aligned} K_i &= \frac{1}{2}\rho_i \int_{R_{i-1}}^{R_i} v_i^2(r) 4\pi r^2 \, dr \\ &= \frac{1}{2} \begin{pmatrix} \dot{R}_{i-1} & \dot{R}_i \end{pmatrix} \begin{pmatrix} \Pi_{11}^i & \Pi_{12}^i \\ \Pi_{21}^i & \Pi_{22}^i \end{pmatrix} \begin{pmatrix} \dot{R}_{i-1} \\ \dot{R}_i \end{pmatrix}, \end{aligned} \tag{4.8}$$

with

$$\Pi_{11}^{(i)} = \frac{3}{5} \frac{\xi^3(\xi^3 + 3\xi^2 + 6\xi + 5)}{(\xi^2 + \xi + 1)^3} m_i \tag{4.9}$$

$$\Pi_{12}^{(i)} = \Pi_{21}^{(i)} = \frac{9}{10} \frac{\xi^2(\xi^2 + 3\xi + 1)}{(\xi^2 + \xi + 1)^3} m_i \tag{4.10}$$

$$\Pi_{22}^{(i)} = \frac{3}{5} \frac{(5\xi^3 + 6\xi^2 + 3\xi + 1)}{(\xi^2 + \xi + 1)^3} m_i, \tag{4.11}$$

where ξ is defined as

$$\xi \equiv \frac{R_{i-1}}{R_i} \tag{4.12}$$

and we omit the subscript i to not overload the notation.

The total kinetic energy of the star can be written as

$$K = \frac{1}{2} \sum_{i,j}^{N} \Pi_{ij} v_i v_j, \tag{4.13}$$

with $v_i = \dot{R}_i$, and explicitly

$$\mathbf{\Pi} = \begin{pmatrix} \Pi_{22}^{(1)} + \Pi_{11}^{(2)} & \Pi_{12}^{(2)} & 0 & 0 & \cdots & 0 \\ \Pi_{21}^{(2)} & \Pi_{22}^{(2)} + \Pi_{11}^{(3)} & \Pi_{12}^{(3)} & 0 & \cdots & \vdots \\ 0 & \Pi_{21}^{(3)} & \Pi_{22}^{(3)} + \Pi_{11}^{(4)} & \Pi_{12}^{(4)} & \cdots & \vdots \\ 0 & 0 & & & & 0 \\ \vdots & \vdots & \vdots & & & 0 \\ \vdots & \vdots & 0 & \Pi_{21}^{(n-1)} & \Pi_{22}^{(n-1)} + \Pi_{11}^{(n)} & \Pi_{12}^{(n)} \\ 0 & \cdots & 0 & 0 & \Pi_{21}^{(n)} & \Pi_{22}^{(n)} \end{pmatrix}, \tag{4.14}$$

is a symmetric tri-diagonal matrix.

The gravitational energy can be calculated by

$$\Omega = -\frac{G}{2} \iint d^3\mathbf{r_1} d^3\mathbf{r_2} \frac{\rho(\mathbf{r_1})\rho(\mathbf{r_2})}{|\mathbf{r_1} - \mathbf{r_2}|}. \tag{4.15}$$

We can associate an individual contribution to each shell such that $\Omega = \sum_{i=1}^{N} \Omega_i$, where Ω_i has two contributions: the first from the gravitational interaction of the shell with its interior shells (Gauss' Law); and the contribution from the self-interaction. Together, both contributions are expressed by

$$\Omega = -G \sum_{i=1}^{N} \frac{3}{10} \frac{m_i}{R_i} \Big[f(\xi) m_i + g(\xi) M_{i-1} \Big], \tag{4.16}$$

with

$$\begin{aligned} f(\xi) &= \frac{3\xi^3 + 6\xi^2 + 4\xi + 2}{(\xi^2 + \xi + 1)^2} \\ g(\xi) &= 5 \frac{\xi + 1}{(\xi^2 + \xi + 1)}, \end{aligned}$$

and M_{i-1} is the total mass of its internal shells, $M_{i-1} = \sum_{j=1}^{i-1} m_j$.

The internal energy is purely

$$U = \sum_{i=1}^{N} u(\rho_i, T_i, \mathbf{X}_i) m_i, \tag{4.17}$$

where u is the internal energy per gram of the material, ρ_i is the shell mass density and T_i is the shell temperature.

The equations of motion are derived from the Euler-Lagrange equations as

$$\frac{\mathrm{d}}{\mathrm{d}t}\left(\frac{\partial \mathcal{L}}{\partial \dot{R}_i}\right) = \frac{\partial \mathcal{L}}{\partial R_i}, \tag{4.18}$$

resulting in

$$\mathbf{\Pi}\frac{\mathrm{d}^2\mathbf{R}}{\mathrm{d}t^2} = \mathbf{\Theta}\frac{\mathrm{d}\mathbf{R}}{\mathrm{d}t} + \mathbf{F}, \tag{4.19}$$

where $\mathbf{\Pi}$ is the kinetic matrix given by Eq.(4.14) and $\mathbf{\Theta} = -\frac{1}{2}\mathrm{d}\mathbf{\Pi}/\mathrm{d}t$, and the force term $\mathbf{F}$ is

$$\mathbf{F} = \begin{pmatrix} 4\pi R_1^2(\Delta p_{(1)} + \Delta q_{(1)}) - \frac{G}{R_1^2}\left[f_1^{(1)} m_1^2 + f_2^{(2)} m_2^2 + g_2^{(2)} m_2 M_1\right] \\ 4\pi R_2^2(\Delta p_{(2)} + \Delta q_{(2)}) - \frac{G}{R_2^2}\left[f_1^{(2)} m_2^2 + f_2^{(3)} m_3^2 + g_1^{(2)} m_2 M_1 + g_2^{(3)} m_3 M_2\right] \\ \vdots \\ 4\pi R_i^2(\Delta p_{(i)} + \Delta q_{(i)}) - \frac{G}{R_i^2}\left[f_1^{(i)} m_i^2 + f_2^{(i+1)} m_{i+1}^2 + g_1^{(i)} m_i M_{i-1} + g_2^{(i+1)} m_{i+1} M_i\right] \\ \vdots \\ 4\pi R_n^2(p_{(n)} + q_{(n)}) - \frac{G}{R_n^2}\left[f_1^{(n)} m_n^2 + g_1^{(n)} m_n M_{n-1}\right] \end{pmatrix}, \tag{4.20}$$

with $\Delta p_{(i)} \equiv p_i - p_{i+1}$ and $\Delta q_{(i)} \equiv q_i - q_{i+1}$, using the boundary condition $p_{n+1} = q_{n+1} = 0$, and

$$f_1^{(i)} = \frac{3}{5}\frac{(5\xi^3 + 6\xi^2 + 3\xi + 1)}{(\xi^2 + \xi + 1)^3} \tag{4.21}$$

$$f_2^{(i)} = \frac{9}{10}\frac{\xi^4(\xi^2 + 3\xi + 1)}{(\xi^2 + \xi + 1)^3} \tag{4.22}$$

$$g_1^{(i)} = \frac{3}{2}\frac{(2\xi + 1)}{(\xi^2 + \xi + 1)^2} \tag{4.23}$$

$$g_2^{(i)} = \frac{3}{2}\frac{\xi^3(\xi + 2)}{(\xi^2 + \xi + 1)^2}. \tag{4.24}$$

The equations of motion (4.19) must be coupled to a set of additional equations: the balance equation of energy and the balance equation of isotopes abundance.

The balance equation of energy is essentially the first law of thermodynamics

$$\frac{\mathrm{d}U}{\mathrm{d}t} = -p\frac{\mathrm{d}V}{\mathrm{d}t} + \dot{Q}, \tag{4.25}$$

and with the help of the fundamental equation of the matter

$$U = u(\rho, T, \boldsymbol{X})m, \tag{4.26}$$

can be rewritten as

$$C_v \frac{\mathrm{d}T}{\mathrm{d}t} = -\left(\frac{\partial U}{\partial \rho}\right)_T \frac{\mathrm{d}\rho}{\mathrm{d}t} - p\frac{\mathrm{d}V}{\mathrm{d}t} + \dot{Q}, \tag{4.27}$$

where $C_v = c_v m$ is the heat capacity at constant volume and the heat source term $\dot{Q}$ is

$$\dot{Q} = -q\frac{\mathrm{d}V}{\mathrm{d}t} + m\epsilon - L, \tag{4.28}$$

with q being the artificial viscosity term, ϵ the energy generation rate of thermonuclear reactions per gram of combustible, and L the luminosity for radiative and conductive heat transfer.

The balance equation of abundance, without diffusion of the elements, can be expressed as

$$\frac{\mathrm{d}X_a}{\mathrm{d}t} = \sum_b \Lambda_{ab}, \tag{4.29}$$

where $\boldsymbol{\Lambda} = \boldsymbol{\Lambda}(\rho, T, \boldsymbol{X})$ is the reaction rate an $\boldsymbol{X}$ is the abundance which represents the mass fraction of the isotope.

Once specified the equation of state, the nuclear energy generation rate, the artificial viscosity and the luminosity, the above system of equations (4.19), (4.27) and (4.29) can be solved numerically for the set of variables $\{R_i, T_i, \boldsymbol{X}_i\}$ with $i = 1, \ldots, N$.

It is important to note that in our formalism the total energy

$$E = K + \Omega + U \tag{4.30}$$

is strictly conserved when there is no nuclear reactions and luminosity present, independently of the number of shells N. In fact

$$\frac{\mathrm{d}E}{\mathrm{d}t} = \sum_{i=1}^{N}(m_i\epsilon_i - L_i). \tag{4.31}$$

This is a basic advantage of the Effective Lagrangian Method: it permits us to keep absolute control of the energy content even for a small value of N. Another advantage is that, in the large N limit for spherically symmetric systems, the Effective Lagrangian Method is equivalent to the Reactive Euler Equations adding the artificial viscosity term.

4.2 Artificial Viscosity

To prevents non-physical high-frequency oscillatory modes during a shock regime, von Neumann and Richtmyer [137] introduced the artificial viscosity expressed as

$$q = \begin{cases} (q_0 \Delta R)^2 \rho (\dot{\rho}/\rho)^2, & \dot{\rho} > 0 \\ 0, & \dot{\rho} < 0 \end{cases}. \tag{4.32}$$

where ΔR is the radial length of the shell and q_0 is a dimensionless parameter between 0 and 1.0.

The original prescription of von Neumann and Richtmyer was found to work fine in Cartesian coordinates, but in a spherical collapse where the infall velocity $v_r \propto r$, it presents a problem, producing significant artificial viscosity where there is no shock. The problem was solved (e.g. [138]) by defining the artificial viscosity as

$$q = -q_0^2 \rho (\Delta r)^2 |\nabla \cdot \boldsymbol{v}| \left(\frac{\partial v_r}{\partial r} - \frac{1}{3} \nabla \cdot \boldsymbol{v} \right) \tag{4.33}$$

and in the free-fall collapse $q = 0$ (Section 4.7.1).

4.3 Equation of state

Our equation of state has the input variables as mass density ρ and temperature T of the material and the output variables are the pressure and internal energy per unit mass as a sum over species

$$p(\rho, T, \boldsymbol{X}) = p_{\text{rad}} + p_{\text{ion}} + p_{\text{ele}} + p_{\text{pos}}, \tag{4.34}$$

$$u(\rho, T, \boldsymbol{X}) = u_{\text{rad}} + u_{\text{ion}} + u_{\text{ele}} + u_{\text{pos}}, \tag{4.35}$$

where the subscripts *rad*, *ion*, *ele* and *pos* represent the contributions due to radiation, ions, electrons and positrons, respectively.

Moreover, quantities as heat specific c_V and c_p, adiabatic index γ and speed of sound c_s can be determined from known partial derivatives of the pressure and the specific internal energy with respect to the density and temperature. For this reason, our routine returns the partial derivatives

$$\left.\frac{\partial p}{\partial \rho}\right|_T, \quad \left.\frac{\partial p}{\partial T}\right|_\rho, \quad \left.\frac{\partial u}{\partial \rho}\right|_T, \quad \left.\frac{\partial u}{\partial T}\right|_\rho, \tag{4.36}$$

and the accuracy and thermodynamic consistency of the appropriated Maxwell relations are verified following the study by Timmes & Arnett [139].

Since the calculation of the Fermi-integrals needed to determine the electron contribution and the electron-positron pair creation is numerically too expensive to be carried out during the simulation, these contributions are read off a recalculated table via bilinear interpolation. The table entries were located on a regular grid in the $(\log T, \log(\rho/\mu_e))$-plane and spanned ranges of $\log T$ = [4; 11] and $\log(\rho/\mu_e)$ = [-6; 11] in cgs units. This procedure is equivalent to the *Helmholtz* equation of state presented by Timmes *et al.* in [140]. We present the relevant calculations and algorithms in Appendix A.

4.4 Luminosity and Opacities

To simulate the thermal evolution inside the star, we use the following expression for the total luminosity of a spherically symmetric shell,

$$L_i = 4\pi R_{i-1}^2 \frac{4ac}{3} \frac{T_{i-1}^3}{\kappa_{i-1}\rho_{i-1}} \left(\frac{T_i - T_{i-1}}{R_i - R_{i-1}} \right) - 4\pi R_i^2 \frac{4ac}{3} \frac{T_i^3}{\kappa_i \rho_i} \left(\frac{T_{i+1} - T_i}{R_{i+1} - R_i} \right) \tag{4.37}$$

where the first parcel is the luminosity coming from the inner shell and the second one is the luminosity leaving the shell. This prescription is the integral version of the (2.31) and it is sufficient to keep the conservation of energy inside the star. In fact, the total luminosity becomes

$$L_{\text{total}} = \sum_{i=1}^{N} L_i = L_N, \tag{4.38}$$

which is the luminosity of the outermost shell.

As discussed in Section 3.2, the total opacity κ in (4.37) can be written as

$$\kappa(\rho, T, \boldsymbol{X}) = \left(\kappa_{\text{rad}}^{-1} + \kappa_{\text{cond}}^{-1} \right)^{-1} \tag{4.39}$$

with the radiative opacity equals

$$\kappa_{\text{rad}} = 10^{23} \rho T^{-3.5} + 0.2 \text{ cm}^2 \text{ g}^{-1}, \tag{4.40}$$

and the conductive opacity is constructed from the *condall06.d*[1] table of electron thermal conductivity by Cassisi *et al.* [108]. This conductivity table covers a large region of the $\log\rho$ = [-6; 9] and $\log T$ = [3; 9] plane, and ion charge numbers Z from 1 to 60. Moreover, for the outer-table regions we use analytical fits to the electron thermal conductivity. We use the Iben [141] fit to the Hubbard-Lampe [106] electron

[1] http://www.ioffe.ru/astro/conduct/condint.html

conduction opacity for the non-degenerate phase, and the Cassisi's procedure established for the electron-electron contributions with the fitting formula from Potekhin *et al.* [116] for the electron-ion contributions in the degenerate case. The transition between non-degenerate and degenerate cases for the outer-table region is simplified as

$$\log T_{\rm deg} = 0.36 \log\left(\rho/\mu_e\right) + 7.34 \tag{4.41}$$

where the region with temperatures below the degenerate temperature $T_{\rm deg}$ is strongly degenerate and above the electrons are non-degenerate.

4.5 Thermonuclear reactions

The thermonuclear reactions must be treated with several isotopes in a nuclear reaction network. Since nuclear networks with hundreds of isotopes are very expensive in terms of CPU time and memory, we use a simplified nuclear network in our hydrodynamical calculations.

The *iso7* network, presented by Timmes *et al.* in [142], provides the nuclear energy generation rate and abundance levels of an α-chain nuclear network that contains only seven isotopes. From ^{4}He to ^{24}Mg the *iso7* reaction network is equivalent to the standard α-chain reaction network, but the difference starts at ^{28}Si. There is no flow from ^{28}Si to ^{32}S, instead, ^{28}Si moves directly to ^{56}Ni with the addiction of 7 ^{4}He nuclei, skipping the intermediate isotopes present in an α-chain reaction network. These direct transitions between [^{28}Si] and [^{56}Ni] are the key steps in reducing the network size to seven isotopes.

The set of 7 nuclei used is

$$\boldsymbol{X}^T = (^4\mathrm{He}, ^{12}\mathrm{C}, ^{16}\mathrm{O}, ^{20}\mathrm{Ne}, ^{24}\mathrm{Mg}, [^{28}\mathrm{Si}], [^{56}\mathrm{Ni}]) \tag{4.42}$$

where [^{28}Si] mass fraction is a silicon group (intermediate mass elements - IME) abundance and the [^{56}Ni] mass fraction is an nickel-iron group abundance. And explicitly, the reaction network is the following:

$$\begin{aligned}
\frac{\mathrm{d}(^4\mathrm{He})}{\mathrm{d}t} =& -3\lambda_{3\alpha}(^4\mathrm{He})^3 + 3\lambda_{\mathrm{C}(\gamma,3\alpha)}(^{12}\mathrm{C}) - \lambda_{\mathrm{C}(\alpha,\gamma)}(^4\mathrm{He})(^{12}\mathrm{C}) \\
&+ \lambda_{\mathrm{C(C},\gamma)}(^{12}\mathrm{C})^2 + 0.5\lambda_{\mathrm{C(O},\alpha+\gamma)}(^{12}\mathrm{C})(^{16}\mathrm{O}) + \lambda_{\mathrm{O}(\gamma,\alpha)}(^{16}\mathrm{O}) \\
&- \lambda_{\mathrm{O}(\alpha,\gamma)}(^4\mathrm{He})(^{16}\mathrm{O}) + \lambda_{\mathrm{O(O},\alpha)}(^{16}\mathrm{O})^2 + \lambda_{\mathrm{Ne}(\gamma,\alpha)}(^{20}\mathrm{Ne}) \\
&- \lambda_{\mathrm{Ne}(\alpha,\gamma)}(^4\mathrm{He})(^{20}\mathrm{Ne}) + \lambda_{\mathrm{Mg}(\gamma,\alpha)}(^{24}\mathrm{Mg}) - \lambda_{\mathrm{Mg}(\alpha,\gamma)}(^4\mathrm{He})(^{24}\mathrm{Mg}) \\
&+ \lambda_{\mathrm{Si}(\gamma,\alpha)}(^{28}\mathrm{Si}) - 7.0\lambda_{\mathrm{Si}\to\mathrm{Ni}}(^4\mathrm{He}) + 7.0\lambda_{\mathrm{Ni}\to\mathrm{Si}}[^{56}\mathrm{Ni})]
\end{aligned} \tag{4.43}$$

$$\begin{aligned}\frac{\mathrm{d}(^{12}\mathrm{C})}{\mathrm{d}t} =&\lambda_{3\alpha}(^{4}\mathrm{He})^3 - \lambda_{\mathrm{C}(\alpha,\gamma)}(^{4}\mathrm{He})(^{12}\mathrm{C}) - \lambda_{\mathrm{C}(\gamma,3\alpha)}{}^{12}\mathrm{C} - 2\lambda_{\mathrm{C}(\mathrm{C},\gamma)}(^{12}\mathrm{C})^2 \\ &- \lambda_{\mathrm{C}(\mathrm{O},\alpha+\gamma)}(^{12}\mathrm{C})(^{16}\mathrm{O}) + \lambda_{\mathrm{O}(\gamma,\alpha)}(^{16}\mathrm{O})\end{aligned} \tag{4.44}$$

$$\begin{aligned}\frac{\mathrm{d}(^{16}\mathrm{O})}{\mathrm{d}t} =&\lambda_{\mathrm{C}(\alpha,\gamma)}(^{4}\mathrm{He})(^{12}\mathrm{C}) - \lambda_{\mathrm{C}(\mathrm{O},\alpha+\gamma)}(^{12}\mathrm{C})(^{16}\mathrm{O}) - \lambda_{\mathrm{O}(\gamma,\alpha)}(^{16}\mathrm{O}) \\ &- \lambda_{\mathrm{O}(\alpha,\gamma)}(^{16}\mathrm{O})(^{4}\mathrm{He}) - 2\lambda_{\mathrm{O}(\mathrm{O},\alpha)}(^{16}\mathrm{O})^2 + \lambda_{\mathrm{Ne}(\gamma,\alpha)}(^{20}\mathrm{Ne})\end{aligned} \tag{4.45}$$

$$\begin{aligned}\frac{\mathrm{d}(^{20}\mathrm{Ne})}{\mathrm{d}t} =&\lambda_{\mathrm{C}(\mathrm{C},\gamma)}(^{12}\mathrm{C})^2 + \lambda_{\mathrm{O}(\alpha,\gamma)}(^{16}\mathrm{O})(^{4}\mathrm{He}) - \lambda_{\mathrm{Ne}(\gamma,\alpha)}(^{20}\mathrm{Ne}) \\ &- \lambda_{\mathrm{Ne}(\alpha,\gamma)}(^{20}\mathrm{Ne})(^{4}\mathrm{He}) + \lambda_{\mathrm{Mg}(\gamma,\alpha)}(^{24}\mathrm{Mg})\end{aligned} \tag{4.46}$$

$$\begin{aligned}\frac{\mathrm{d}(^{24}\mathrm{Mg})}{\mathrm{d}t} =&0.5\lambda_{\mathrm{C}(\mathrm{O},\alpha+\gamma)}(^{12}\mathrm{C})(^{16}\mathrm{O}) + \lambda_{\mathrm{Ne}(\alpha,\gamma)}(^{20}\mathrm{Ne})(^{4}\mathrm{He}) - \lambda_{\mathrm{Mg}(\gamma,\alpha)}(^{24}\mathrm{Mg}) \\ &- \lambda_{\mathrm{Mg}(\alpha,\gamma)}(^{24}\mathrm{Mg})(^{4}\mathrm{He}) + \lambda_{\mathrm{Si}(\gamma,\alpha)}(^{28}\mathrm{Si})(^{4}\mathrm{He})\end{aligned} \tag{4.47}$$

$$\begin{aligned}\frac{\mathrm{d}[^{28}\mathrm{Si}]}{\mathrm{d}t} =&0.5\lambda_{\mathrm{C}(\mathrm{O},\alpha+\gamma)}(^{12}\mathrm{C})(^{16}\mathrm{O}) + \lambda_{\mathrm{O}(\mathrm{O},\alpha)}(^{16}\mathrm{O})^2 - \lambda_{\mathrm{Mg}(\alpha,\gamma)}(^{24}\mathrm{Mg})(^{4}\mathrm{He}) \\ &- \lambda_{\mathrm{Si}(\gamma,\alpha)}(^{28}\mathrm{Si}) - \lambda_{\mathrm{Si}\to\mathrm{Ni}}(^{4}\mathrm{He}) + \lambda_{\mathrm{Ni}\to\mathrm{Si}}[^{56}\mathrm{Ni}]\end{aligned} \tag{4.48}$$

$$\frac{\mathrm{d}[^{56}\mathrm{Ni}]}{\mathrm{d}t} = \lambda_{\mathrm{Si}\to\mathrm{Ni}}(^{4}\mathrm{He}) - \lambda_{\mathrm{Ni}\to\mathrm{Si}}[^{56}\mathrm{Ni}] \tag{4.49}$$

The $\lambda_{\mathrm{C}(\mathrm{O},\alpha+\gamma)} = \lambda_{\mathrm{C}(\mathrm{O},\alpha)\mathrm{Mg}} + \lambda_{\mathrm{C}(\mathrm{O},\gamma)\mathrm{Si}}$ represents the total carbon-oxygen fusion reaction rate with the same branching ratio for magnesium and silicon production. Indeed, the $\lambda_{\mathrm{Si}\to\mathrm{Ni}}$ and $\lambda_{\mathrm{Ni}\to\mathrm{Si}}$ are the direct and reverse reaction rate from intermadiate-mass elements $[^{28}\mathrm{Si}]$ to nickel-group elements $[^{56}\mathrm{Ni}]$, respectively.

Once the nuclear reaction network has been constructed, the average energy generated per unit mass over a time interval Δt in (4.28) is

$$\epsilon_{\mathrm{nuc}}(\rho, T, \boldsymbol{X}) = N_A \sum_k \frac{B_k}{A_k}\frac{\Delta X_k}{\Delta t}. \tag{4.50}$$

where B_k is the binding energy of the isotope k. This average energy generation rate is used when the hydrodynamic evolution is slower than the nuclear evolution and it was used in this work.

The point is that this *iso7* network gives the thermonuclear energy generation rate and nucleosynthesis generally close of that given by much larger nuclear reaction networks.

4.6 Integration and Timestepping

4.6.1 The Runge-Kutta-Fehlberg Integrator

Runge-Kutta methods for integrating systems of differential equations are well known, tried and trusted methods, which use multiple estimates of the derivative across a given time-step to arrive at accurate, generally high order estimates for the evolved quantities. Most common is the fourth order Runge-Kutta method, often simply abbreviated to RK4, which has been known and used for over a century [143].

The embedded methods are designed to produce an estimate of the local truncation error of a single Runge-Kutta step, and as result, allow to control the error with adaptive step-size. The embedded method I have used is the Fehlberg method [144], which consists of two methods in the tableau, one with order 1 and one with order 2, denominated Fehlberg RKF1(2) method.

For a given variable $\boldsymbol{y}$, the evolution from $\boldsymbol{y}_n$ at time t_n to $\boldsymbol{y}_{n+1}$ at time $t_{n+1} = t_n + \Delta t$ is given by

$$\frac{d\boldsymbol{y}}{dt} = \boldsymbol{f}(t, \boldsymbol{y}), \tag{4.51}$$

with the lower-order step given by

$$\boldsymbol{y}_{n+1} = \boldsymbol{y}_n + \frac{\Delta t}{256}\left(\boldsymbol{k}_1 + 255\boldsymbol{k}_2\right), \tag{4.52}$$

and the high-order step given by

$$\boldsymbol{y}^*_{n+1} = \boldsymbol{y}_n + \frac{\Delta t}{512}\left(\boldsymbol{k}_1 + 510\boldsymbol{k}_2 + \boldsymbol{k}_3\right) \tag{4.53}$$

with the RKF1(2) steps written explicitly as

$$\boldsymbol{k}_1 = \boldsymbol{f}\left(t_n, \boldsymbol{y}_n\right) \tag{4.54}$$

$$\boldsymbol{k}_2 = \boldsymbol{f}\left(t_n + \frac{\Delta t}{2}, \boldsymbol{y}_n + \frac{\Delta t}{2}\boldsymbol{k}_1\right) \tag{4.55}$$

$$\boldsymbol{k}_3 = \boldsymbol{f}\left(t_n + \Delta t, \boldsymbol{y}_n + \frac{\Delta t}{256}(\boldsymbol{k}_1 + 255\boldsymbol{k}_2)\right). \tag{4.56}$$

The truncated error estimate can be determined from

$$\varepsilon_{n+1} = |\boldsymbol{y}_{n+1} - \boldsymbol{y}^*_{n+1}| = \frac{\Delta t}{512}|\boldsymbol{k}_1 - \boldsymbol{k}_3| \tag{4.57}$$

4.6.2 Timestepping Criteria

For any integrator, it is crucial that the time-step be chosen correctly, both to ensure the accuracy of the evolution and to ensure numerical stability. In this section I shall briefly discuss the principal timestepping criteria in general use, and one specific to the code I have used.

Integrator Criterion

The RKF1(2) method has a time-step criterion associated with the error correction. The calculated step can either be accepted ($\varepsilon < \texttt{tol}$) or rejected ($\varepsilon > \texttt{tol}$) and re-calculated. In both cases one can use the error measure to estimate the new time step. Since $\varepsilon \propto \Delta t$, the new time step is

$$\Delta t_{\text{new}} = s\left(\frac{\texttt{tol}}{\varepsilon}\right)\Delta t \tag{4.58}$$

where $s < 1$ is a "safety factor" for a conservative choice of the next time step.

Courant-Friedrichs-Lewy Criterion

By far the most general time-step criterion for gas-dynamical systems is the so-called *Courant-Friedrichs-Lewy* or CFL criterion, given in it simplest form by

$$\Delta t_{CFL} \leq \frac{l}{v} \tag{4.59}$$

where l is a characteristic length scale, and v is a characteristic speed [145]. For one-dimensional simulations, these are both well defined; the fluid element length Δx provides the characteristic length, and sound speed c_s gives the characteristic speed.

The CFL condition for our spherical shells description then becomes

$$\Delta t_{CFL} = \frac{\Delta R}{c_s} \tag{4.60}$$

The physical interpretation of this time interval is that it prevents spatial information transfer through the fluid at a rate greater than the local sound speed.

Force Criterion

A further commonly used time-step condition is that based on the acceleration of the fluid element, know as the acceleration condition. This is simple in form, and is given by

$$\Delta t_F = \sqrt{\frac{\Delta R}{|\boldsymbol{a}|}} \tag{4.61}$$

where $\boldsymbol{a}$ is the fluid element acceleration.

Conservative Criterion

A general class of additional time-step criteria can be obtained by dimensional analysis, in that for any time-varying quantity y we may define a characteristic timescale on which it varies as

$$\Delta t_y = \frac{y}{\dot{y}} \tag{4.62}$$

where as usual $\dot{y}$ is the time derivative of y.

Although not required in general, a time-step criterion of this form was implemented into the code when looking at the effects of strongly varying cooling times and to tracking the variation of energy during explosive dynamics.

Setting the Time-step

There are therefore a variety of possible time-step choices, and thus to ensure that they are all satisfied, the time-step for each fluid element used is the minimum of all possibilities, i.e.

$$\Delta t_i = \min\left(\Delta t_{\rm new}, \Delta t_{CFL}, \Delta t_F, \Delta t_y\right), \tag{4.63}$$

which are the characteristic timescale for each fluid element. A good choice is to use a global time-step $\Delta t_{\rm glob}$, which is set by the minimum of the time-steps Δt_i for the individual fluid element, such that

$$\Delta t_{\rm glob} = \beta \min \Delta t_i, \tag{4.64}$$

and $\beta < 1$ is a tuning factor. Values for β vary from problem to problem but are generally in the range 0.25 - 0.5, and here we set $\beta = 0.3$.

This approach has the advantage that all fluid elements are evolved in a single lockstep, and thus there is no lag due to evolve each element on separate time-steps.

4.7 Code Validation and Verification

At this point our software needs to be validated and verified. In this process of checking, our software should fulfills its purposes to simulate a spherically symmetric star and all processes associated with supernova explosions. In this section we list some appropriate tests for this check.

4.7.1 Free fall collapse

Here we execute and present the simulation of the free-fall collapse of a homogeneous sphere. The problem has an analytical solution [146] that can be obtained inserting the definition of velocity in the momentum conservation equation (with no-pressure $p = 0$), while assuming that the homogeneous sphere is initially at rest ($v_r = 0$ cm/s, at $t = t_0$). The corresponding solution can be written as

$$\left(\frac{8\pi G\rho_0}{3}\right)^{1/2}(t - t_0) = \left(1 - \frac{R}{R_0}\right)^{1/2}\left(\frac{R}{R_0}\right)^{1/2} + \arcsin\left(1 - \frac{R}{R_0}\right)^{1/2}, \qquad (4.65)$$

where ρ_0 and R_0 are the initial density and radius of the sphere, and G is the gravitational constant.

We perform a calculation using $N = 100$ shells, without pressure and artificial viscosity, and our result are in excellent agreement with the analytical solution of the free-fall problem, as presented in Figure 4.2a.

In about 0.65 s, the density of the sphere has increased by six orders of magnitude (Figure 4.2b) but, as theoretically predicted, homogeneity is maintained throughout the sphere. This defines a homologous collapse, with a constant temperature and a uniform density across the sphere. Note also that since $\rho \propto R^{-3}$, a plot of the density versus radius has a constant slope, as showed in Figure 4.2c.

4.7.2 Sod's Shock Wave Problem

As an example of a test involving shocks we consider the classical test of the spherical explosion in ideal hydrodynamics, an extension of the classical Sod shock tube test [147] to the case of spherical geometry. The present problem consists of a spherical system of 1 earth radius. The interface is located at

At the initial time, the states on the left and on the right sides of the interface are constant. The left state is a high density fluid characterized by $\rho = 10^7$ g cm^{-3} and $\dot{R} = 0$, the right state is a low density fluid defined by $\rho = 1.25 \times 10^6$ g cm^{-3} and $\dot{R} = 0$. The equation of state is the complete eos presented in Section 4.3.

The Figure 4.3 represent the profiles of density, pressure and velocity at instants of time t = 0, 0.125, and 0.25 s. There is no current analytical solution to this prob-

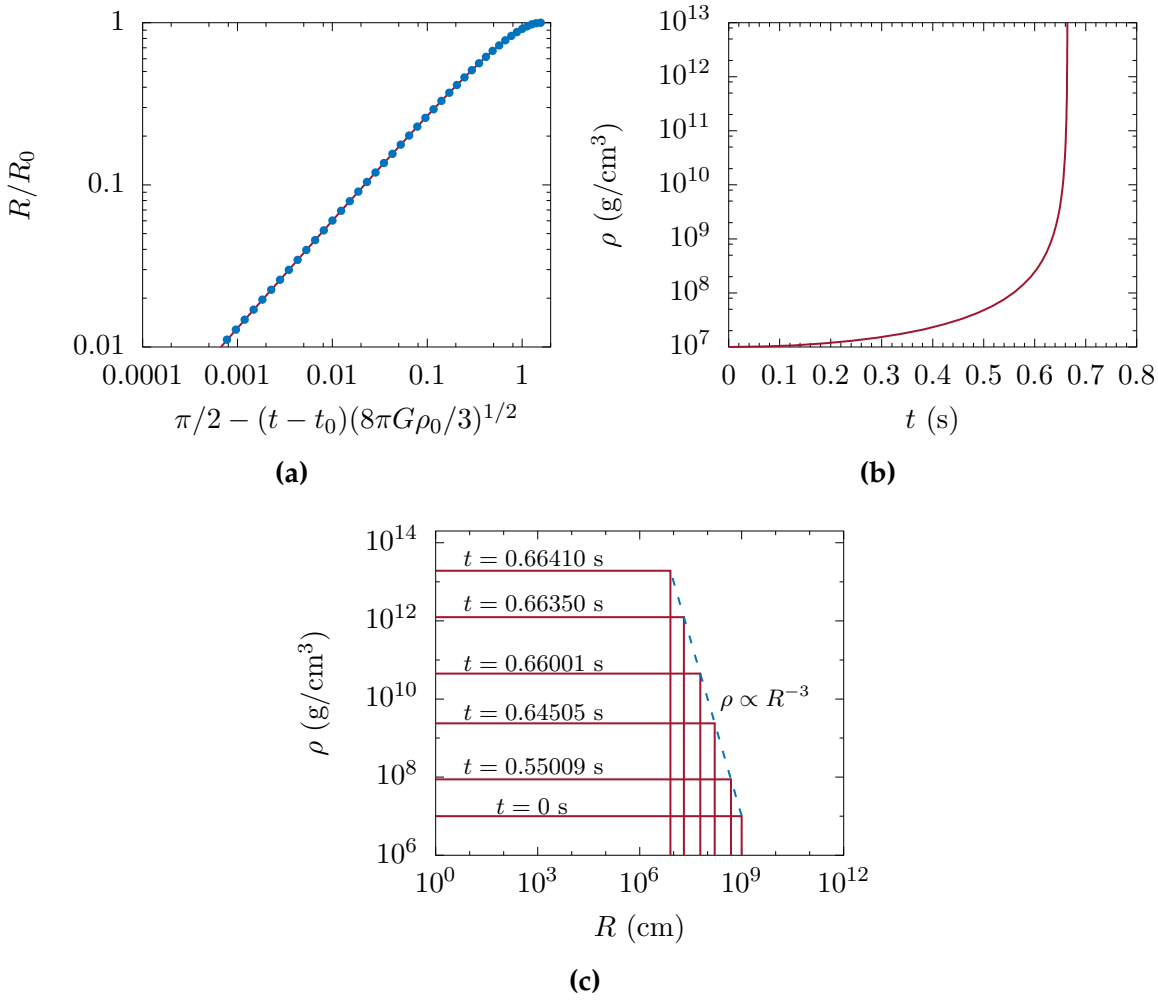

Figure 4.2: (a) Simulation of the free-fall collapse of a homogeneous sphere. Note the agreement between the analytical solution (*red line*) and the numerical results (*blue points*). Simulation performed with the *ELcode*, with $N = 100$ shells. **(b)** Evolution of the central density as a function of time for the free-fall collapse. **(c)** Density profile versus radius for the free-fall collapse. The blue dashed line represents the relation $\rho \propto R^{-3}$ to the outer shell.

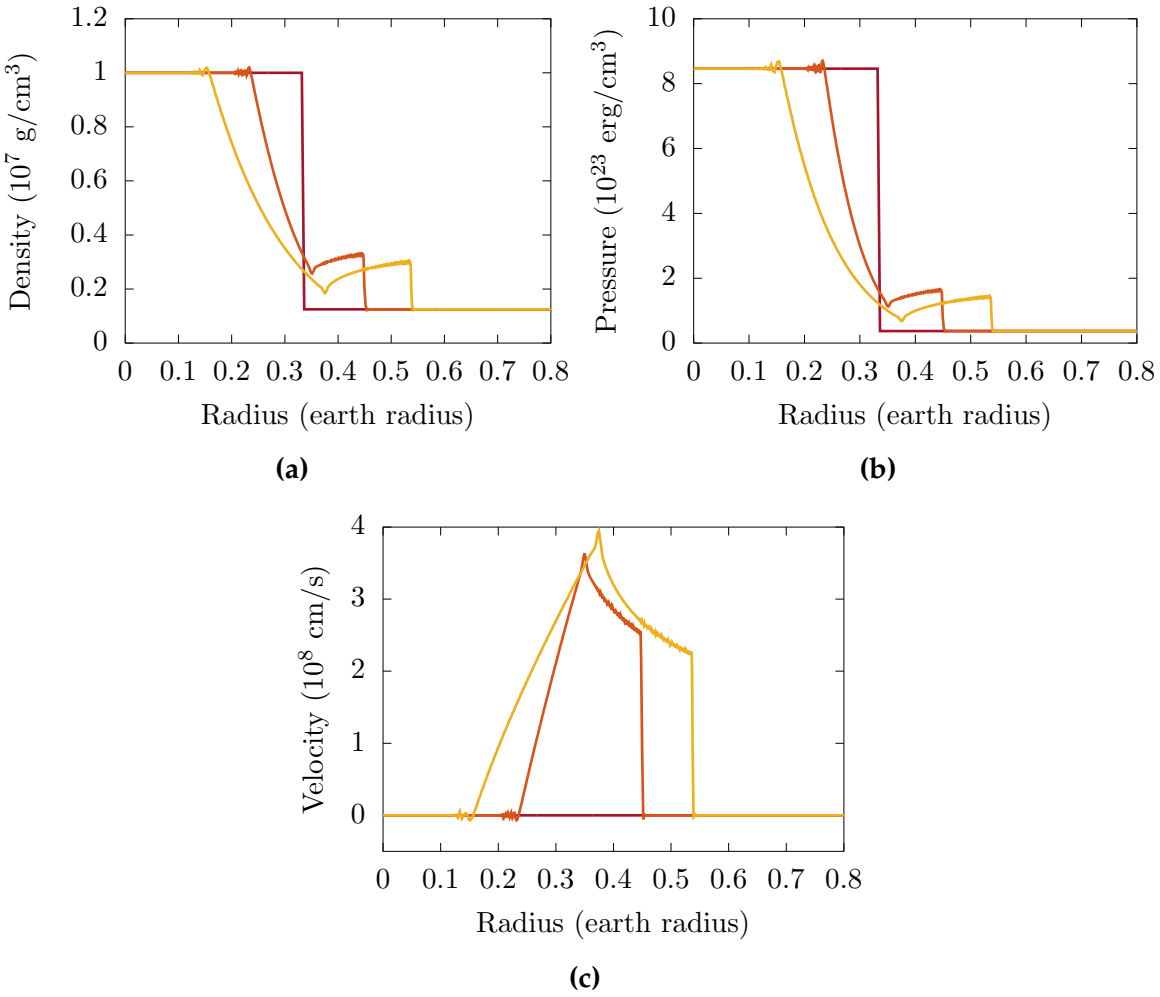

Figure 4.3: **(a)** Density profiles at times t = 0, 0.125, and 0.25 s, in Sod's shock wave problem, using *ELcode* with 1000 shells. **(b)** Pressure profiles. **(c)** Velocity profiles.

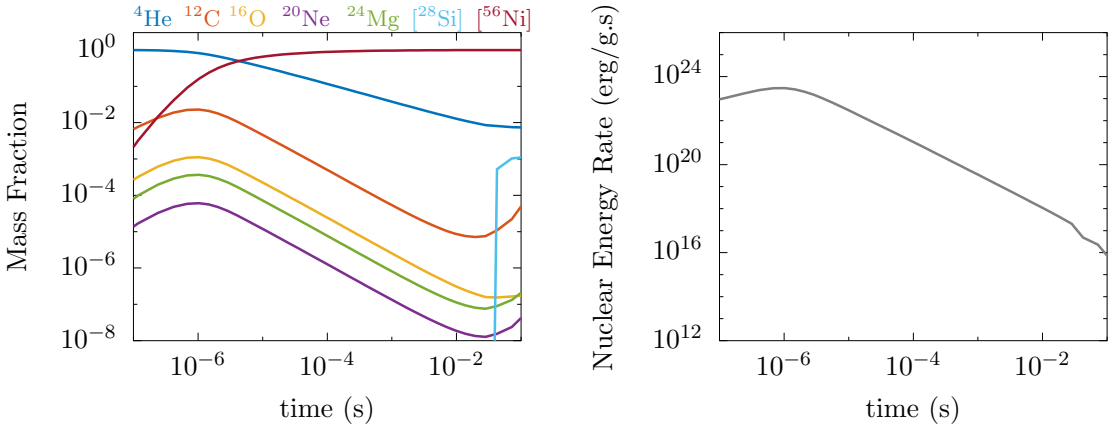

Figure 4.4: **(a)** Evolution of the mass fractions under adiabatic expansion using the *iso7* reaction network. The initial conditions are $T = 3 \times 10^9$ K and $\rho = 1 \times 10^8$ g cm^{-3} with a pure ^{4}He composition. The sum of the intermediate-mass fractions are plotted as silicon-group [^{28}Si], and the sum of the nickel-mass fractions are plotted as nickel-group [^{56}Ni]. **(b)** The energy generation rate under adiabatic expansion. Helium burning under these conditions is exothermic.

lem to compare. The main purpose is to keep the small fluctuations produced by discontinuities under control with the artificial viscosity.

4.7.3 Explosive Nuclear Burning

An explosive burning is characterized by a material heated and compressed by a shock wave to some temperature $T_{\rm sh}$ and $\rho_{\rm sh}$ which subsequently expands adiabatically as a pure radiation gas [e.g., 148]. The temperature and density decreases over a hydrodynamic timescale, the free-fall timescale $\tau_{\rm hyd} = (24\pi G\rho)^{-1/2}$, in the form

$$T(t) = T_{\rm sh} \exp\left(-t/3\tau_{\rm hyd}\right), \tag{4.66}$$

$$\rho(t) = \rho_{\rm sh} \exp\left(-t/\tau_{\rm hyd}\right). \tag{4.67}$$

The Figure 4.4, Figure 4.5 and Figure 4.6b represent the explosive burning for pure-helium, half-carbon-half-oxygen composition, and pure-silicon composition, respectively. The precursor shock wave temperature and densities are listed in each figure. Our results are compared to the original paper from Timmes *et al.* [142] and are in good agreement with their calculations.

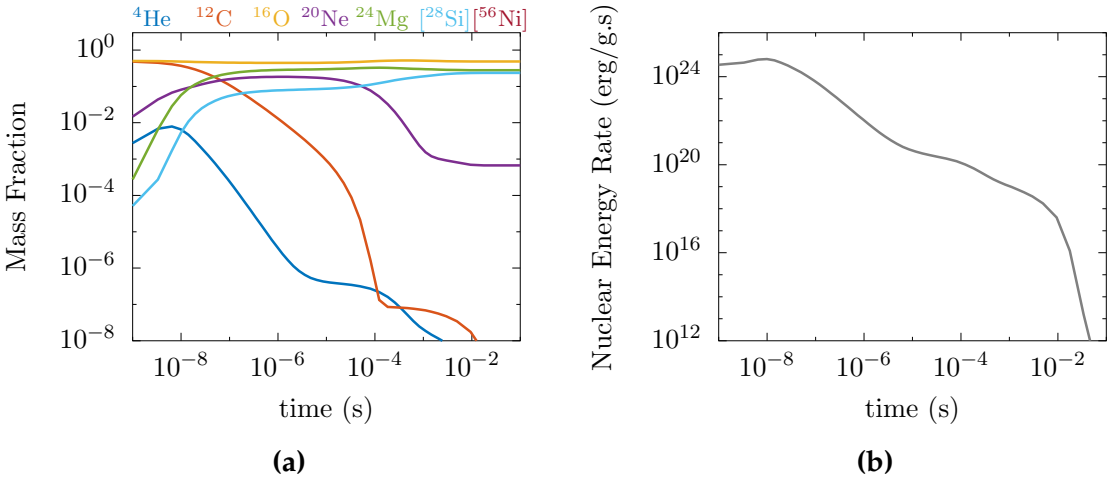

Figure 4.5: **(a)** Evolution of the mass fractions under adiabatic expansion using the *iso7* reaction network. The initial conditions are $T = 3 \times 10^9$ K and $\rho = 1 \times 10^9$ g cm^{-3} with a mixture half ^{12}C-half ^{16}O composition. **(b)** The energy generation rate under adiabatic expansion. Carbon-oxygen burning under these conditions is exothermic.

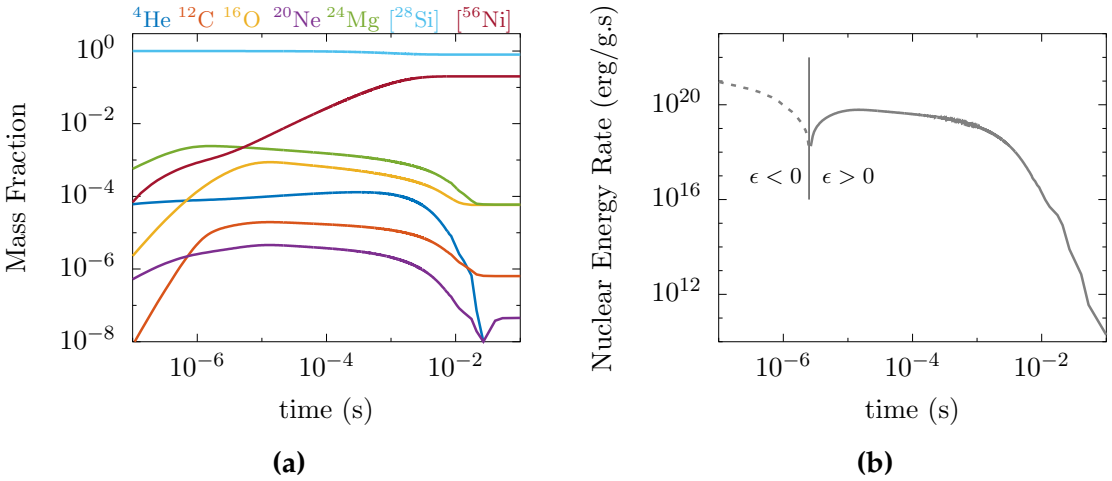

Figure 4.6: **(a)** Evolution of the mass fractions under adiabatic expansion using the *iso7* reaction network. The initial conditions are $T = 5 \times 10^9$ K and $\rho = 1 \times 10^9$ g cm^{-3} with a pure ^{28}Si composition. **(b)** The energy generation rate under adiabatic expansion. Silicon burning under these conditions is endothermic before $t \sim 10^{-5}$ s and exothermic afterward. The transition point is marked with the black vertical line.

Chapter 5

Stationary Cooling of White Dwarfs

We learn about the stars by receiving and interpreting the messages which their light brings to us. The message of the Companion of Sirius when it was decoded ran: "I am composed of material 3,000 times denser than anything you have ever come across; a ton of my material would be a little nugget that you could put in a matchbox." What reply can one make to such a message? The reply which most of us made in 1914 was—"Shut up. Don't talk nonsense.

– A. S. Eddington (1882-1944)

The observed white dwarfs have considerable high effective temperatures ($T_{\rm eff}$) ranging from 5,000 K to over 100,000 K, losing their thermal energy emitting radiation [e.g., 17]. Their outer layers determine the thermal evolution of the whole white dwarfs although the amount of mass contained there is small, while the bulk degenerate electrons keep the star's core essentially isothermal due to its high thermal conductivity and hotter than the crust. The radiative opacity in these outermost layers prevents the white dwarf to cool quickly. Comparison between observations and models requires the corrections from the finite temperature effects to the white dwarf stellar structure, despite the zero temperature approximation of highly degenerate electron gas pressure provides an adequate description of the stellar structure as a whole. Many works have been developed, since the discovery of the maximum mass of ideal white dwarfs (WD) by [8], in the field of finite temperature corrections to the degenerate equation of state (EoS) [e.g., 11, 12, 13]. However, as commented by Boshkayev *et al*. [149], a systematic analysis using empirical mass-radius relations obtained from the spectroscopic or photometric measurements of

masses and radii is still needed to understand the precise structure and the dynamics of time evolution of WDs.

Moreover, the total number of observed hot ($T_{\rm eff} > 10\ 000$ K) white dwarfs (WDs) has increased enormously mainly due to the Sloan Digital Sky Survey (SDSS; [150]). Follow-up high quality ground-based spectroscopy of survey objects yield large samples of hot WDs with precise measurements of effective temperatures and surface gravities. More than 10,000 spectroscopically identified white dwarfs with determined effective temperatures ($T_{\rm eff}$) and surface gravities ($\log g$) have been detected to date [21, 10], giving us the opportunity to explore the white dwarf mass distribution, which ultimately provides insights into mass-loss processes during stellar evolution and the mass budget of the Galaxy.

5.1 Extended Model for Outer Radiative Layers of White Dwarfs

The highly degenerated electron gas inside a WD provides a high thermal conductivity as a result of the large mean free path of the degenerate electrons in the filled Fermi sea [e.g., 102]. Such high thermal conductivity together with the lack of nuclear reactions do not allow large temperature gradients, leading to an almost uniform temperature in the WD interior. On the other hand, in the domain close to its surface, the density ρ decreases and the matter becomes quickly non-degenerate. Then, the dominant heat transfer is the radiative one (and a little convection), and the heat conduction becomes much smaller if compared to the degenerate electron gas. Therefore, we expect that the structure of a WD can be modeled as an isothermal core covered by non-degenerate surface layers which isolates the degenerate core from the outer space [e.g., 3].

To exploit the above image, let us introduce a simple approach to describe the energy transfer mechanism in the outer layers of a white dwarf. The main simplification consists in attributing the outermost layers as the region responsible by the thermal regulation of the white dwarf and the core responsible for the mechanical regulation of the stellar structure, i.e., the core is in a hydrostatic equilibrium and the outer layers is in a stationary state of radiative energy transfer. The outer layer region starts where the degenerate matter becomes non-degenerate (ideal gas) matter. The thermal gradient and the hydrostatic equilibrium are maintained by

$$\frac{\mathrm{d}T}{\mathrm{d}r} = -\frac{3}{4ac}\frac{\kappa\rho}{T^3}\frac{L_r}{4\pi r^2} \tag{5.1}$$

and

$$\frac{\mathrm{d}P}{\mathrm{d}r} = -\frac{GM_r}{r^2}\rho, \tag{5.2}$$

where $M_r = \int_0^r \rho 4\pi r^2 \mathrm{d}r$ and $L_r = \int_0^r \epsilon 4\pi r^2 \mathrm{d}r$. Dividing one equation by the other, we can write

$$\frac{\mathrm{d}P}{\mathrm{d}T} = \frac{16\pi acG}{3}\frac{1}{\kappa}\left(\frac{M_r}{M}\right)\left(\frac{L}{L_r}\right)\frac{M}{L}T^3 \tag{5.3}$$

where M and L are respectively the mass and luminosity of the star. This equation can be integrated with the hypothesis that the outer layers are too thin to contribute to the mass, i.e., $M_r \approx M$ and there is no energy generation ($\epsilon = 0$) in these layers, i.e., $L_r \approx L$. By supposition, the material here is a non-degenerate and fully ionized gas, so we can use the ideal gas EoS and the Kramers opacity, $\kappa = \kappa_0 \rho T^{-3.5}$. With this we have

$$\rho^2 = \left(\frac{2}{8.5}\frac{4ac}{3}\frac{4\pi GM}{\kappa_0 L}\frac{\mu}{N_A k_B}\right)T^{6.5}, \tag{5.4}$$

integrating the Eq.(5.3) from $P = 0$ when $T = 0$. The Eq.(5.4) is a well-known result, as can be seen in Shapiro & Teukolsky's book [16].

Using the Eq.(5.4), which is valid for any r inside the outer layer, we can eliminate ρ from Eq.(5.1) and integrate this equation from an effective radius (region where the photons decouple from surface) where the temperature is the effective temperature to the external radius of the WD where the temperature is zero, we get

$$T_{\mathrm{eff}} = \left(\frac{1}{4.25}\frac{\mu}{N_A k_B}\right)\frac{GM}{R}\left(\frac{R}{R_{\mathrm{eff}}} - 1\right). \tag{5.5}$$

It is reasonable to assume that the effective radius can be related with the Chandrasekhar radius, $R_{\mathrm{eff}} = \xi R_{\mathrm{ch}}(M)$, with $\xi \sim 1$, since the effective radius should be very close to the core surface. Then

$$T_{\mathrm{eff}} = (588{,}862\ \mathrm{K})\mu\left(\frac{M}{M_\odot}\right)\left(\frac{R}{R_\oplus}\right)^{-1}\left[\left(\frac{R}{\xi R_{\mathrm{ch}}(M)}\right) - 1\right], \tag{5.6}$$

where μ and ξ are parameters to be determined. For simplicity we further use the analytical approximated expression for the radius of ideal white dwarfs $R_{\mathrm{ch}}(M)$ given by (1.14) with M_{ch} given by (1.15), and μ_e is the mean molecular weight per electron.

The Eq.(5.6) determines the effective temperatures of the white dwarf stars as a function of their masses and their radii. This relation is semi-empirical because the correction parameters μ and ξ are fitted by data, but it is physically based on the model of transport phenomena in the outer layers of the white dwarf stars.

5.1.1 Data Set and Procedure

Using the data from the Sloan Digital Sky Survey (SDSS) Data Release 7, Kleinman *et al.* [10] reported 42,154 spectroscopically confirmed white dwarf stars. From the 14,120 clean DAs classified by the spectra, we use the 2,216 stars with $S/N \geq 15$ and $T_{\rm eff} \geq 13{,}000$ K. Of the 923 stars which they classified as clean DBs, we use the 140 stars with $S/N \geq 15$ and $T_{\rm eff} \geq 16{,}000$ K.

The masses of the identified clean DA and DB stars are calculated from the effective temperature $T_{\rm eff}$ and surface gravity g values obtained by spectra. These relations are based on full evolutionary calculation of hydrogen-rich DA white dwarfs and hydrogen-deficient DB white dwarfs, as discussed in that paper. These evolutionary sequences constitute a complete and homogeneous grid of white dwarf models that captures the core features of progenitor evolution, in particular the internal chemical structures expected in the different types of white dwarf stars.

Therefore we will not consider the data uncertainties to fit the parameters μ and ξ, assuming that such cannot be divided in systematical uncertainties from the stellar evolution simulations, and observational uncertainties coming from the spectra. Of course, this procedure must be revised in the future when the systematical uncertainties were recognized.

Then, to adjust the parameters μ and ξ we choose a narrow range of masses around a mean value M with a width of $0.001 M_\odot$ sufficient to determine the parameters for a single value of mass, because white dwarf stars with same mass must evolve similarly.

5.1.2 DA white dwarfs

For the hydrogen-rich DA white dwarfs, the main behavior of the coefficients $\mu(M)$ and $\xi(M)$ can be fitted by the simplest forms

$$\mu(M) = \begin{cases} 0.48(0.02) & M/M_\odot < 0.448 \\ 4.2(0.2)\frac{M}{M_\odot} - 1.4(0.1) & 0.448 \leq M/M_\odot \leq 0.503 \\ 0.78(0.01)\frac{M}{M_\odot} + 0.32(0.01) & M/M_\odot > 0.503 \end{cases} \tag{5.7}$$

and

$$\xi(M) = 0.984(0.002) - 0.021(0.003)\frac{M}{M_\odot}, \tag{5.8}$$

according with the Figure 5.1, and the uncertainties are represented in the parentheses.

A transition from a pure hydrogen composition for a hydrogen-helium mixture in the outer layers is presented by the parameter $\mu(M)$ in the top panel of Fig.5.1.

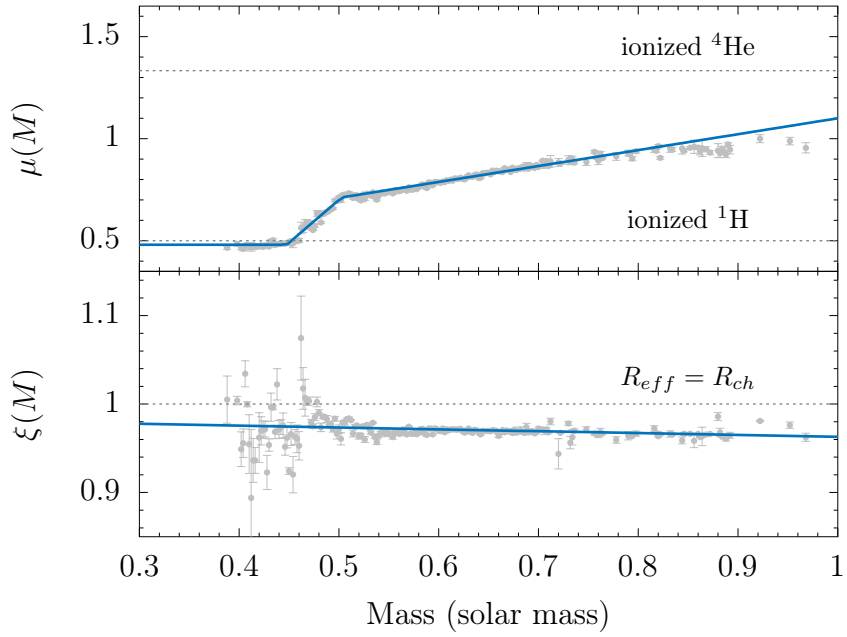

Figure 5.1: Parameters μ and ξ as a function of mass for DA-WD. The top panel shows two references for μ as dotted lines, a pure ionized He gas and a pure ionized H gas. In the bottom panel we represent the case where $R_{\text{eff}} = R_{\text{ch}}$ as dotted line.

This outer layer composition transition is marked by an core composition transition. In fact, WD with mass below 0.452 $M_\odot$ are helium-core white dwarf stars [151] and WD with mass above 0.452 $M_\odot$ are carbon-oxygen white dwarf stars [152].

The Figure 5.2 illustrates the radius-effective temperature of DA-WD with different masses using the Eq.(5.6) and the parameters $\mu(M)$ and $\xi(M)$ given by Eqs.(5.7) and (5.8) for several values of WD masses (blue lines). The orange circles represent the correspondent data for these mass values. The light gray circles are the available data for DA-WD in the SDSS-DR7. Our analytic lines are not displayed for all data but there is a excellent agreement between the semi-empirical relation and the DA-WD data for masses above 0.4 $M_\odot$. Bellow this mass value, the parameters cannot be adjusted because the low statistics of the data.

5.1.3 DB white dwarfs

For the hydrogen-deficient DB white dwarfs, the main behavior of the coefficients $\mu(M)$ and $\xi(M)$ can be fitted by the simplest forms

$$\mu(M) = 1.25(0.03) - 0.59(0.05)\frac{M}{M_\odot}, \tag{5.9}$$

$$\xi(M) = 0.92(0.03) + 0.02(0.05)\frac{M}{M_\odot}, \tag{5.10}$$

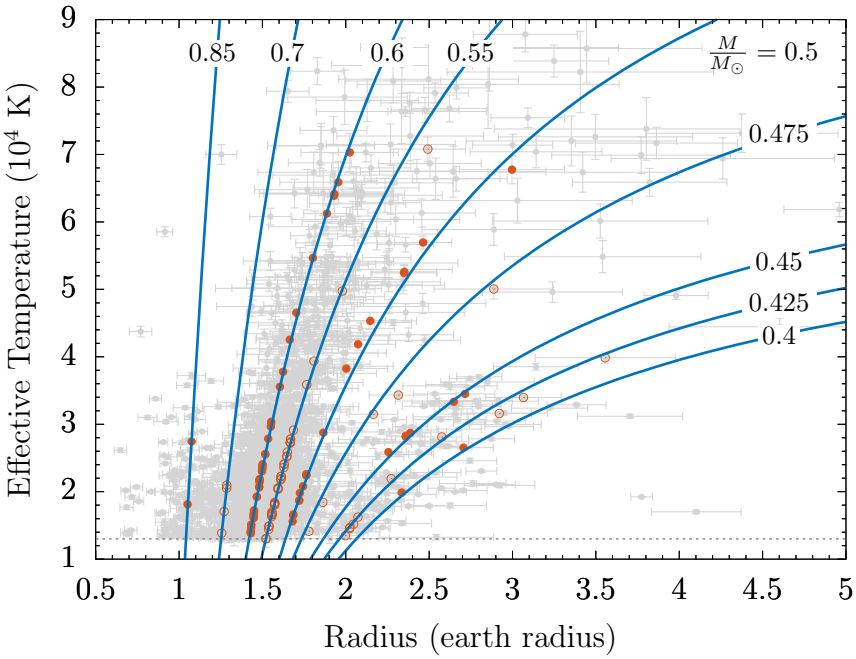

Figure 5.2: Semi-empirical radius-effective temperature relation for DA-WD with different masses. The orange circles represent some values of mass and the blue lines are their correspondent fits. The light gray circles are the available data for DA-WD from the SDSS-DR7.

according with the Figure 5.3.

For hydrogen-deficient white dwarf stars with stellar mass values from 0.515 to 0.870 $M_\odot$ [153] there is not core composition transition, and consequently the parameter $\mu(M)$ varies slowly in this range of mass values.

Alike the case of DA-WD, the Figure 5.4 illustrates the radius-effective temperature of DB-WD with different masses using the Eq.(5.6) and the parameters $\mu(M)$ and $\xi(M)$ given in this section. The red circles represent some mass values for which the semi-empirical relation is calculated, represented by the green lines. The light gray circles are the available data for DB-WD in the SDSS-DR7. There is again a good agreement between the semi-empirical relation and the DB-WD data despite the low statistics. Note that the very isolated point for $M = 0.3M_\odot$ is stay also well on our curve.

5.2 Semi-Empirical Mass-Radius Relation

The mass-radius relation is a fundamental ingredient to understand the physics of white dwarfs. The first mass-radius relation given by [154] assumed a zero temperature fully degenerate core. Finite temperature corrections to C and O nuclear material and the non-degenerate outer layers of He and H were included by Al-

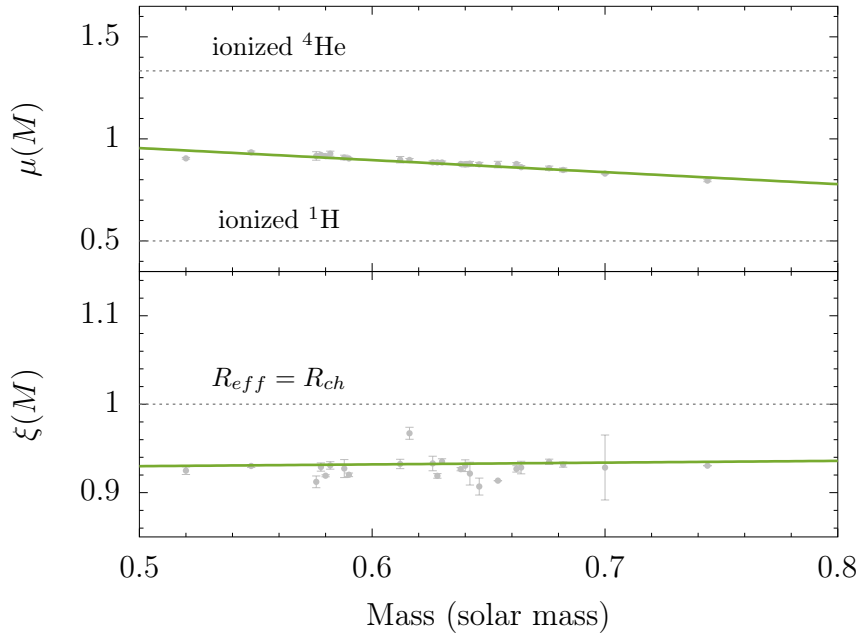

Figure 5.3: Parameters μ and ξ as a function of mass for DB-WD. The top panel shows two references for μ as dotted lines, a pure ionized He gas and a pure ionized H gas. In the bottom panel we represent the case where $R_{\text{eff}} = R_{\text{ch}}$ as dotted line.

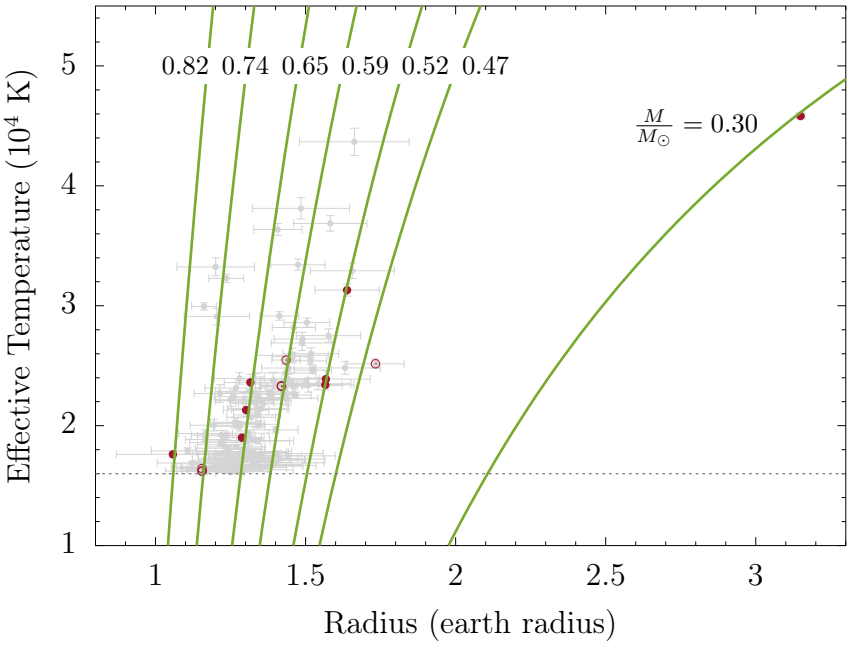

Figure 5.4: Semi-empirical radius-effective temperature relation for DB-WD with different masses. The red circles represent some values of mass and the green lines are their correspondent fits. The light gray circles are the available data for DB-WD from the SDSS-DR7.

thaus *et al.* [155]. Recently, Holberg *et al.* [156] constrain the degenerate mass-radius relation with the observations, but there is a doubt about the favored models to estimate the mass and radius of WD, using "thick" H envelopes or "thin" H envelopes. Therefore, the mass-radius relation of white dwarfs is not greatly constrained by observations.

Our constraining relation Eq.(5.6) can be inverted to give

$$R = \xi R_{\rm ch}(M)\left[1 - \frac{1}{\mu}\left(\frac{T_{\rm eff}}{T_0}\right)\left(\frac{M}{M_\odot}\right)^{-1}\left(\frac{\xi R_{\rm ch}(M)}{R_\oplus}\right)\right]^{-1}, \tag{5.11}$$

which provides a simple analytical mass-radius relation of white dwarfs, with $T_0 =$ 588,862 K. The knowledge about the parameters μ and ξ are the only physical ingredients to be added from the observations.

For DA-WD we can use the parameters μ and ξ found in Section 5.1.2. The Figure 5.5 represents this mass-radius relation of DA-WD with different effective temperatures. The data are represented in narrow ranges of effective temperature with width of 1000 K, symbolized as the orange circles. The blue lines are the correspondent mass-radius relation obtained from Eq.(5.6), where $T_4 = T/(10^4$ K). The Chandrasekhar mass-radius relation for CO ideal white dwarf is represented for comparison. We can note an ideal white dwarf behavior to white dwarf with mass above 1 $M_\odot$. This behavior comes from the denominator in Eq.(5.11) when the temperature parcel becomes smaller than the Chandrasekhar radius parcel. A mass-radius relation for DB white dwarfs can be obtained similarly, getting the parameters of Section 5.1.3, and the result is presented in Figure 5.6.

A recent paper from Tremblay *et al.* [157] reports a sample of white dwarf parallaxes, including 4 directly observed DA-WD and other wide binaries WD. This data set can be combined with spectroscopic atmospheric parameters, as effective temperature and surface gravity, to study the mass-radius relationship.

Using the data from that paper, we can reproduce the estimated masses and radii from the *Gaia*-DR1 and compare with our semi-empirical mass-radius relation, as illustrated in Figure 5.7. The purple solid circles are the directly observed DA-WD, also identified in Table 5.3, and the yellow open circles are the wide binaries DA-WD. Our semi-empirical mass-radius relation is represented as the blue lines for different effective temperatures. Since our mass-radius relation is obtained from the *SDSS*-DR7 and agreed very well with the directly observed DA-WD from *Gaia*, we suggest that the wide binaries data be reviewed in future analysis.

There is a observed sample of eclipsing white-dwarfs where the derivation of both mass and radius is independent. In Table 5.1, we calculate the radius R (the last column) for the given $T_{\rm eff}$ and $M = M_{\rm eclipse}$ which is to be compared to the

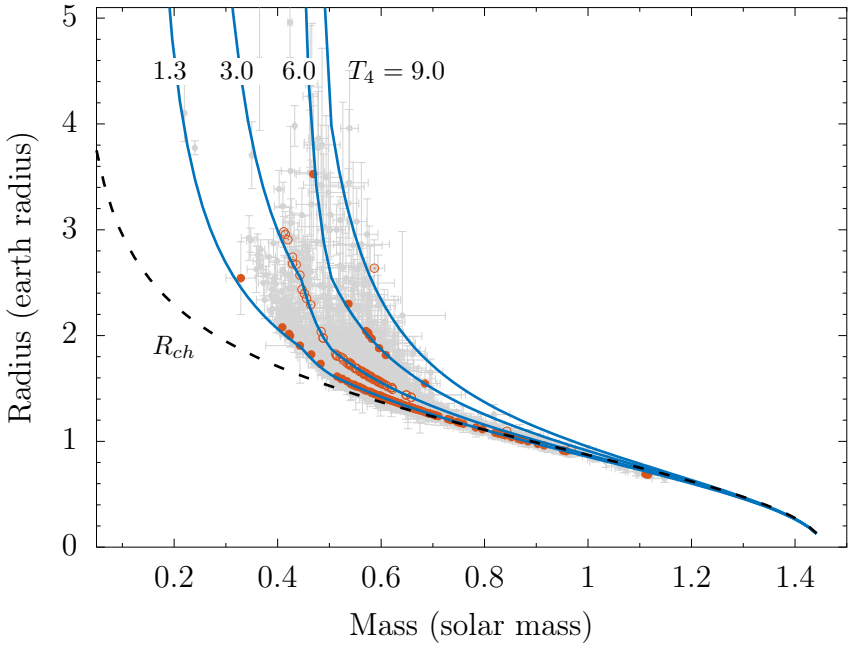

Figure 5.5: Semi-empirical mass-radius relation for DA-WD with different effective temperatures. The orange circles represent some values of effective temperature and the blue lines are their correspondent fits. The light gray circles are the available data for DA-WD from the SDSS-DR7. The dashed line corresponds to the Chandrasekhar model for ideal white dwarfs stars.

observed radius R_{eclipse} (the fourth column) . We find that our semi-empirical mass-radius relation is in good agreement with observations.

5.2.1 Effective Temperature Limit

The star radius R, from Eq.(5.11), becomes infinite when the effective temperature is equal to the limiting value, T_{lim}, given by

$$\frac{T_{\text{lim}}(M)}{T_0} = \mu \left(\frac{M}{M_\odot}\right) \left(\frac{\xi R_{\text{ch}}(M)}{R_\oplus}\right)^{-1}. \tag{5.12}$$

Using this definition for the limiting temperature, the radius of the hot white dwarf is written as $R \propto (T_{\text{lim}} - T)^{-1}$.

In Fig.5.8, we show T_{lim} as function of mass M. The light gray circles are the effective temperature distribution as a function of mass. The blue region represents the forbidden region for the effective temperature of hot DA-WD. In fact, there is not a single point in the bulk of the region, which indicates that this temperature limit exhibits a physical behavior of data, although it is a mathematical limit of our model.

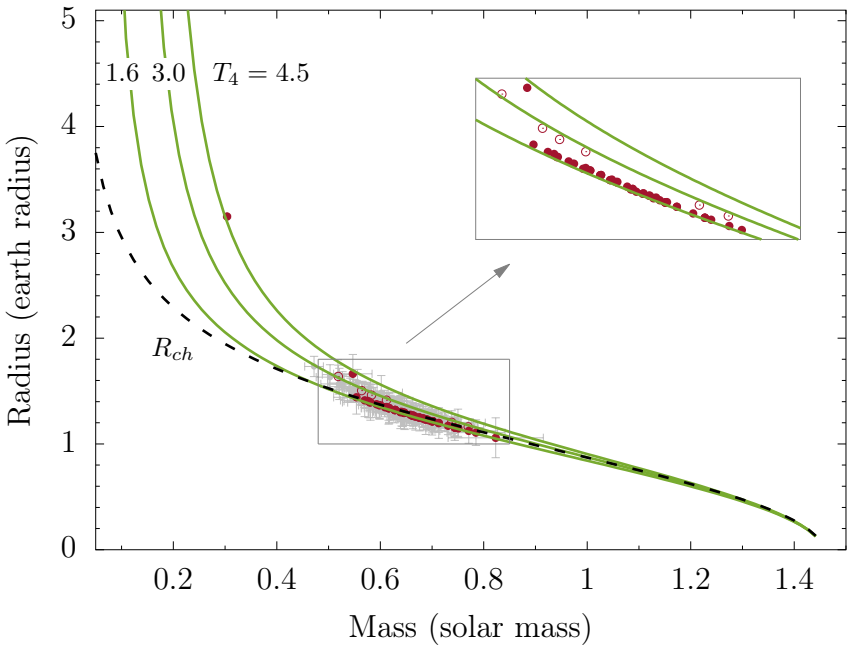

Figure 5.6: Semi-empirical mass-radius relation for DB-WD with different effective temperatures. The red circles represent some values of effective temperature and the green lines are their correspondent fits. The light gray circles are the available data for DB-WD from the SDSS-DR7. The dashed line corresponds to the Chandrasekhar model for ideal white dwarfs stars.

Table 5.1: The estimated radii for the observed DA white dwarf stars from Eclipsing Binaries.

Name	$T_{\rm eff}$ (K)	$M_{\rm eclipse}$ ($M_\odot$)	$R_{\rm eclipse}$ ($R_\oplus$)	R ($R_\oplus$)	Ref
CSS 41177A	22,500(60)	0.378(0.023)	2.425(0.045)	2.64(0.21)	1
NN Ser	63,000(3000)	0.535(0.012)	2.27(0.02)	2.31(0.12)	2
SDSS J0857+0342	37,400(400)	0.514(0.049)	2.69(0.09)	2.11(0.48)	3
SDSS J1212-0123	17,710(40)	0.439(0.050)	1.83(0.01)	2.07(0.28)	4
GK Vir	50,000(670)	0.562(0.014)	1.85(0.03)	1.91(0.07)	4
QS Vir	14,220(350)	0.781(0.013)	1.165(0.008)	1.14(0.02)	5
V471 Tau	34,500(1000)	0.840(0.050)	1.17(0.08)	1.10(0.08)	6

References. 1) Bours et al. [158], 2) Parsons et al. [159], 3) Parsons et al. [160], 4) Parsons et al. [161], 5) Parsons et al. [162], 6) O'Brien et al. [163].

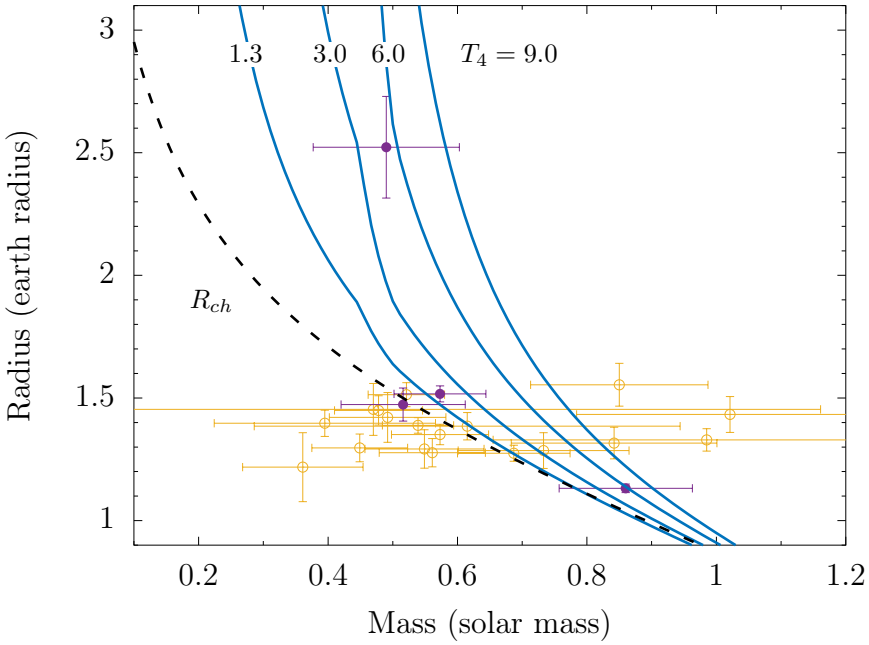

Figure 5.7: Semi-empirical mass-radius relation for DA-WD with different effective temperatures (blue lines). The purple solid circles correspond to the directly observed DA-WD and the yellow open circles are the DA-WD observed in wide binaries from the *Gaia* DR1. The dashed line is the Chandrasekhar mass-radius relation for ideal WD.

5.3 Central Temperature and Nuclear Ignition in White Dwarfs

Although astronomical observables are stellar atmospheric quantities, the stellar interior quantities are of great importance to astrophysics. For instance, the central temperature and the central density determine the chemical evolution of the star and its nuclear energy generation.

The relation between effective temperature and central temperature is given by Koester [164] in the approximated form

$$\frac{T_{\rm eff}^4}{g} = 2.05 \times 10^{-10} T_c^{2.56} \tag{5.13}$$

where g is the surface gravity. This relation was obtained by fitting the data from simulations and give us a good estimate of the central temperature inside WD stars.

We can estimate the central temperature of WD-data from SDSS-DR7, using their radii, mass and effective temperature. In Figure 5.9 we represent these data as the gray circles.

Using our semi-empirical mass-radius relation, we can obtain the central tem-

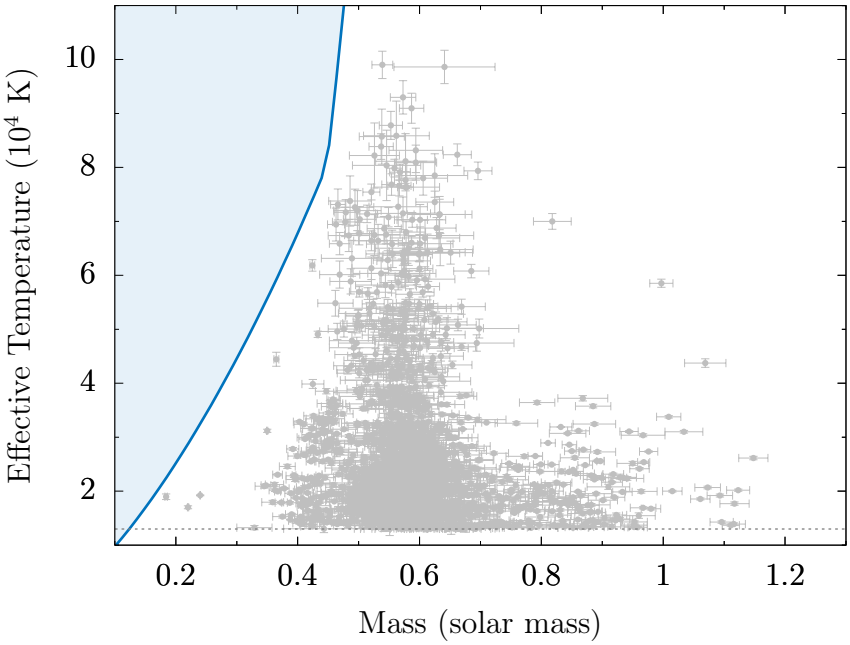

Figure 5.8: Effective temperature limit as a function of mass for DA-WD (blue line). The blue region represents the forbidden region of the effective temperature to the correspondent mass of DA-WD. The light gray circles are the available data for DA-WD from the SDSS-DR7. The dot line corresponds to the temperature threshold for ideal white dwarfs stars.

perature of WD using just their effective temperatures and their masses, since their radii can be calculated with this relation. The central temperature of DA-WDs as a function of their effective temperature is plotted for different mass values in Figure 5.9, as blue lines.

The ignition of the nuclear material inside the white dwarf is determined by the balance between nuclear energy generation rate and local heat losses. We consider the case where the heat losses are mainly caused by neutrino emission, which is appropriate in white dwarfs, e.g., for modeling Type Ia supernova events Ref.[26]. The ignition temperature for the material depends on the central density of the star. We use the fitting formula for ignition temperature for carbon and oxygen fusions as a function of mass density, the Eq.(A.1) in Ref.[128]. The central densities for white dwarfs with different masses are calculated using the hydrostatic equilibrium equation with the EoS of degenerate electrons, i.e., hydrostatic equilibrium for ideal white dwarfs. This assumption is enough *a posteriori* because the temperature corrections to the EoS are important just above the ignition temperature for oxygen. In Figure 5.9 we represent both carbon and oxygen ignition lines as the dashed lines, using the Eq.(5.13) to estimate the correspondent effective temperature.

In Table 5.2 we present six DA-WD with central temperature (the last column)

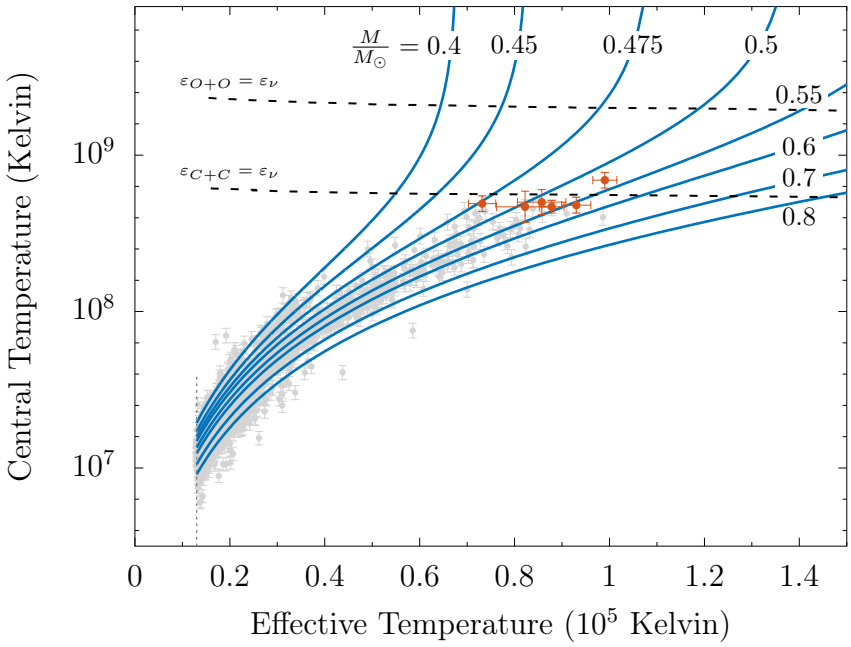

Figure 5.9: Central temperature as a function of the effective temperature for DA-WD with different masses (blue lines). The gray circles represent the central temperature to each DA-WD star in the available data from the SDSS-DR7, and the orange circles are the highest central temperature for WD from these data. The dashed lines are the ignition curves for carbon and oxygen fusions. The dotted line is our effective temperature threshold for hot white dwarfs.

Table 5.2: The highest estimated central temperature determined for the observed DA white dwarf stars from *SDSS*-DR7.

Name	M ($M_\odot$)	R ($R_\oplus$)	$T_{\rm eff}$ (K)	$\log T_c$ (K)
200646.50-124410.9	0.539(0.017)	3.959(0.546)	99,018(2529)	8.84(0.05)
091442.70+041455.9	0.538(0.037)	3.445(0.692)	85,714(5102)	8.70(0.08)
113303.70+290223.0	0.466(0.012)	4.375(0.577)	73,149(2867)	8.69(0.05)
102624.05+091554.8	0.573(0.021)	2.957(0.335)	92,989(3088)	8.68(0.05)
224653.73-094834.5	0.553(0.019)	3.077(0.313)	87,805(2600)	8.67(0.04)
080403.06+083030.8	0.526(0.041)	3.406(0.799)	82,219(6036)	8.67(0.10)

above 99% of the carbon ignition temperature, represented by the orange circles in Figure 5.9. The star 200646.50-124410.9 is a special case because it is the only one WD above the carbon ignition line. The fact that this WD did not become a supernova can be understood by its internal composition, i.e., if there is more oxygen then carbon in its core, we expect no ignition inside this WD. We suggest that more careful observations and more detailed simulations must be directed to the modeling of this WD star.

5.4 Estimating Masses of Hot White Dwarfs

One of the great achievements in white dwarf research has been the capacity to measure the effective temperatures and surface gravities. In particular, the spectroscopic technique developed by Bergeron *et al.* [165] for analyzing the Balmer line of hydrogen in (DA) white dwarfs has become the standard method for measuring the effective temperature and surface gravity of these stars which represent 80% of the white dwarf population. In addition to being infrequent than their hydrogen-line DA counterparts, the hotter DB stars are characterized by an optical spectrum where the neutral helium transitions exhibit little sensitivity to effective temperature, as discussed by Bergeron *et al.* in [166]. The mass-radius relation is fundamental to compute white dwarf masses from these accurate measurements.

Using our semi-empirical mass-radius relation, Eq.(5.11), we can obtain the surface gravity g as a function of the mass M and the effective temperature $T_{\rm eff}$ of the white dwarf star according

$$g(M, T_{\rm eff}) = \frac{GM}{R(M, T_{\rm eff})^2}, \tag{5.14}$$

which we can be numerically invert to obtain the mass of the WD as a function of $T_{\rm eff}$ and $\log g$.

As a test case, the most recent measurements of Sirius B from [167] can be used to determine its mass. Sirius B is a hydrogen-rich DA-WD whose the effective tem-

Table 5.3: The estimated masses for the directly observed DA white dwarf stars from the *Gaia*-DR1.

Name	$T_{\rm eff}$ (K)	$\log g$ (cm/s^2)	$M_{\rm Gaia}$ ($M_\odot$)	M ($M_\odot$)
0232+035	66,950(1440)	7.40(0.07)	0.490(0.113)	0.518(0.013)
1314+293	56,800(1250)	7.89(0.07)	0.516(0.096)	0.644(0.028)
1647+591	12,510(200)	8.34(0.05)	0.860(0.103)	0.807(0.031)
2117+539	14,680(240)	7.91(0.05)	0.573(0.071)	0.561(0.025)

perature is 24,790(100) K and the surface gravity is $\log g = 8.57(0.06)$. Then, using the Eq.(5.14), we can obtain the mass value of $M = 0.960(0.035)\ M_\odot$. This result is close to the refined estimates of the mass $M = 1.034(0.026)\ M_\odot$ using other method of measurement, as the *Hipparcos* parallax method.

Another example would be the PG0948+534 reported by [168] as currently one of the hottest DA white dwarf stars. The authors were able to measure the $T_{\rm eff}$ and the $\log g$ for this WD, finding $T_{\rm eff} = 110{,}000$ K and $\log g = 7.58$. For the case of PG0948+534, we find the mass value of $M = 0.640\ M_\odot$, that corroborates the hypothesis of DA hot white dwarfs with mass between $0.5 - 0.7\ M_\odot$ are the hottest observed DA stars, as can be seen in Figure 5.9.

The best test is to compare our mass estimates with direct mass measurements by independent methods, such as those presented in *Gaia*-DR1 at Ref. [157]. As discussed in the Section 5.2, the data of directly observed DA-WD are in better agreement with our model than the data of wide binaries WD. In Table 5.3, we estimate the mass (the last column) using the atmospheric measurements of effective temperature and surface gravity for these WD, by Eq.(5.14), and compare with the observed mass $M_{\rm Gaia}$ (the fourth column).

5.5 Discussion and Conclusion

Introducing a very simple model for the outer layer of hot WDs we analyzed the *SDSS*-DR7 and derived a simple, analytic semi-phenomenological relation among effective temperature, mass and radius of hot white dwarfs, the Eq.(5.6). The introduced parameters μ and ξ capture the relation among those quantities provided by full evolutionary models, i.e., they are associated with the processes of stellar evolution of white dwarfs.

From this relation, we observe that there are two essential differences between hydrogen-rich DA white dwarf and hydrogen-deficient DB white dwarf: their outer layer composition and their effective temperature range.

As discussed by Sion *et al.* in [169], the DA-WD are much easier to classify because the Balmer lines of hydrogen across a wide range of effective temperature

$T_{\rm eff}$, from 4,000 up to 120,000 K and higher, whereas DB-WD exhibit He I lines but with a lower effective temperature range, from 12,000 to 45,000 K. Confirming the different effective temperature ranges for DA and DB.

The difference in the outer layer composition was presented by the parameter μ of both DA and DB, and it indicates that the parameter is closely related to the mean molecular weight of this region, whose the information give us clues about the chemical composition of the material.

The parameter ξ must be related to the Rosseland optical-depth mentioned in Ref.[170] and it depends on the chemical composition of the material, due to the opacity of the material. The fact of $\xi \lesssim 1$ shows that the region responsible for the photon emission is essentially in the border of the core described by the degenerate electron gas, suggesting that a small portion of this surface is melted into the outer layer.

Our result permits us to obtain a mass-radius relation, the Eq.(5.11), and estimates of radii for WDs for known mass and temperature with other methods. Furthermore, our formula exhibits a mathematical limit to the effective temperature, and curiously there is not a single white dwarf star in the bulk of the forbidden region imposed by this limit. A further study to understand the existence of such a limiting temperature is required.

The central temperature can be evaluated using the relation between effective temperature and surface gravity derived from Koester *et al.* [164] using numerical models of WD. The data from *SDSS*-DR7 present six DA-WD with central temperatures very close to the carbon ignition temperature. There is only one DA-WD with central temperature above the ignition temperature. If our analytic expression reflects the physical systematics correctly, we may think of the possibility that the core of this WD is composed by oxygen instead of carbon. Numerical simulations and future observations are required for the better understanding whether such WD is a possible Type Ia supernova progenitor.

The mass-radius relation obtained in this work allows us to obtain mass estimates from atmospheric measurements of effective temperature and surface gravity. We use this method to estimate masses of the well known Sirius B and other DA-WD from the recent *Gaia*-DR1. Although they are distinct methods, our mass evaluations are in good accordance with the masses measured by *Gaia*, considering their uncertainties. This result confirm our relation, Eq.(5.6), as a great constraining for effective temperature, mass and radius of hot white dwarfs. All these results are compiled in a submitted paper [171].

Chapter 6

Delayed Thermalization in Thermonuclear Supernovae

In every branch of knowledge the progress is proportional to the amount of facts on which to build, and therefore to the facility of obtaining data.

– J. C. Maxwell (1831-1879)

We know that the outburst in Type Ia supernovae are caused by nuclear burning in microscopically thin layers either conductively as subsonic deflagrations or by shock compression as supersonic detonations [e.g., 67, Ch. XIV]. These burning fronts are hydrodynamically unstable to linear spatial perturbations, but they can be stabilized by forming nonlinear cellular structure or become fully turbulent that produce the flame surface growth, increasing the total burning rate [172]. Neither flames nor detonations can be resolved in explosion simulations on stellar scales and therefore must be represented by numerical models [e.g, 26].

In fact, phenomenologically adjusted models based on these mode of burning front propagation were able to fit most of the observational data remarkably well. However, most of these earlier models computed the dynamical evolution of the white dwarf from the time of ignition through disruption assuming spherical symmetry on all scales and intrinsically non-spherical effects such as convective mixing and transport were included in some parametrized form. Moreover, since it is well know that the laminar speed of a deflagration front propagating in the deep interior of a dense white dwarf is by far insufficient to lead to the desired explosion and provide at least $0.5 M_\odot$ of radioactive ^{56}Ni to power the light curve [e.g., 173]. So, an acceleration of the front due to some unknown mechanism had to be assumed to achieve the necessary detonation [174].

On the other hand, it has also been realized rather early that the matter behind

the deflagration front suffers hydrodynamic instabilities, including the Rayleigh-Taylor instability, and Woosley [175] introduced the concept of a fractal dimension of the flame surface into supernova models in order to account for these effects. But as before, the models did not resolve numerically all relevant length scales.

6.1 Retardation Effects in Hydrodynamical Calculations

Though in the past several years hydrodynamical simulations have been extended to two and three dimensions, the most recent and state-of-art 3D hydrodynamical calculations are beyond the computational capacity to reconstruct the details of microscopic fluid motion. The typical fluid elements of order 1 km^3 are assumed in thermodynamic equilibrium, where the matter is homogeneous and there are no gradients of thermodynamic quantities. However, in a highly unstable regime the fluid motion may be infinitely complicated on scales smaller than the fluid element, and these complex fluid motion will thermalize on finite timescales. Therefore, the thermodynamic equilibrium within the fluid element is a good approximation only when the timescale of thermalization is negligible compared to the other relevant timescale the hydrodynamic timescale.

In the one-dimensional modeling of the hydrodynamical evolution many degrees of freedom are embedded within a shell. However, from the preceding considerations it is natural to expect that there exist transient processes such as convective mixing, vortices, collective motion and other instabilities on smaller and smaller scales which must delay the thermalization of the burning matter, and that retardation will effect the propagation of the flame or detonation. One then expects that the thermalization of the burning matter may not be instantaneous on the relevant timescales, and that such retardation effects will influence the propagation of the burning fronts. Thus, the heat generated by these microscopically irreversible process will take some time to be equilibrated as heat in the matter.

In this case, the entropy balance equation should be modified as

$$T\frac{\mathrm{d}S}{\mathrm{d}t} = [\dot{Q}] - L, \tag{6.1}$$

where the original heat term, accounting for the dissipative work rate and the nuclear energy generation, given by

$$\dot{Q} = -q\frac{\mathrm{d}V}{\mathrm{d}t} + \epsilon M \tag{6.2}$$

and the delayed dissipative-reactive source term described by

$$[\dot{Q}] = \int_{-\infty}^{t} G(t,t')\dot{Q}(t')\mathrm{d}t', \tag{6.3}$$

where $G(t,t')$ denotes the probability that the heat dissipated by turbulence or generated by nuclear reactions at time t' will appear as heat at time t. This retardation effect will be more important if the size of the hydrodynamical cell is extremely macroscopic, as is the case in present supernova calculations.

The specified form of $G(t,t')$ depends on the dynamical details of how the microscopic hydrodynamic motion turns to heat, which we have no knowledge currently. However, we expect that it should satisfy certain general conditions:

(1) be normalized , i.e. $\int_{-\infty}^{\infty} G(t,t')\mathrm{d}t' = 1$;

(2) be a function of $t - t'$, i.e., the retardation process is Markovian;

(3) should be zero for large $t - t'$;

(4) the principal effect can be represented by a single relaxation time τ.

The two most simple possibilities for $G(t,t')$ that satisfy the above conditions are

$$G(t,t') = \delta(t - t' - \tau), \tag{6.4}$$

or

$$G(t,t') = \frac{1}{\tau} e^{-(t-t')/\tau}. \tag{6.5}$$

From a practical point of view, the possibility (6.5) is more convenient, since the integral expression for $[\dot{Q}]$ in Eq.(6.3) can be transformed into a differential equation as

$$\frac{\mathrm{d}[\dot{Q}]}{\mathrm{d}t} = \frac{1}{\tau}\left(\dot{Q} - [\dot{Q}]\right). \tag{6.6}$$

which is similar to the Maxwell-Cattaneo equations (2.50) for the dissipative currents.

The Figure 6.1 illustrates the delayed thermalization for a simple heat distribution. The original heat distribution $\dot{Q}$ is a Gaussian peaked at 0.4 s and width of 0.03 s, represented as the blue dashed line. The orange and yellow lines represent the delayed distributions $[\dot{Q}]$ with $\tau = 100$ ms and $\tau = 200$ ms, respectively. Therefore, we can note that as the delay time increases the maximum of the distribution decreases and the distribution itself becomes larger. All these distributions return the same deposited energy after a long time.

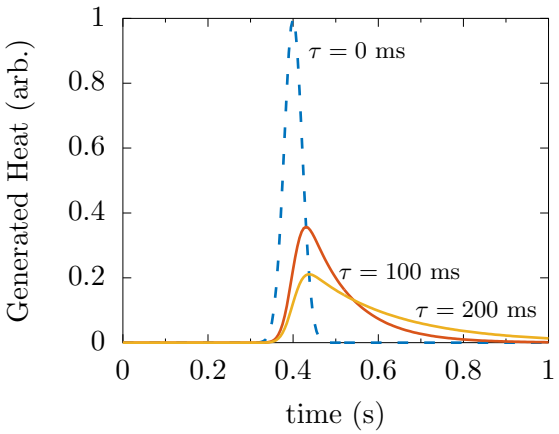

Figure 6.1: The generated heat as a function of time. The original distribution is a Gaussian centered at 0.4 s with width 0.03 s, represented as the dashed blue line. The orange and yellow lines represent the delayed distributions with $\tau = 100$ ms and $\tau = 200$ ms, respectively.

6.2 sub-Chandrasekhar Supernovae

The calculations were performed for several models with different values of the delay parameter τ. The progenitor for all these models is a sub-Chandrasekhar-mass WD star (1.08 $M_\odot$) composed of equal mass fractions of ^{12}C and ^{16}O ($X = 0.5$) with 0.08 $M_\odot$ He-rich material accreted, totalizing 1.16 $M_\odot$ described by $N = 116$ shells with 0.01 $M_\odot$ mass each one. This progenitor is motivated by the case A model from Nomoto *et al.* [54] with the helium matter accreted at a constant accretion rate of $\mathrm{d}M/\mathrm{d}t = 3 \times 10^{-8} M_\odot \mathrm{yr}^{-1}$, resulting in a helium burning at near surface shell $M_r = 1.13\ M_\odot$, i.e., the shell with 1.13 $M_\odot$ inside.

Our initial condition is assumed to be in hydrostatic equilibrium, with the described helium burning producing a large overpressure as seen from the spike in the initial pressure distribution in Figure 6.4. The nuclear energy released at this shell results in a steep temperature peak of $T = 3 \times 10^9$ K in that region.

6.2.1 Effects on the shock wave propagration

The nuclear burning leads to an increase of temperature and the nuclear energy rate ϵ because of high electron degeneracy. The heat transport becomes negligible as compared with ϵ, and the heat is retained in the burning region. As a consequence the temperature increases rapidly at a time scale of $\tau_{\mathrm{nuc}} = c_p T/\epsilon$, where c_p is the specific heat at constant pressure. When τ_{nuc} becomes shorter than the dynamical scale $\tau_{\mathrm{dyn}} = (24\pi G\rho)^{-1/2}$, the temperature runaway becomes a deflagration and the temperature at $\tau_{\mathrm{nuc}} = \tau_{\mathrm{dyn}}$ is the deflagration temperature. The deflagration releases the nuclear energy rapidly and yields an overpressure, i.e., a shock front is

formed.

The off-center ignition, in our initial condition, results in an overpressure which forms double shock waves which propagate both outward and inward. Initially, the shock waves are as strong as $P_{\rm sh}/P_0 \sim 800$ for the inward and $P_{\rm sh}/P_0 \sim 40$ for the outward at the adjacent shells. This overpressure created by the heat of the burning products is sufficiently high to form a hydrodynamical shock wave. The resulting shock wave ignites the fuel by compressional heating in a self-sustaining combustion front, a detonation wave. The double detonations move supersonically and do not allow the unburned medium to expand before it is burned. Their speed depends mainly on the ratio of the total amount of energy released per unit mass over the internal energy, i.e., ϵ/u_0. The delayed thermalization can affect this ratio during the detonation wave propagation leading to a shock wave damping.

The outgoing wave is so strong that the shock temperature $T_{\rm sh}$ reaches 2×10^9 K which much higher than the deflagration temperature of helium, $T_{\rm def}({\rm He})$. The helium is then deflagrated into NSE composition, and consequently the shock grows into a helium detonation wave (He-DW) which propagates outward. The inward shock wave initially propagates through the helium zone of 0.05 $M_\odot$ just below the ignited shell. It forms a helium detonation wave which propagates inward. The precursor shock wave then reaches the CO core and is also strong enough to deflagrate the carbon, $T_{\rm sh} > T_{\rm def}({\rm C})$, and a carbon detonation wave (C-DW) forms and propagates inward while incinerating the material into NSE composition.

The double detonation waves propagate self-consistently, i.e., double precursor shock waves are strong enough to keep $T_{\rm sh}$ higher than both $T_{\rm def}({\rm He})$ and $T_{\rm def}({\rm C})$. The propagation of the double detonation waves and the accompanying changes in the radial coordinates are shown in Figure 6.2. The profiles of temperature, pressure and radial velocity are represented in Figure 6.4 for the inward C-DW without the delayed thermalization effects.

When we introduce the time delay τ the evolution of the radial coordinates changes calmly. For $\tau = 2$ ms (Figure 6.3), the shock wave propagates inward slower than for $\tau = 0$ ms (Figure 6.2). However, this shock wave remains strong enough to maintain the carbon detonation inward incinerating whole star. The outgoing shock wave (SW) is represented both in Figure 6.2 and Figure 6.3, and it is also slower in the case with delay $\tau = 2$ ms than the case without delay.

The double detonation waves do not always form. With $\tau = 4$ ms the helium flash near the surface is also explosive, with the precursor shock as strong as $P_{\rm sh}/P_0 \sim 600$, but smaller than that in case with $\tau = 0$. The resultant postshock temperature is $T_{\rm sh} \sim 4 \times 10^9$ is higher than $T_{\rm def}({\rm He}) = 1.3 \times 10^8$ K giving origin to a helium detonation wave forms which propagates outward while incinerating helium matter. On the other hand, $T_{\rm sh}$ decreases as the shock wave propagates inward due

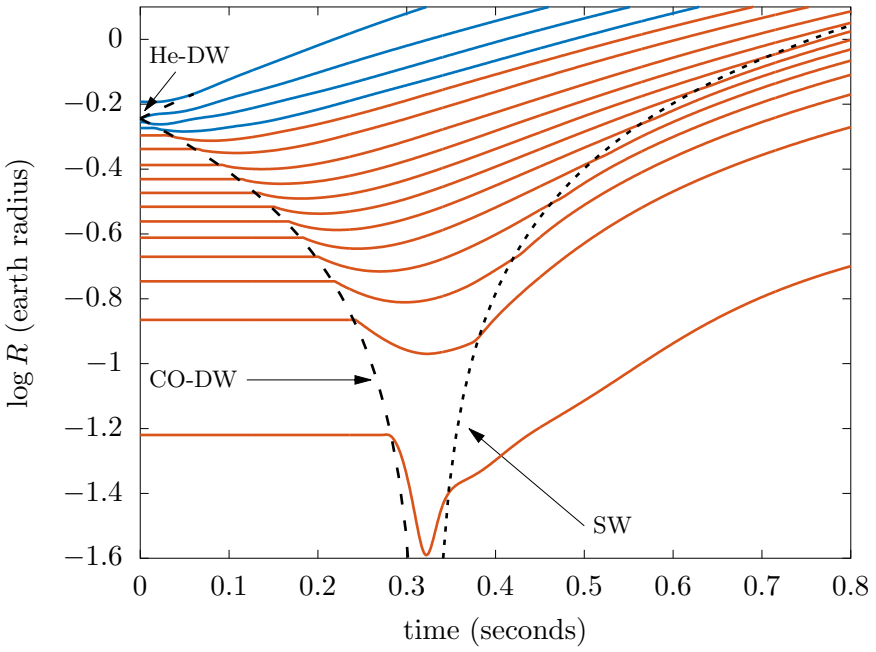

Figure 6.2: Propagation of the double detonation waves *(dashed lines)* and the corresponding changes of the radial coordinates of the Lagrangian shells *(solid lines)* as a function of time without time delay ($\tau = 0$ ms). The blue lines represent the helium accreted shells and the orange lines represent the CO core.

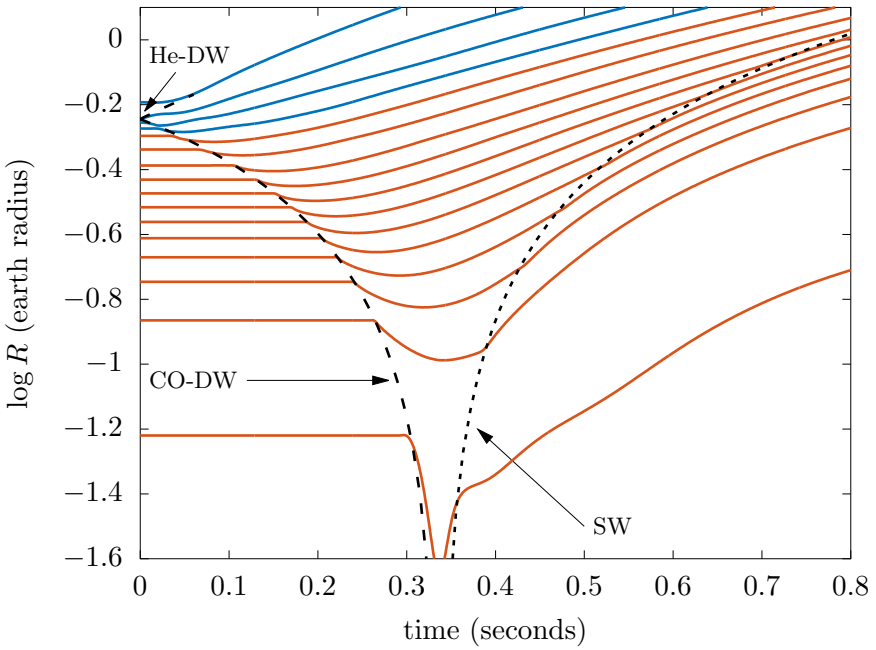

Figure 6.3: Propagation of the double detonation waves *(dashed lines)* and the corresponding changes of the radial coordinates of the Lagrangian shells *(solid lines)* as a function of time for time delay $\tau = 2$ ms. The color scale is the same as Figure 6.2.

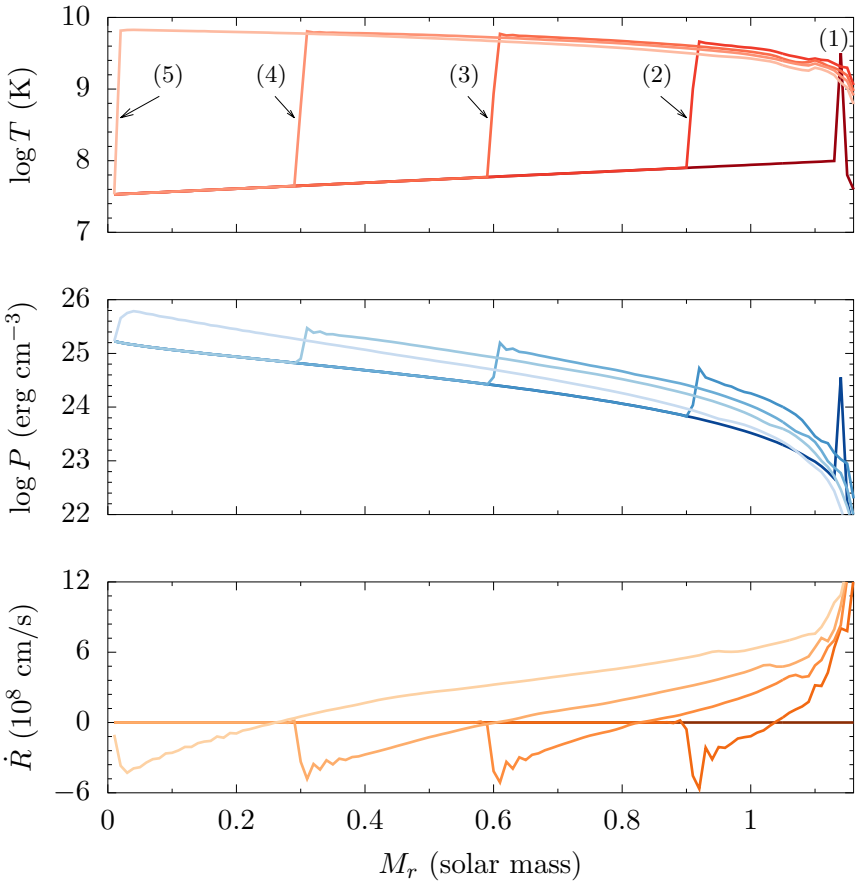

Figure 6.4: The temperature, pressure and radial velocity profiles at time (1) t = 0, (2) t = 92 ms, (3) t = 151 ms, (4) t = 201 ms, (5) t = 280 ms without time delay ($\tau = 0$).

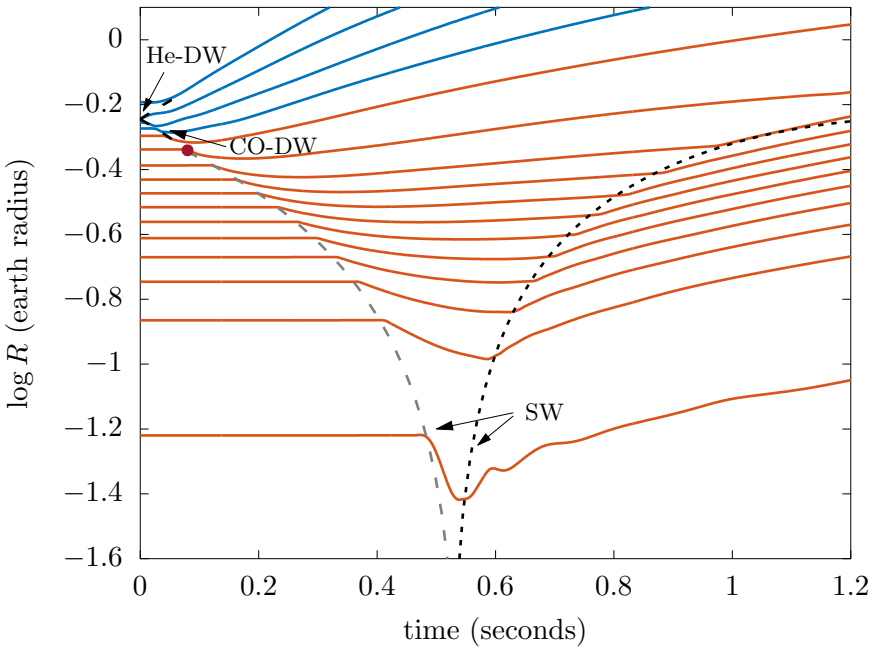

Figure 6.5: Propagation of the double detonation waves *(dashed lines)* and the corresponding changes of the radial coordinates of the Lagrangian shells *(solid lines)* as a function of time for time delay $\tau = 4$ ms. The red circle represents the Lagrangian shell $M(r) = 1.0\ M_\odot$ where the detonation ceases. The shock wave *(light dotted line)* which propagates inward into the CO core is not able to induce a carbon detonation. The color scale is the same as Figure 6.2.

to the delayed thermalization. Then, $T_{\rm sh}$ becomes smaller than $T_{\rm def}({\rm C}) = 1.3 \times 10^9$ K and the detonation ceases. Although the shock wave propagates inward into the CO core, it becomes too weak at $M(r) = 1.0\ M_\odot$ to form an inward carbon detonation wave, as can be seen in Figure 6.5. In fact, such a wave does not induce the inward carbon detonation because of the pressure damping due to the delayed thermalization. This damping effect can be seen in pressure profiles and the consequent decrease in temperature as showed in Figure 6.6.

We should remark, however, that for $\tau > 4$ ms the combustion becomes restricted just to the helium layers of helium. In that case, the total energy of the CO core is still negative, so that is remains at rest. There is no supernova in these cases.

6.2.2 Effects on the energetics of explosion and nucleosynthesis

The double detonation nucleosynthesis is quite simple. The inward carbon detonation incinerates all materials in the CO core into NSE composition, i.e., in our simulations ^{4}He, ^{28}Si and ^{56}Ni. The electron capture is too slow such that neutronization in NSE composition is negligible. Therefore, the NSE composition becomes

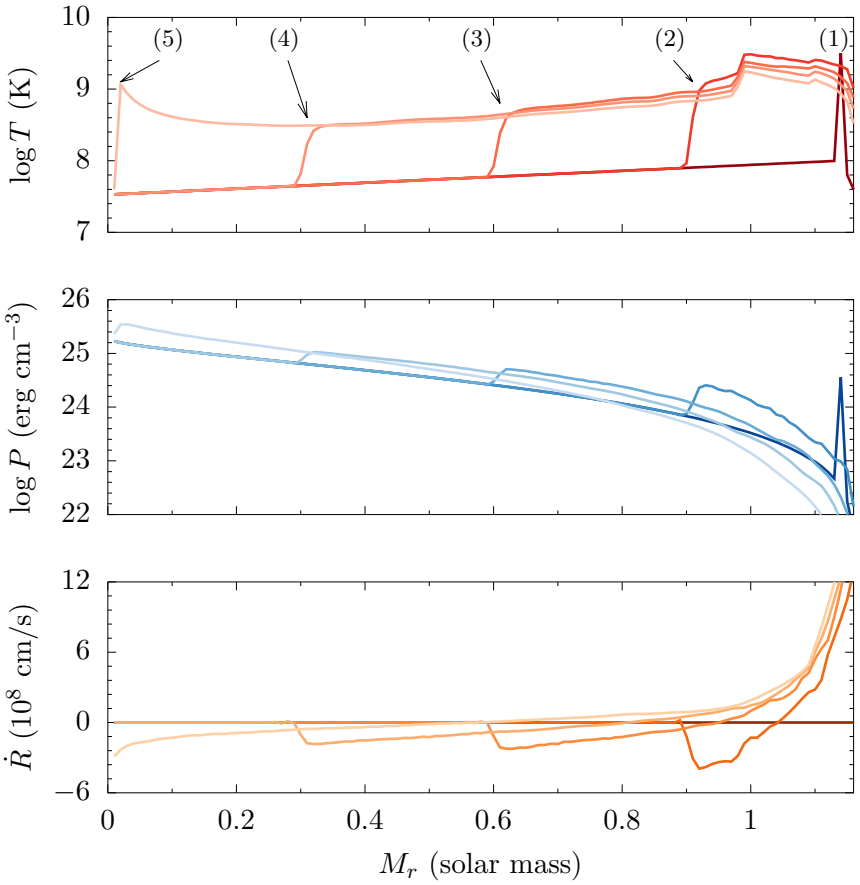

Figure 6.6: The temperature, pressure and radial velocity profiles at time (1) t = 0, (2) t = 120 ms, (3) t = 233 ms, (4) t = 333 ms, (5) t = 495 ms with time delay $\tau = 4$ ms.

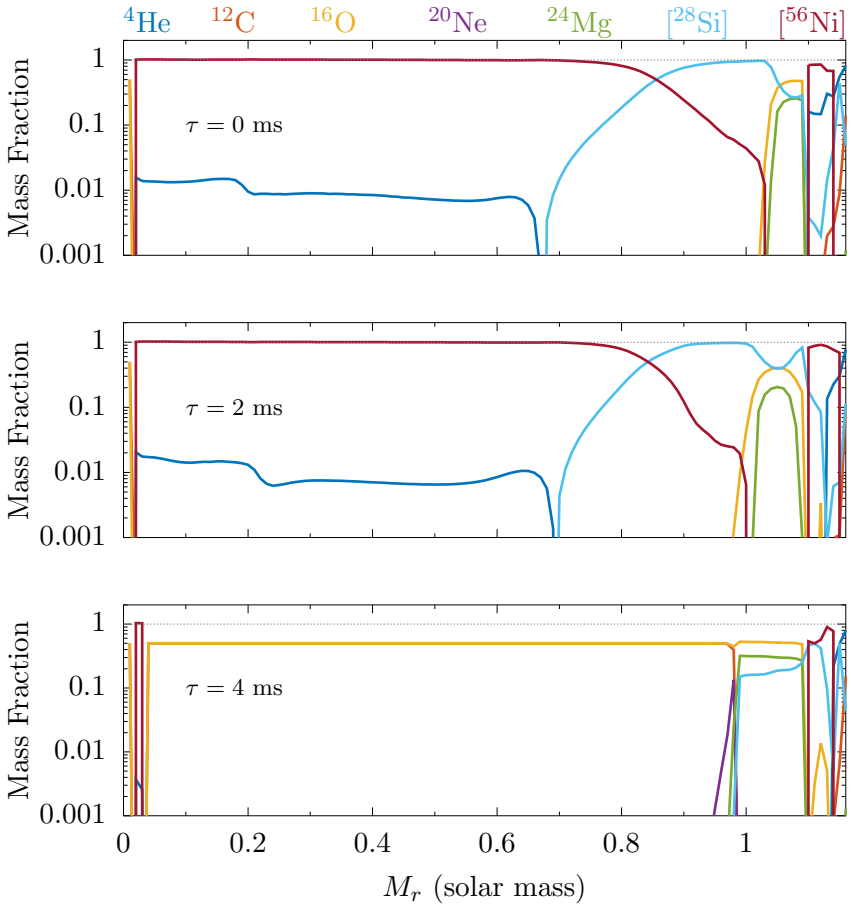

Figure 6.7: The final mass fractions of the seven isotopes for different values of time delay parameter τ.

^{56}Ni as the temperature decreases due to expansion. The outward helium detonation als incinerates most of the initial helium zone into NSE composition which becomes ^{56}Ni in later stages due to the low density. The He-CO transition layer is the appropriate region to produce the intermediate-mass elements as ^{28}Si, because there the α-capture reaction proceeds partially and may synthesize these IME in those low density layers. This pattern of nucleosynthesis is retrieved by our numerical calculations until $\tau = 3$ ms, as represented by Figure 6.7.

There is an abrupt fall in ^{56}Ni production for $\tau > 3$ ms. This is because, as discussed earlier, the inward shock wave is not strong enough to induce a carbon detonation which results in no carbon combustion at CO core, as represented in Figure 6.7 for the $\tau = 4$ ms case. This failure in the nickel-group element nucleosynthesis is presented in Table 6.1.

The main observable affected by the variation in [^{56}Ni] mass is the peak luminosity, which correlates with the explosion energy. This energy is essentially the nuclear energy released during the explosion minus the initial binding energy. Therefore, for the same initial condition, the greater is the nickel amount produced by the ex-

Table 6.1: Nucleosynthetic yields of selected species and nickel radial velocity for different values of the time delay parameter τ.

τ (ms)	$M[^4\mathrm{He}]$ ($M_\odot$)	$M[^{12}\mathrm{C}]$ ($M_\odot$)	$M[^{16}\mathrm{O}]$ ($M_\odot$)	$M[^{20}\mathrm{Ne}]$ ($M_\odot$)	$M[^{24}\mathrm{Mg}]$ ($M_\odot$)	$M[^{28}\mathrm{Si}]$ ($M_\odot$)	$M[^{56}\mathrm{Ni}]$ ($M_\odot$)	$v_{^{56}\mathrm{Ni}}$ (km/s)
0	0.030	0.006	0.029	5.62(-6)	0.011	0.206	0.886	1.7(4)
1.0	0.025	0.006	0.015	6.87(-6)	2.36(-4)	0.226	0.896	1.7(4)
2.0	0.020	0.006	0.032	4.63(-6)	0.010	0.220	0.878	1.6(4)
3.0	0.021	0.006	0.059	6.11(-6)	0.029	0.216	0.835	1.6(4)
3.5	0.015	0.461	0.535	4.93(-4)	0.044	0.049	0.056	1.5(4)
4.0	0.015	0.480	0.536	0.001	0.034	0.040	0.054	1.5(4)
4.5	0.015	0.495	0.542	0.001	0.028	0.037	0.042	1.5(4)
5.0	0.015	0.506	0.541	0.001	0.022	0.036	0.039	1.5(4)

Notes: Numbers in parenthesis correspond to powers of ten. $v_{^{56}\mathrm{Ni}}$ is the velocity of the ejecta shell that bounds 99% of the total ^{56}Ni mass.

Table 6.2: Energetics of explosion for different values of the time delay parameter τ.

τ (ms)	Binding Energy E_{bin} (erg)	Nuclear Energy E_{nuc} (erg)	Explosion Energy E_{exp} (erg)
0	2.4×10^{50}	1.8×10^{51}	1.6×10^{51}
1.0	2.4×10^{50}	1.9×10^{51}	1.7×10^{51}
2.0	2.4×10^{50}	1.8×10^{51}	1.6×10^{51}
3.0	2.4×10^{50}	1.7×10^{51}	1.5×10^{51}
3.5	2.4×10^{50}	2.9×10^{50}	5.2×10^{49}
4.0	2.4×10^{50}	2.6×10^{50}	1.6×10^{49}
4.5	2.4×10^{50}	2.3×10^{50}	...
5.0	2.4×10^{50}	2.2×10^{50}	...
10.0	2.4×10^{50}	1.8×10^{50}	...

plosion, the greater is the nuclear energy released, and consequently the greater is the explosion energy. The Table 6.2 presents the binding energy E_{bin}, the nuclear energy E_{nuc} and the explosion energy E_{exp} for models with different values of delay parameter τ.

All these results can be compiled into a simple plot which relates the nuclear energy released with the amount of silicon- and nickel-group elements synthesized during the WD combustion when the delayed thermalization is considered, represented by different single time delay parameter τ as in Figure 6.8.

6.3 Discussion and Conclusion

The time delay in our delayed thermalization model results from assuming that the transformation of microscopic kinetic and nuclear energies into thermal energy

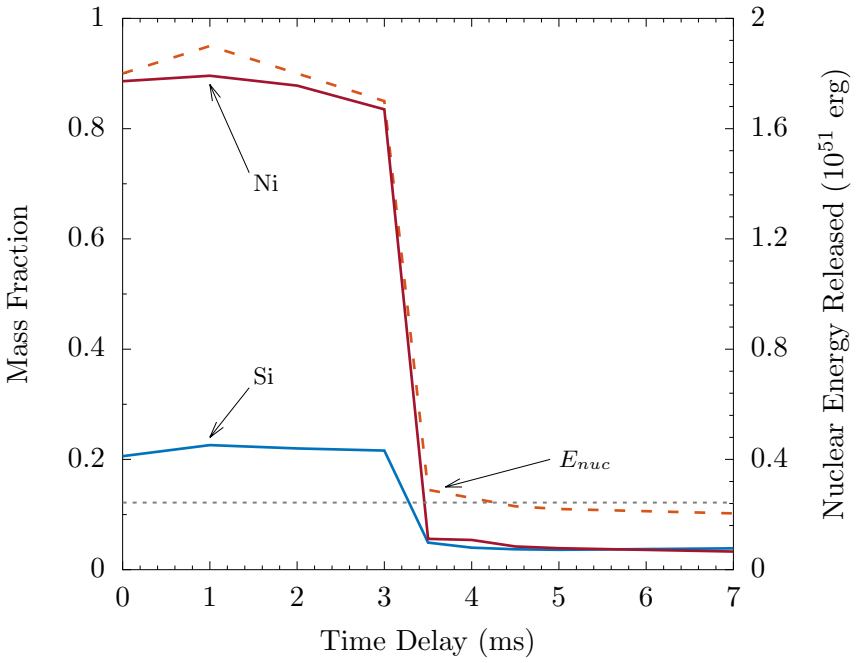

Figure 6.8: The mass fractions of silicon-group elements (*blue solid line*) and nickel-group elements (*red solid line*) and the nuclear energy released during the explosion (*orange dashed line*) versus the delay time parameter τ. The dotted line represents the binding energy.

---

is not instantaneous on timescales relevant for the supernova explosion. We account the associated physical process as a gradual transfer of irreversible entropy to collective degrees of freedom that act on smaller scales. Since most hydrodynamical calculation appeal to dividing the system into a set of interacting macroscopic fluid elements, these retardation effects should be included no matter how small the size of these fluid elements are in practical calculations, because at some stage of the thermalization process they will be larger than some of the collective modes present. The necessary concern which was not addressed here is the size of such retardation effects in physically realistic systems. However, the schematic demonstration in the present work that these retardation effects may strongly influence the hydrodynamical evolution and their observables indicates that serious consideration should be given to such effects in the description of thermonuclear supernovae.

The fundamental indication of the retardation effects in thermonuclear supernovae is the variation in the ^{56}Ni masses produced during the detonation of the carbon-oxygen material. This nucleosynthesis variation introduces diversity in ejecta that have other endorsement as velocity ejecta, kinetic energy, and explosion energy. It is thus no surprise that this variation in the nickel-group mass [^{56}Ni] and in the intermediate-mass group [^{28}Si] provide the main contrast in model results. From $\tau = 0$ to 3 ms, the velocity of the ejecta shell that bounds 99% of the total ^{56}Ni mass

is almost the same $\sim$ 17000 km s^{-1}, while the mass of synthesized ^{56}Ni is approximately $\sim 0.88 M_{\odot}$. This amount of ^{56}Ni is large enough to provide energy input for the light curve of SN I. On the other hand, for $\tau > 3$ ms the synthesized mass of ^{56}Ni is below $\sim 0.06\ M_{\odot}$ and it is not sufficient for light curves, since the minimum mass of ^{56}Ni required to power the SN I light curves was estimated to be $\sim 0.2\ M_{\odot}$ [e.g., 36].

We can associate this sharp transition with the characteristic timescale for hydrodynamic processes, the Courant-Friedrich timescale related to the propagation of disturbations with the sound velocity inside the fluid element, given by $\tau_{CFL} = \delta R / c_s \approx 4$ ms. Being this value accurately correlated with the timescale associated with the transition from a explosion by double detonation in a sub-Chandrasekhar WD to a single outward He-detonation, as presented by Figure 6.8. This coupling of timescales should be investigated more carefully.

We also know that in the present calculation the artificial viscosity can somehow be overestimated due to the small number of shells $N = 116$, which eventually damps the propagation of shock waves. We have performed a calculation for $N = 1160$ shells without delay, and found that important differences appear when compared to the our case shown in Figure 6.2. In particular, the final configuration for the last few shells becomes unbound early, showing that the number of shells used here is not sufficient to describe the detailed behavior of the external shells. However, the present model is intended to be schematic.

Besides that, it is not the purpose of the present work to claim that the introduction of retardation effects is able to solve the apparent issues about the deflagration-to-detonation transition of the one-dimensional calculations of realistic supernova models. Such calculations should not only increase the number of shells, but also include many more ingredients, such as the interaction of shock waves and turbulent flow. Furthermore, it appears that two- and three-dimensional treatments may lead to quite different behavior of the time evolution of the system. The point that we would like to stress is that the relative importance of those retardation effects should remain the same in these multidimensional calculations.

Of course, our result are resumed for only one initial condition. The fact that we do not know whether some SNe Ia come from sub-Chandrasekhar or Chandrasekhar mass explosions is still confusing. We expect reproduce this calculations for other initial conditions currently discussed as possible progenitors.

Lastly, differentiating between these various models can be improved by detailed radiative transfer simulations to match the observed evolution of SN Ia light curves and spectra form early to late times. All these results will be compiled in a paper [176].

Chapter 7

Epilogue

Every atom in your body came from a star that exploded. And, the atoms in your left hand probably came from a different star than your right hand. It really is the most poetic thing I know about physics: You are all stardust. You couldn't be here if stars hadn't exploded, because the elements - the carbon, nitrogen, oxygen, iron, all the things that matter for evolution and for life - weren't created at the beginning of time. They were created in the nuclear furnaces of stars, and the only way for them to get into your body is if those stars were kind enough to explode.... The stars died so that you could be here today.

– Lawrence Krauss (1954-)

Non-equilibrium thermodynamic is still the object of study of many scientists in diverse areas of knowledge. The near-equilibrium and the linear treatment discussed here is the essence of the development of human knowledge and technological applications. We start with the equilibrium thermodynamic and we search the neighborhood of these states of equilibrium like a detective looking for clues to a crime. However, although much has been learned, there is a long road to deal with far-from-equilibrium phenomena.

We have learned that for most of his life, the WD stars are in stationary states with their radiative luminosity coming from the thermal energy stored in the plasma inside them. Their radii and consequently their effective temperatures remain in constant change throughout their entire life. The degenerate matter keeps the WD in hydrostatic equilibrium while the ions in the outer layers keep the star hot. The photons cannot cross the outermost layers without colliding many times, and the

consequence of this block is an isothermal core surrounding by a tiny but relentless atmosphere. The observed radius, mass and effective temperature are direct quantities of this atmosphere and they provide us with information about its internal composition.

But not everything is so calm during the life of white dwarfs. When they are in binary systems, they can receive a lot of pure helium mass and start a supernova. These glorious thermonuclear explosions may be triggered by the carbon fusion and produce a good amount of the nickel present in the universe. Explosions, of coure, are not quite states of matter. They release a lot of energy in a tiny region of the star, and the resulting shock waves propagate with ultrasound velocities. Thus, non-equilibrium thermodynamic can be an alternative way to describe these complex and transient phenomena.

Bibliography

Journal Article references

[1] Koester, D. and Weidemann, V. "White dwarf constraints on mass loss rates and models of galactic evolution". In: *Astronomy & Astrophysics* 81.1 (1980), pp. 145–151. DOI: 1980A&A....81..145K (see p. 1).

[2] Heger, A., Fryer, C. L., Woosley, S. E., Langer, N., and Hartmann, D. H. "How Massive Single Stars End Their Life". In: *The Astrophysical Journal* 591 (July 2003), pp. 288–300. DOI: 10.1086/375341. eprint: astro-ph/0212469 (see p. 1).

[4] Woosley, S E and Heger, Alexander. "THE REMARKABLE DEATHS OF 9–11 SOLAR MASS STARS". In: *The Astrophysical Journal* 810.1 (Aug. 2015), p. 34. ISSN: 1538-4357. DOI: 10.1088/0004-637X/810/1/34. arXiv: 1505.06712 (see p. 2).

[5] Liebert, James, Bergeron, P., Eisenstein, Daniel, Harris, H. C., Kleinman, S. J., Nitta, Atsuko, and Krzesinski, Jurek. "A Helium White Dwarf of Extremely Low Mass". In: *The Astrophysical Journal* 606.2 (May 2004), pp. L147–L149. ISSN: 0004-637X. DOI: 10.1086/421462 (see p. 2).

[6] Fowler, R. H. "On Dense Matter". In: *Monthly Notices of the Royal Astronomical Society* 87.2 (Dec. 1926), pp. 114–122. ISSN: 0035-8711. DOI: 10.1093/mnras/87.2.114 (see p. 2).

[7] Nauenberg, Michael. "Analytic Approximations to the Mass-Radius Relation and Energy of Zero-Temperature Stars". In: *The Astrophysical Journal* 175 (July 1972), p. 417. ISSN: 0004-637X. DOI: 10.1086/151568 (see p. 3).

[8] Chandrasekhar, Subrahmanyan. "The Highly Collapsed Configurations of a Stellar Mass". In: *Monthly Notices of the Royal Astronomical Society* 91 (1931), pp. 456–466 (see pp. 5, 69).

[10] Kleinman, S. J., Kepler, S. O., Koester, D., Pelisoli, Ingrid, Peçanha, Viviane, Nitta, A., Costa, J. E. S., Krzesinski, J., Dufour, P., Lachapelle, F.-R., Bergeron, P., Yip, Ching-Wa, Harris, Hugh C., Eisenstein, Daniel J., Althaus, L. G., and Córsico, A. "SDSS DR7 WHITE DWARF CATALOG". In: *The Astrophysical Journal Supplement Series* 204.1 (Jan. 2013), p. 5. ISSN: 0067-0049. DOI: 10.1088/0067-0049/204/1/5 (see pp. 5, 6, 70, 72).

[11] Marshak, R. E. "The Internal Temperature of White Dwarf Stars." In: *The Astrophysical Journal* 92 (Nov. 1940), p. 321. ISSN: 0004-637X. DOI: 10.1086/144225 (see pp. 5, 37, 69).

[12] Hubbard, W. B. and Wagner, Raymond L. "Hot White Dwarfs". In: *The Astrophysical Journal* 159 (Jan. 1970), p. 93. ISSN: 0004-637X. DOI: 10.1086/150292 (see pp. 5, 69).

[13] Carvalho, S. M. de, Rotondo, M., Rueda, Jorge A., and Ruffini, R. "Relativistic Feynman-Metropolis-Teller treatment at finite temperatures". In: *Physical Review C* 89.1 (Jan. 2014), p. 015801. ISSN: 0556-2813. DOI: 10.1103/PhysRevC.89.015801 (see pp. 5, 69).

[14] Ade, P. A. R. et al. "Planck 2013 results. XVI. Cosmological parameters". In: *Astronomy & Astrophysics* 571 (Nov. 2014), A16. ISSN: 0004-6361. DOI: 10.1051/0004-6361/201321591 (see p. 6).

[15] Fontaine, G., Brassard, P., and Bergeron, P. "The Potential of White Dwarf Cosmochronology". In: *Publications of the Astronomical Society of the Pacific* 113.782 (Apr. 2001), pp. 409–435. ISSN: 0004-6280. DOI: 10.1086/319535 (see p. 6).

[17] Koester, D and Chanmugam, G. "Physics of white dwarf stars". In: *Reports on Progress in Physics* 53.7 (1990), pp. 837–915. ISSN: 0034-4885. DOI: 10.1088/0034-4885/53/7/001 (see pp. 7, 69).

[18] Schatzman, Evry. "Théorie du débit d'énergie des naines blanches". In: *Annales d'Astrophysique* 8 (1945), p. 143. ISSN: 1098-6596 (see p. 7).

[19] Sion, E. M., Greenstein, J. L., Landstreet, J. D., Liebert, J., Shipman, H. L., and Wegner, G. A. "A proposed new white dwarf spectral classification system". In: *The Astrophysical Journal* 269 (June 1983), p. 253. ISSN: 0004-637X. DOI: 10.1086/161036 (see p. 7).

[21] Kepler, S. O., Kleinman, S. J., Nitta, A., Koester, D., Castanheira, B. G., Giovannini, O., Costa, a. F M, and Althaus, L. "White dwarf mass distribution in the SDSS". In: *Monthly Notices of the Royal Astronomical Society* 375.4 (Feb. 2007), pp. 1315–1324. ISSN: 00358711. DOI: 10.1111/j.1365-2966.2006.11388.x (see pp. 7, 70).

[22] Dufour, P., Liebert, J., Fontaine, G., and Behara, N. "White dwarf stars with carbon atmospheres". In: *Nature* 450.7169 (Nov. 2007), pp. 522–524. ISSN: 0028-0836. DOI: 10.1038/nature06318. arXiv: arXiv:0711.3227v1 (see p. 7).

[23] Dufour, P., Fontaine, G., Liebert, James, Schmidt, G. D., and Behara, N. "Hot DQ White Dwarfs: Something Different". In: *The Astrophysical Journal* 683.2 (Aug. 2008), pp. 978–989. ISSN: 0004-637X. DOI: 10.1086/589855. arXiv: 0805.0331 (see p. 8).

[24] Kepler, S O, Koester, Detlev, and Ourique, Gustavo. "A white dwarf with an oxygen atmosphere." en. In: *Science (New York, N.Y.)* 352.6281 (Apr. 2016), pp. 67–9. ISSN: 1095-9203. DOI: 10.1126/science.aad6705 (see p. 8).

[25] Hillebrandt, W., Kromer, M., Röpke, F. K., and Ruiter, A. J. "Towards an understanding of Type Ia supernovae from a synthesis of theory and observations". In: *Frontiers of Physics* 8.2 (2013), pp. 116–143. ISSN: 20950462. DOI: 10.1007/s11467-013-0303-2 (see p. 8).

[26] Hillebrandt, Wolfgang and Niemeyer, Jens C. "Type Ia Supernova Explosion Models". In: *Annual Review of Astronomy and Astrophysics* 38.1 (Sept. 2000), pp. 191–230. ISSN: 0066-4146. DOI: 10.1146/annurev.astro.38.1.191 (see pp. 9, 80, 85).

[28] Howell, D Andrew. "Type Ia supernovae as stellar endpoints and cosmological tools." In: *Nature communications* 2 (Jan. 2011), p. 350. ISSN: 2041-1723. DOI: 10.1038/ncomms1344 (see p. 9).

[29] Nielsen, Jeppe Trøst, Guffanti, Alberto, and Sarkar, Subir. "Marginal evidence for cosmic acceleration from Type Ia supernovae". In: *Nature Publishing Group* (2015), p. 5. ISSN: 2045-2322. DOI: 10.1038/srep35596. arXiv: 1506.01354 (see p. 9).

[30] Matteucci, F. and Greggio, L. "Relative roles of type I and II supernovae in the chemical enrichment of the interstellar gas". In: *Astronomy and Astrophysics* 154 (1986), pp. 279–287. ISSN: 0004-6361 (see p. 9).

[31] Matteucci, Francesca and Recchi, Simone. "On the Typical Timescale for the Chemical Enrichment from Type Ia Supernovae in Galaxies". In: *The Astrophysical Journal* 558.1 (Sept. 2001), pp. 351–358. ISSN: 0004-637X. DOI: 10.1086/322472. arXiv: 0105074 [astro-ph] (see p. 9).

[32] Matteucci, F., Panagia, N., Pipino, A., Mannucci, F., Recchi, S., and Della Valle, M. "A new formulation of the Type Ia supernova rate and its consequences on galactic chemical evolution". In: *Monthly Notices of the Royal Astronomical Society* 372.1 (2006), pp. 265–275. ISSN: 00358711. DOI: 10.1111/j.1365-2966.2006.10848.x (see p. 9).

[33] Branch, D., Buta, R., Falk, S. W., McCall, M. L., Uomoto, A., Wheeler, J. C., Wills, B. J., and Sutherland, P. G. "Interpretation of the maximum light spectrum of a Type I supernova". In: *The Astrophysical Journal* 252 (Jan. 1982), p. L61. ISSN: 0004-637X. DOI: 10.1086/183720 (see pp. 9, 14).

[34] Riess, Adam G., Filippenko, Alexei V., Challis, Peter, Clocchiatti, Alejandro, Diercks, Alan, Garnavich, Peter M., Gilliland, Ron L., Hogan, Craig J., Jha, Saurabh, Kirshner, Robert P., Leibundgut, B., Phillips, M. M., Reiss, David, Schmidt, Brian P., Schommer, Robert A., Smith, R. Chris, Spyromilio, J., Stubbs, Christopher, Suntzeff, Nicholas B., and Tonry, John. "Observational Evidence from Supernovae for an Accelerating Universe and a Cosmological Constant". In: *The Astronomical Journal* 116.3 (Sept. 1998), pp. 1009–1038. ISSN: 00046256. DOI: 10.1086/300499. arXiv: 9805201 [astro-ph] (see p. 9).

[35] Perlmutter, S., Aldering, G., Goldhaber, G., Knop, R. A., Nugent, P., Castro, P. G., Deustua, S., Fabbro, S., Goobar, A., Groom, D. E., Hook, I. M., Kim, A. G., Kim, M. Y., Lee, J. C., Nunes, N. J., Pain, R., Pennypacker, C. R., Quimby, R., Lidman, C., Ellis, R. S., Irwin, M., McMahon, R. G., Ruiz-Lapuente, P., Walton, N., Schaefer, B., Boyle, B. J., Filippenko, A. V., Matheson, T., Fruchter, A. S., Panagia, N., Newberg, H. J. M., Couch, W. J., and Project, The Supernova Cosmology. "Measurements of Ω and Λ from 42 High-Redshift Supernovae". In: *The Astrophysical Journal* 517.2 (June 1999), pp. 565–586. ISSN: 0004-637X. DOI: 10.1086/307221. arXiv: 9812133 [astro-ph] (see p. 9).

[36] Wheeler, J C and Harkness, R P. "Type I supernovae". In: *Reports on Progress in Physics* 53.12 (Dec. 1990), pp. 1467–1557. ISSN: 0034-4885. DOI: 10.1088/0034-4885/53/12/001 (see pp. 9, 14, 97).

[37] Arnett, W. David. "Type I supernovae. I - Analytic solutions for the early part of the light curve". In: *The Astrophysical Journal* 253.1 (Feb. 1982), pp. 785–797. ISSN: 0004-637X. DOI: 10.1086/159681 (see pp. 9, 10).

[38] Stritzinger, M., Mazzali, P. A., Sollerman, J., and Benetti, S. "Consistent estimates of 56 Ni yields for type Ia supernovae". In: *Astronomy and Astrophysics* 460.3 (2006), pp. 793–798. ISSN: 0004-6361. DOI: 10.1051/0004-6361:20065514. arXiv: 0609232 [astro-ph] (see p. 10).

[39] Colgate, Stirling A. and McKee, Chester. "Early Supernova Luminosity". In: *The Astrophysical Journal* 157 (1969), p. 623. ISSN: 0004-637X. DOI: 10.1086/150102 (see p. 10).

[40] Nadyozhin, D. K. "The properties of NI to CO to Fe decay". In: *The Astrophysical Journal Supplement Series* 92.100 (June 1994), p. 527. ISSN: 0067-0049. DOI: 10.1086/192008 (see p. 10).

[41] Dado, Shlomo and Dar, Arnon. "ANALYTICAL EXPRESSIONS FOR LIGHT CURVES OF ORDINARY AND SUPERLUMINOUS TYPE Ia SUPERNOVAE". In: *The Astrophysical Journal* 809.1 (Aug. 2015), p. 32. ISSN: 1538-4357. DOI: 10.1088/0004-637X/809/1/32 (see p. 10).

[42] Arnett, W. David, Fryer, Christopher L., and Matheson, Thomas. "Early identification of Type I supernova light curves". In: *preprint arXiv:1611.08746* 2013 (2016), pp. 1–17 (see p. 10).

[43] Pereira, R, Thomas, R C, Aldering, G, Antilogus, P, Baltay, C, Benitez-Herrera, S, Bongard, S, Buton, C, Canto, A, Cellier-Holzem, F, Chen, J, Childress, M, Chotard, N, Copin, Y, Fakhouri, H K, Fink, M, Fouchez, D, Gangler, E, Guy, J, Hillebrandt, W, Hsiao, E Y, Kerschhaggl, M, Kowalski, M, Kromer, M, Nordin, J, Nugent, P, Paech, K, Pain, R, Pécontal, E, Perlmutter, S, Rabinowitz, D, Rigault, M, Runge, K, Saunders, C, Smadja, G, Tao, C, Taubenberger, S, Tilquin, A, and Wu, C. "Spectrophotometric time series of SN 2011fe from the Nearby Supernova Factory". In: *Astronomy & Astrophysics* 554.2012 (June 2013), A27. ISSN: 0004-6361. DOI: 10.1051/0004-6361/201221008. arXiv: 1302.1292 (see pp. 10, 11).

[44] Phillips, M. M. "The absolute magnitudes of Type IA supernovae". In: *The Astrophysical Journal* 413 (1993), p. L105. ISSN: 0004-637X. DOI: 10.1086/186970. arXiv: 9912123 [astro-ph] (see p. 10).

[45] Kasen, Daniel and Woosley, S. E. "On the Origin of the Type Ia Supernova Width-Luminosity Relation". In: *The Astrophysical Journal* 656.2 (2007), pp. 661–665. ISSN: 0004-637X. DOI: 10.1086/510375 (see p. 10).

[46] Jha, Saurabh, Riess, Adam G., and Kirshner, Robert P. "Improved Distances to Type Ia Supernovae with Multicolor Light-Curve Shapes: MLCS2k2". In: *The Astrophysical Journal* 659.1 (Apr. 2007), pp. 122–148. ISSN: 0004-637X. DOI: 10.1086/512054. arXiv: 0612666 [astro-ph] (see p. 10).

[47] Coelho, Rodrigo C V, Calvão, Maurício O, Reis, Ribamar R R, and Siffert, Beatriz B. "Standardization of type Ia supernovae". In: *European Journal of Physics* 36.1 (2015), p. 015007. ISSN: 0143-0807. DOI: 10.1088/0143-0807/36/1/015007. arXiv: 1411.3596 (see p. 10).

[48] Filippenko, Alexei V., Richmond, Michael W., Branch, David, Gaskell, Martin, Herbst, William, Ford, Charles H., Treffers, Richard R, Matheson, Thomas, Ho, Luis C, Dey, Arjun, Sargent, Wallace L W, Small, Todd A, and Breugel, Wil J. M. van. "The subluminous, spectroscopically peculiar type IA supernova 1991bg in the elliptical galaxy NGC 4374". In: *The Astronomical Journal* 104.4 (Oct. 1992), p. 1543. ISSN: 00046256. DOI: 10.1086/116339 (see p. 11).

[49] Maoz, D. and Mannucci, F. "Type-Ia supernova rates and the progenitor problem: A review". In: *Publications of the Astronomical Society of Australia* 29.4 (2012), pp. 447–465. ISSN: 13233580. DOI: 10.1071/AS11052 (see p. 12).

[50] Iben, I., Jr. and Tutukov, a. V. "On the evolution of close binaries with components of initial mass between 3 solar masses and 12 solar masses". In: *The Astrophysical Journal Supplement Series* 58 (Aug. 1985), p. 661. ISSN: 0067-0049. DOI: 10.1086/191054. arXiv: 1985ApJS...58..661I (see p. 12).

[51] Nomoto, K and Sugimoto, D. "Rejuvenation of Helium White Dwarfs by Mass Accretion". In: *Publications of the Astronomical Society of Japan* 29 (1977), pp. 765–780 (see p. 12).

[52] Nomoto, Ken'ichi and Kondo, Yoji. "Conditions for accretion-induced collapse of white dwarfs". In: *The Astrophysical Journal* 367 (Jan. 1991), p. L19. ISSN: 0004-637X. DOI: 10.1086/185922 (see p. 12).

[53] Whelan, John and Iben, Icko, Jr. "Binaries and Supernovae of Type I". In: *The Astrophysical Journal* 186 (Dec. 1973), p. 1007. ISSN: 0004-637X. DOI: 10.1086/152565 (see p. 12).

[54] Nomoto, K. "Accreting white dwarf models for type I supernovae. I - Presupernova evolution and triggering mechanisms". In: *The Astrophysical Journal* 253 (Feb. 1982), p. 798. ISSN: 0004-637X. DOI: 10.1086/159682 (see pp. 12, 14, 88).

[55] Iben, I., Jr. and Tutukov, A. V. "Supernovae of type I as end products of the evolution of binaries with components of moderate initial mass (M not greater than about 9 solar masses)". In: *The Astrophysical Journal Supplement Series* 54 (Feb. 1984), p. 335. ISSN: 0067-0049. DOI: 10.1086/190932 (see p. 12).

[56] Webbink, R. F. "Double white dwarfs as progenitors of R Coronae Borealis stars and Type I supernovae". In: *The Astrophysical Journal* 277 (Feb. 1984), p. 355. ISSN: 0004-637X. DOI: 10.1086/161701. arXiv: 1984ApJ...277..355W (see p. 12).

[57] Nomoto, K., Thielemann, Friedrich-Karl, and Yokoi, K. "Accreting white dwarf models of Type I supernovae. III - Carbon deflagration supernovae". In: *The Astrophysical Journal* 286 (1984), p. 644. ISSN: 0004-637X. DOI: 10.1086/162639 (see pp. 13, 14).

[58] Maoz, Dan, Mannucci, Filippo, and Nelemans, Gijs. "Observational Clues to the Progenitors of Type Ia Supernovae". In: *Annual Review of Astronomy and Astrophysics* 52.1 (2014), pp. 107–170. ISSN: 0066-4146. DOI: 10.1146/annurev-astro-082812-141031 (see p. 12).

[59] Hoyle, F and Fowler, William A. "Nucleosynthesis in Supernovae." In: *The Astrophysical Journal* 132 (Nov. 1960), p. 565. ISSN: 0004-637X. DOI: 10.1086/146963 (see p. 12).

[60] Takarada, Katsuo, Sato, Humitaka, and Hayashi, Chushiro. "Central Temperature and Density of Stars in Gravitational Equilibrium". In: *Progress of Theoretical Physics* 36.3 (Sept. 1966), pp. 504–514. ISSN: 0033-068X. DOI: 10.1143/PTP.36.504 (see p. 13).

[61] Arnett, W. David. "A possible model of supernovae: Detonation of 12C". In: *Astrophysics and Space Science* 5.2 (Oct. 1969), pp. 180–212. ISSN: 0004-640X. DOI: 10.1007/BF00650291 (see p. 14).

[62] Nomoto, K. "Accreting white dwarf models for Type I supernovae. II - Off-center detonation supernovae". In: *The Astrophysical Journal* 257 (June 1982), p. 780. ISSN: 0004-637X. DOI: 10.1086/160031 (see pp. 14, 15).

[63] Friedrich Konrad Röpke. "Following multi-dimensional type Ia supernova explosion models to homologous expansion". In: *Astronomy and Astrophysics* 432.3 (Mar. 2005), pp. 969–983. ISSN: 0004-6361. DOI: 10.1051/0004-6361:20041700 (see p. 14).

[64] Röpke, F. K., Seitenzahl, I. R., Benitez, S., Fink, M., Pakmor, R., Kromer, M., Sim, S. A., Ciaraldi-Schoolmann, F., and Hillebrandt, W. "Modeling Type Ia supernova explosions". In: *Progress in Particle and Nuclear Physics* 66.2 (2011), pp. 309–318. ISSN: 01466410. DOI: 10.1016/j.ppnp.2011.01.026 (see p. 14).

[65] Long, Min, Jordan, George C., Rossum, Daniel R. van, Diemer, Benedikt, Graziani, Carlo, Kessler, Richard, Meyer, Bradley, Rich, Paul, and Lamb, Don Q. "THREE-DIMENSIONAL SIMULATIONS OF PURE DEFLAGRATION MODELS FOR THERMONUCLEAR SUPERNOVAE". In: *The Astrophysical Journal* 789.2 (July 2014), p. 103. ISSN: 0004-637X. DOI: 10.1088/0004-637X/789/2/103 (see p. 14).

[66] Arnett, W. David and Clayton, D D. "Explosive nucleosynthesis in stars." In: *Nature* 227.5260 (Aug. 1970), pp. 780–4. ISSN: 0028-0836. DOI: 10.1038/227780a0 (see p. 14).

[68] Branch, D, Doggett, J. B., Nomoto, K., and Thielemann, Friedrich-Karl. "Accreting white dwarf models for the type I supernovae. IV The optical spectrum of a carbon-deflagration supernova". In: *The Astrophysical Journal* 294 (1985), p. 619. ISSN: 0004-637X. DOI: 10.1086/163329 (see p. 14).

[69] Woosley, S. E. and Weaver, Thomas A. "Sub-Chandrasekhar mass models for Type IA supernovae". In: *The Astrophysical Journal* 423.1 (Mar. 1994), pp. 371–379. ISSN: 0004-637X. DOI: 10.1086/173813 (see pp. 14, 15).

[70] Niemeyer, J. C. and Woosley, S. E. "The Thermonuclear Explosion Of Chandrasekhar Mass White Dwarfs". In: *The Astrophysical Journal* 475 (1997), pp. 740–753. ISSN: 0004-637X. DOI: 10.1086/303544 (see pp. 14, 39).

[71] Shigeyama, Toshikazu, Nomoto, Ken'ichi, Yamaoka, Hitoshi, and Thielemann, Friedrich-Karl. "Possible models for the type IA supernova 1990N". In: *The Astrophysical Journal* 386 (Feb. 1992), p. L13. ISSN: 0004-637X. DOI: 10.1086/186281 (see p. 14).

[72] Yamaoka, Hitoshi, Nomoto, Ken'ichi, Shigeyama, Toshikazu, and Thielemann, Friedrich-Karl. "Late detonation models for the type IA supernovae SN 1991T and SN 1990N". In: *The Astrophysical Journal* 393 (July 1992), p. L55. ISSN: 0004-637X. DOI: 10.1086/186450 (see p. 14).

[73] Nomoto, Ken'ichi, Sugimoto, Daiichiro, and Neo, Sadayuki. "Carbon deflagration supernova, an alternative to carbon detonation". In: *Astrophysics and Space Science* 39.2 (Feb. 1976), pp. L37–L42. ISSN: 0004-640X. DOI: 10.1007/BF00648354 (see p. 14).

[74] Khokhlov, AM. "Mechanisms for the initiation of detonations in the degenerate matter of supernovae". In: *Astronomy and Astrophysics* 246 (1991), pp. 383–396 (see pp. 14, 48).

[75] Khokhlov, Alexei M., Oran, Elaine S., and Wheeler, J. Craig. "Deflagration to Detonation Transition in Thermonuclear Supernovae". In: *The Astrophysical Journal* 478 (1996), p. 28. ISSN: 0004-637X. DOI: 10.1086/303815 (see p. 14).

[76] Blondin, S, Dessart, Luc, Hillier, D. J., and Khokhlov, A. M. "One-dimensional delayed-detonation models of Type Ia supernovae: confrontation to observations at bolometric maximum". In: *Monthly Notices of the Royal Astronomical Society* 429.3 (Mar. 2013), pp. 2127–2142. ISSN: 0035-8711. DOI: 10.1093/mnras/sts484. arXiv: arXiv:1211.5892v1 (see p. 15).

[77] Niemeyer, J. C. "Can Deflagration-Detonation Transitions Occur in Type Ia Supernovae?" In: *The Astrophysical Journal* 523.1 (Sept. 1999), pp. L57–L60. ISSN: 0004637X. DOI: 10.1086/312253 (see p. 15).

[78] Lisewski, a. M., Hillebrandt, Wolfgang, and Woosley, S. E. "Constraints On The Delayed Transition to Detonation in Type Ia Supernovae". In: 1 (1999), p. 18. ISSN: 0004-637X. DOI: 10.1086/309158 (see p. 15).

[79] Fink, M., Hillebrandt, Wolfgang, and Röpke, Friedrich Konrad. "Double-detonation supernovae of sub-Chandrasekhar mass white dwarfs". In: *Astronomy and Astrophysics* 476.3 (Dec. 2007), pp. 1133–1143. ISSN: 0004-6361. DOI: 10.1051/0004-6361:20078438 (see p. 15).

[80] Sim, S. A., Röpke, F. K., Hillebrandt, W., Kromer, M., Pakmor, R., Fink, M., Ruiter, A. J., and Seitenzahl, I. R. "DETONATIONS IN SUB-CHANDRASEKHAR-MASS C+O WHITE DWARFS". In: *The Astrophysical Journal* 714.1 (May 2010), pp. L52–L57. ISSN: 2041-8205. DOI: 10.1088/2041-8205/714/1/L52 (see p. 15).

[81] McKernan, B. and Ford, K. E. S. "On the resonant detonation of sub-Chandrasekhar mass white dwarfs during binary inspiral". In: *Monthly Notices of the Royal Astronomical Society* 463.2 (Dec. 2016), pp. 2039–2045. ISSN: 0035-8711. DOI: 10.1093/mnras/stw2068. arXiv: 1608.06294 (see p. 15).

[82] Stritzinger, M., Leibundgut, B., Walch, S., and Contardo, G. "Constraints on the progenitor systems of type Ia supernovae". In: *Astronomy and Astrophysics* 450.1 (2006), pp. 241–251. ISSN: 0004-6361. DOI: 10.1051/0004-6361:20053652. arXiv: 0506415 [astro-ph] (see p. 15).

[83] Ruiz-Lapuente, Pilar. "New approaches to SNe Ia progenitors". In: *New Astronomy Reviews* 62-63 (2014), pp. 15–31. ISSN: 13876473. DOI: 10.1016/j.newar.2014.08.002 (see p. 15).

[84] Maeda, Keiichi and Terada, Yukikatsu. "Progenitors of type Ia supernovae". In: *International Journal of Modern Physics D* 25.10 (Sept. 2016), p. 1630024. ISSN: 0218-2718. DOI: 10.1142/S021827181630024X (see p. 15).

[87] Denicol, Gabriel S, Heinz, Ulrich, Martinez, Mauricio, Noronha, Jorge, and Strickland, Michael. "New Exact Solution of the Relativistic Boltzmann Equation and its Hydrodynamic Limit". In: *Phys. Rev. Lett.* 113.20 (Nov. 2014), p. 202301. DOI: 10.1103/PhysRevLett.113.202301 (see p. 21).

[88] Denicol, G S, Niemi, H, Molnár, E, and Rischke, D H. "Derivation of transient relativistic fluid dynamics from the Boltzmann equation". In: *Phys. Rev. D* 85.11 (June 2012), p. 114047. DOI: 10.1103/PhysRevD.85.114047 (see p. 21).

[89] Onsager, Lars. "Reciprocal Relations in Irreversible Processes. I." In: *Physical Review* 37.4 (Feb. 1931), pp. 405–426. ISSN: 0031-899X. DOI: 10.1103/PhysRev.37.405 (see pp. 25, 27).

[90] Onsager, Lars. "Reciprocal Relations in Irreversible Processes. II." In: *Physical Review* 38.12 (Dec. 1931), pp. 2265–2279. ISSN: 0031-899X. DOI: 10.1103/PhysRev.38.2265 (see p. 25).

[97] Fick, Adolf. "Ueber Diffusion". In: *Annalen der Physik und Chemie* 170.1 (1855), pp. 59–86. ISSN: 00033804. DOI: 10.1002/andp.18551700105 (see p. 25).

[98] Burnett, D. "The distribution of velocities in a slightly non-uniform gas". In: *Proceedings of the London Mathematical Society* s2-39.1 (1935), pp. 385–430. ISSN: 1460244X. DOI: 10.1112/plms/s2-39.1.385 (see p. 26).

[99] Maxwell. J. C. "On the Dynamical Theory of Gases". In: *Philosophical Transactions of the Royal Society of London* 157 (1867), pp. 49–88. DOI: 108968 (see p. 28).

[100] Cattaneo, Carlo. "Sur une forme de lequation de la chaleur eliminant le paradoxe dune propagation instantanee". In: *Comptes Rendus Hebdomadaires Des Seances De L Academie Des Sciences* 247.4 (1958), pp. 431–433 (see p. 28).

[106] Hubbard, W. B. and Lampe, Martin. "Thermal Conduction by Electrons in Stellar Matter". In: *The Astrophysical Journal Supplement Series* 18 (July 1969), pp. 297–346. ISSN: 0067-0049. DOI: 10.1086/190192 (see pp. 39, 58).

[107] Lampe, Martin. "Transport Coefficients of Degenerate Plasma". In: *Physical Review* 170.1 (June 1968), pp. 306–319. ISSN: 0031-899X. DOI: 10.1103/PhysRev.170.306 (see p. 39).

[108] Cassisi, S., Potekhin, Alexander Y., Pietrinferni, A., Catelan, M., and Salaris, M. "Updated Electron-Conduction Opacities: The Impact on Low-Mass Stellar Models". In: *The Astrophysical Journal* 661.2 (June 2007), pp. 1094–1104. ISSN: 0004-637X. DOI: 10.1086/516819 (see pp. 39, 58).

[109] Itoh, N., Mitake, S., Iyetomi, H., and Ichimaru, S. "Electrical and thermal conductivities of dense matter in the liquid metal phase. I - High-temperature results". In: *The Astrophysical Journal* 273 (Oct. 1983), p. 774. ISSN: 0004-637X. DOI: 10.1086/161412 (see p. 39).

[110] Itoh, N., Kohyama, Y., Matsumoto, N., and Seki, M. "Electrical and Thermal Conductivities of Dense Matter in the Crystalline Lattice Phase". In: *The Astrophysical Journal* 285 (1984), p. 758. ISSN: 0004-637X. DOI: 10.1086/162553 (see p. 39).

[111] Mitake, S., Ichimaru, S., and Itoh, N. "Electrical and thermal conductivities of dense matter in the liquid metal phase. II - Low-temperature quantum corrections". In: *The Astrophysical Journal* 277 (Feb. 1984), p. 375. ISSN: 0004-637X. DOI: 10.1086/161704 (see p. 39).

[112] Itoh, Naoki, Hayashi, Hiroshi, and Kohyama, Yasuharu. "Electrical and Thermal Conductivities of Dense Matter in the Crystalline Lattice Phase. III. Inclusion of Lower Densities". In: *The Astrophysical Journal* 418 (Nov. 1993), p. 405. ISSN: 0004-637X. DOI: 10.1086/173401 (see p. 39).

[113] Itoh, Naoki and Kohyama, Yasuharu. "Electrical and Thermal Conductivities of Dense Matter in the Crystalline Lattice Phase. II - Impurity scattering". In: *The Astrophysical Journal* 404 (Feb. 1993), p. 268. ISSN: 0004-637X. DOI: 10.1086/172275 (see p. 39).

[114] Itoh, Noaki, Hayashi, Hiroshi, and Kohyama, Yasuharu. "Electrical and Thermal Conductivities of Dense Matter in the Crystalline Lattice Phase. III. Inclusion of Lower Densities: Erratum". In: *The Astrophysical Journal* 436 (Nov. 1994), p. 418. ISSN: 0004-637X. DOI: 10.1086/174916 (see p. 39).

[115] Baiko, D. A., Kaminker, a D, Potekhin, Alexander Y., and Yakovlev, D. G. "Ion Structure Factors and Electron Transport in Dense Coulomb Plasmas". In: *Phys. Rev. Lett.* 81.25 (1998), pp. 5556–5559. DOI: 10.1103/PhysRevLett.81.5556 (see p. 39).

[116] Potekhin, Alexander Y., Baiko, D. A., Haensel, P., and Yakovlev, D. G. "Transport properties of degenerate electrons in neutron star envelopes and white dwarf cores". In: *Astronomy and Astrophysics* 346 (1999), pp. 345–353. ISSN: 00046361 (see pp. 39, 59).

[117] Potekhin, Alexander Y. "Electron conduction in magnetized neutron star envelopes". In: *Astronomy and Astrophysics* 351 (1999), pp. 787–797. ISSN: 00046361 (see p. 39).

[118] Shternin, P. S. and Yakovlev, D. G. "Electron thermal conductivity owing to collisions between degenerate electrons". In: *Physical Review D* 74.4 (2006), p. 043004. ISSN: 1550-7998. DOI: 10.1103/PhysRevD.74.043004 (see p. 39).

[119] José, Jordi and Iliadis, Christian. "Nuclear astrophysics: the unfinished quest for the origin of the elements". In: *Reports on Progress in Physics* 74.9 (Sept. 2011), p. 096901. ISSN: 0034-4885. DOI: 10.1088/0034-4885/74/9/096901 (see p. 39).

[121] Kunz, R, Fey, M, Jaeger, M, Mayer, A, Hammer, J W, Staudt, G, Harissopulos, S, and Paradellis, T. "Astrophysical Reaction Rate of 12C(α, γ)16O". In: *The Astrophysical Journal* 567 (2002), p. 643. ISSN: 15384357. DOI: 10.1086/338384 (see p. 39).

[122] Cooper, Randall L., Steiner, Andrew W., and Brown, Edward F. "Possible resonances in the 12C + 12C fusion rate and superburst ignition". In: *The Astrophysical Journal* 702.1 (Sept. 2009), pp. 660–671. ISSN: 0004-637X. DOI: 10.1088/0004-637X/702/1/660. arXiv: 0903.3994 (see p. 39).

[123] Beard, M., Afanasjev, A. V., Chamon, L. C., Gasques, L. R., Wiescher, M., and Yakovlev, D. G. "Astrophysical S factors for fusion reactions involving C, O, Ne, and Mg isotopes". In: *Atomic Data and Nuclear Data Tables* 96.5 (2010), pp. 541–566. ISSN: 0092640X. DOI: 10.1016/j.adt.2010.02.005 (see p. 39).

[124] Iliadis, Christian, Anderson, K. S., Coc, Alain, Timmes, F. X., and Starrfield, Sumner. "BAYESIAN ESTIMATION OF THERMONUCLEAR REACTION RATES". In: *The Astrophysical Journal* 831.1 (Oct. 2016), p. 107. ISSN: 1538-4357. DOI: 10.3847/0004-637X/831/1/107. arXiv: 1608.05853 (see p. 39).

[125] Salpeter, Edwin E. and Horn, H. M. van. "Nuclear Reaction Rates at High Densities". In: *The Astrophysical Journal* 155 (1969), p. 183. ISSN: 0004-637X. DOI: 10.1086/149858 (see p. 39).

[126] Gasques, L. R., Afanasjev, a. V., Aguilera, E. F., Beard, M., Chamon, L. C., Ring, P., Wiescher, M., and Yakovlev, D. G. "Nuclear fusion in dense matter: Reaction rate and carbon burning". In: *Physical Review C - Nuclear Physics* 72.2 (2005), pp. 1–14. ISSN: 05562813. DOI: 10.1103/PhysRevC.72.025806 (see p. 39).

[127] Yakovlev, D. G., Gasques, L. R., Afanasjev, A. V., Beard, M., and Wiescher, M. "Fusion reactions in multicomponent dense matter". In: *Physical Review C* 74.3 (Sept. 2006), p. 035803. ISSN: 0556-2813. DOI: 10.1103/PhysRevC.74.035803 (see p. 39).

[128] Potekhin, A Y and Chabrier, G. "Thermonuclear fusion in dense stars". In: *Astronomy & Astrophysics* 538 (Feb. 2012), A115. ISSN: 0004-6361. DOI: 10.1051/0004-6361/201117938 (see pp. 39, 80).

[129] Potekhin, A. Y. and Chabrier, G. "Electron screening effect on stellar thermonuclear fusion". In: *Contributions to Plasma Physics* 53.4-5 (2013), pp. 397–405. ISSN: 08631042. DOI: 10.1002/ctpp.201200094 (see p. 39).

[132] Fowler, William A., Caughlan, Georgeanne R., and Zimmerman, Barbara A. "Termonuclear Reaction Rates". In: *Annual Review of Astronomy and Astrophysics* (1967), pp. 525–570 (see p. 46).

[133] Caughlan, Georgeanne R. and Fowler, William A. "Thermonuclear reaction rates V". In: *Atomic Data and Nuclear Data Tables* 40.2 (1988), pp. 283–334. ISSN: 0092640X. DOI: 10.1016/0092-640X(88)90009-5 (see p. 46).

[134] Timmes, F. X. "Integration of Nuclear Reaction Networks for Stellar Hydrodynamics". In: *The Astrophysical Journal Supplement Series* 124 (1999), p. 241. ISSN: 0067-0049. DOI: 10.1086/313257 (see p. 46).

[135] Truran, J. W., Cameron, A. G. W., and Gilbert, A. "THE APPROACH TO NUCLEAR STATISTICAL EQUILIBRIUM". In: *Canadian Journal of Physics* 44.3 (Mar. 1966), pp. 563–592. ISSN: 0008-4204. DOI: 10.1139/p66-049 (see p. 47).

[136] Kodama, T, Donangelo, R, and Guidry, M W. "Retardation Effects for Shock Wave Formation and Propagation during Supernova Explosions". In: *Elsevier* (2009), pp. 1–23 (see p. 51).

[137] Neumann, J. von and Richtmyer, R. D. "A Method for the Numerical Calculation of Hydrodynamic Shocks". In: *Journal of Applied Physics* 21.3 (1950), p. 232. ISSN: 00218979. DOI: 10.1063/1.1699639 (see p. 57).

[139] Timmes, F. X. and Arnett, Dave. "The Accuracy, Consistency, and Speed of Five Equations of State for Stellar Hydrodynamics". In: *The Astrophysical Journal Supplement Series* 125.1 (1999), pp. 277–294. ISSN: 0067-0049. DOI: 10.1086/313271 (see pp. 57, 133).

[140] Timmes, F. X. and Swesty, F. Douglas. "The Accuracy, Consistency, and Speed of an Electron-Positron Equation of State Based on Table Interpolation of the Helmholtz Free Energy". In: *The Astrophysical Journal Supplement Series* 126.2 (2000), pp. 501–516. ISSN: 0067-0049. DOI: 10.1086/313304 (see pp. 58, 127).

[141] Iben I., Jr. "Thermal pulses; p-capture, alpha-capture, s-process nucleosynthesis; and convective mixing in a star of intermediate mass". In: *The Astrophysical Journal* 196.9 (Mar. 1975), p. 525. ISSN: 0004-637X. DOI: 10.1086/153433 (see p. 58).

[142] Timmes, F. X., Hoffman, R. D., and Woosley, S. E. "An Inexpensive Nuclear Energy Generation Network for Stellar Hydrodynamics". In: *The Astrophysical Journal Supplement Series* 129.1 (2000), pp. 377–398. ISSN: 0067-0049. DOI: 10.1086/313407 (see pp. 59, 67).

[143] Kutta, Wilhelm. "Beitrag zur näherungweisen Integration totaler Differentialgleichungen". In: *Zeitschrift für Mathematik und Physik* 46 (1901), pp. 435–453 (see p. 61).

[144] Fehlberg, Erwin. "Low-order classical Runge-Kutta formulas with stepsize control and their application to some heat transfer problems". In: *NASA technical report* July (1969), R–315 (see p. 61).

[145] Courant, R, Friedrichs, K, and Lewy, H. "On the partial difference equations of mathematical physics". In: *IBM Journal* 100.March (1928), pp. 32–74. ISSN: 0018-8646. DOI: 10.1147/rd.112.0215 (see p. 62).

[146] Colgate, Stirling A. and White, Richard H. "The Hydrodynamic Behavior of Supernovae Explosions". In: *The Astrophysical Journal* 143.1 (Mar. 1966), p. 626. ISSN: 0004-637X. DOI: 10.1086/148549 (see p. 64).

[147] Sod, Gary A. "A survey of several finite difference methods for systems of nonlinear hyperbolic conservation laws". In: *Journal of Computational Physics* 27.1 (Apr. 1978), pp. 1–31. ISSN: 00219991. DOI: 10.1016/0021-9991(78)90023-2 (see p. 64).

[148] Fowler, William A and Hoyle, F. "Neutrino Processes and Pair Formation in Massive Stars and Supernovae." In: *The Astrophysical Journal Supplement Series* 9 (Dec. 1964), p. 201. ISSN: 0067-0049. DOI: 10.1086/190103 (see p. 67).

[149] Boshkayev, K. A., Rueda, Jorge a., Zhami, B. A., Kalymova, Zh. A., and Balgymbekov, G. Sh. "Equilibrium structure of white dwarfs at finite temperatures". In: *International Journal of Modern Physics: Conference Series* 41 (Jan. 2016), p. 1660129. ISSN: 2010-1945. DOI: 10.1142/S2010194516601290 (see p. 69).

[150] Eisenstein, Daniel J., Liebert, James, Harris, Hugh C., Kleinman, S. J., Nitta, Atsuko, Silvestri, Nicole, Anderson, Scott a., Barentine, J. C., Brewington, Howard J., Brinkmann, J., Harvanek, Michael, Krzesiński, Jurek, Neilsen Jr., Eric H., Long, Dan, Schneider, Donald P., and Snedden, Stephanie a. "A Catalog of Spectroscopically Confirmed White Dwarfs from the Sloan Digital Sky Survey Data Release 4". In: *The Astrophysical Journal Supplement Series* 167.1 (Nov. 2006), pp. 40–58. ISSN: 0067-0049. DOI: 10.1086/507110 (see p. 70).

[151] Althaus, L. G., Panei, J. a., Romero, a. D., Rohrmann, R. D., Córsico, a. H., García-Berro, E., and Miller Bertolami, M. M. "Evolution and colors of helium-core white dwarf stars with high-metallicity progenitors". In: *Astronomy and Astrophysics* 502.1 (July 2009), pp. 207–216. ISSN: 0004-6361. DOI: 10.1051/0004-6361/200911640 (see p. 73).

[152] Althaus, L. G., García-Berro, E., Isern, J., and Córsico, A. H. "Mass-radius relations for massive white dwarf stars". en. In: *Astronomy and Astrophysics* 441.2 (Oct. 2005), pp. 689–694. ISSN: 0004-6361. DOI: 10.1051/0004-6361:20052996 (see p. 73).

[153] Althaus, L. G., Panei, J. A., Miller Bertolami, M. M., García-Berro, E., Córsico, A. H., Romero, A. D., Kepler, S. O., and Rohrmann, R. D. "NEW EVOLUTIONARY SEQUENCES FOR HOT H-DEFICIENT WHITE DWARFS ON THE BASIS OF A FULL ACCOUNT OF PROGENITOR EVOLUTION". In: *The Astrophysical Journal* 704.2 (Oct. 2009), pp. 1605–1615. ISSN: 0004-637X. DOI: 10.1088/0004-637X/704/2/1605 (see p. 74).

[154] Hamada, T. and Salpeter, E. E. "Models for Zero-Temperature Stars." In: *The Astrophysical Journal* 134 (Nov. 1961), p. 683. ISSN: 0004-637X. DOI: 10.1086/147195 (see p. 74).

[155] Althaus, Leandro G., Córsico, Alejandro H., Isern, Jordi, and García-Berro, Enrique. "Evolutionary and pulsational properties of white dwarf stars". In: *The Astronomy and Astrophysics Review* 18.4 (Oct. 2010), pp. 471–566. ISSN: 0935-4956. DOI: 10.1007/s00159-010-0033-1 (see p. 76).

[156] Holberg, J. B., Oswalt, T. D., and Barstow, M. A. "OBSERVATIONAL CONSTRAINTS ON THE DEGENERATE MASS-RADIUS RELATION". In: *The Astronomical Journal* 143.3 (Mar. 2012), p. 68. ISSN: 0004-6256. DOI: 10.1088/0004-6256/143/3/68 (see p. 76).

[157] Tremblay, P. -E., Gentile-Fusillo, N., Raddi, R., Jordan, S., Besson, C., Gaensicke, B. T., Parsons, S. G., Koester, D., Marsh, T., Bohlin, R., and Kalirai, J. "The Gaia DR1 Mass-Radius Relation for White Dwarfs". In: *e-print arXiv:1611.00629* November (Nov. 2016), pp. 1–13 (see pp. 76, 83).

[158] Bours, M. C P, Marsh, T. R., Parsons, S. G., Copperwheat, C. M., Dhillon, V. S., Littlefair, S. P., Gansicke, B. T., Gianninas, A., and Tremblay, P. E. "Precise parameters for both white dwarfs in the eclipsing binary CSS 41177". In: *Monthly Notices of the Royal Astronomical Society* 438.4 (Mar. 2014), pp. 3399–3408. ISSN: 0035-8711. DOI: 10.1093/mnras/stt2453 (see p. 78).

[159] Parsons, S. G., Marsh, T. R., Copperwheat, C. M., Dhillon, V. S., Littlefair, S. P., Gänsicke, B. T., and Hickman, R. "Precise mass and radius values for the white dwarf and low mass M dwarf in the pre-cataclysmic binary NN Serpentis". In: *Monthly Notices of the Royal Astronomical Society* 402.4 (Mar. 2010), pp. 2591–2608. ISSN: 00358711. DOI: 10.1111/j.1365-2966.2009.16072.x (see p. 78).

[160] Parsons, S. G., Marsh, T. R., Gänsicke, B. T., Dhillon, V. S., Copperwheat, C. M., Littlefair, S. P., Pyrzas, S., Drake, A. J., Koester, D., Schreiber, M. R., and Rebassa-Mansergas, A. "The shortest period detached white dwarf + main-sequence binary". In: *Monthly Notices of the Royal Astronomical Society* 419.1 (2012), pp. 304–313. ISSN: 00358711. DOI: 10.1111/j.1365-2966.2011.19691.x (see p. 78).

[161] Parsons, S. G., Marsh, T. R., Gänsicke, B. T., Rebassa-Mansergas, A., Dhillon, V. S., Littlefair, S. P., Copperwheat, C. M., Hickman, R. D G, Burleigh, M. R., Kerry, P., Koester, D., Nebot Gómez-Morán, A., Pyrzas, S., Savoury, C. D J, Schreiber, M. R., Schmidtobreick, L., Schwope, A. D., Steele, P. R., and Tappert, C. "A precision study of two eclipsing white dwarf plus M dwarf binaries". In: *Monthly Notices of the Royal Astronomical Society* 420.4 (Jan. 2012), pp. 3281–3297. ISSN: 00358711. DOI: 10.1111/j.1365-2966.2011.20251.x (see p. 78).

[162] Parsons, S. G., Hill, C. A., Marsh, T. R., G??nsicke, B. T., Watson, C. A., Steeghs, D., Dhillon, V. S., Littlefair, S. P., Copperwheat, C. M., Schreiber, M. R., and Zorotovic, M. "The crowded magnetosphere of the post-common-envelope binary QS Virginis". In: *Monthly Notices of the Royal Astronomical Society* 458.3

(2016), pp. 2793–2812. ISSN: 13652966. DOI: 10.1093/mnras/stw516 (see p. 78).

[163] O'Brien, M. Sean, Bond, Howard E., and Sion, Edward M. "Hubble Space Telescope Spectroscopy of V471 Tauri: Oversized K Star, Paradoxical White Dwarf". In: *The Astrophysical Journal* 563.2 (2001), pp. 971–986. ISSN: 0004-637X. DOI: 10.1086/324040 (see p. 78).

[164] Koester, D. "Convective Mixing and Accretion in White Dwarfs". In: *Astronomy and Astrophysics* 52 (1976), p. 415 (see pp. 79, 84).

[165] Bergeron, P., Saffer, Rex A., and Liebert, James. "A spectroscopic determination of the mass distribution of DA white dwarfs". In: *The Astrophysical Journal* 394 (July 1992), p. 228. ISSN: 0004-637X. DOI: 10.1086/171575 (see p. 82).

[166] Bergeron, P., Wesemael, F., Dufour, Pierre, Beauchamp, A., Hunter, C., Saffer, Rex A., Gianninas, A., Ruiz, M. T., Limoges, M.-M., Dufour, Patrick, Fontaine, G., and Liebert, James. "A COMPREHENSIVE SPECTROSCOPIC ANALYSIS OF DB WHITE DWARFS". In: *The Astrophysical Journal* 737.1 (Aug. 2011), p. 28. ISSN: 0004-637X. DOI: 10.1088/0004-637X/737/1/28 (see p. 82).

[167] Holberg, J B, Barstow, M A, Bruhweiler, F C, Cruise, A M, and Penny, A J. "Sirius B: A New, More Accurate View". In: *The Astrophysical Journal* 497.2 (Apr. 1998), pp. 935–942. ISSN: 0004-637X. DOI: 10.1086/305489 (see p. 82).

[168] Preval, S. P. and Barstow, M. A. "Understanding the spectrum of the very hot DA white dwarf PG0948+534". In: *e-print arXiv:1610.01677* (Oct. 2016), pp. 1–6 (see p. 83).

[170] Baschek, B., Scholz, M., and Wehrse, R. "The parameters R and Teff in stellar models and observations". In: *Astronomy and Astrophysics* 246 (1991), pp. 374–382. ISSN: 0004-6361 (see p. 84).

[171] Soares, Elvis do Amaral. "Constraining Effective Temperature, Mass and Radius of Hot White Dwarfs". In: *Submitted to Astronomy & Astrophysics* January (Jan. 2017), pp. 1–8. arXiv: 1701.02295 (see p. 84).

[173] Timmes, F. X. and Woosley, S. E. "The conductive propagation of nuclear flames. I - Degenerate C + O and O + NE + MG white dwarfs". In: *The Astrophysical Journal* 396 (Sept. 1992), p. 649. ISSN: 0004-637X. DOI: 10.1086/171746 (see p. 85).

[176] Soares, Elvis do Amaral, Kodama, Takeshi, and De Mello Neto, J. R T. "Delayed Thermalization in Thermonuclear Supernovae Calculations. I. Off-Center Detonations". In: *To be submitted* (2017) (see p. 97).

Other references

[27] Canal, R and Gutierrez, J. "The Possible White Dwarf-Neutron Star Connection". In: 1976. 1997, pp. 49–55. DOI: 10.1007/978-94-011-5542-7_7 (see pp. 9, 12).

[92] Meixner, Josef and Reik, H G. "Thermodynamik der irreversiblen Prozesse". In: *Prinzipien der Thermodynamik und Statistik/Principles of Thermodynamics and Statistics*. Springer, 1959, pp. 413–523 (see p. 25).

[169] Sion, Edward M. "Hot White Dwarfs". In: *White Dwarf Atmospheres and Circumstellar Environments*. Ed. by Hoard, Dr. D. W. Weinheim, Germany: Wiley-VCH Verlag GmbH & Co. KGaA, Sept. 2011. Chap. 1, pp. 1–23. ISBN: 9783527636570. DOI: 10.1002/9783527636570.ch1 (see p. 83).

[174] Hillebrandt, W. and Niemeyer, J. C. "Turbulence and thermonuclear burning". In: *Thermonuclear Supernovae*. Springer, 1997, pp. 337–348 (see p. 85).

[175] Woosley, S. E. "Type I supernovae: Carbon deflagration and detonation". In: *Supernovae*. Springer, 1990, pp. 182–212 (see p. 86).

Book references

[3] Kippenhahn, Rudolf, Weigert, Alfred, and Weiss, Achim. *Stellar Structure and Evolution*. 2nd ed. Astronomy and Astrophysics Library. Springer-Verlag Berlin Heidelberg, 2012, pp. XVIII, 606. ISBN: 9783642302558 (see pp. 1, 5, 70).

[9] Chandrasekhar, Subrahmanyan. *An Introduction to the Study of Stellar Evolution*. 1st ed. Dover Publications, 1957, p. 507. ISBN: 978-0-4-486-60413-8 (see pp. 5, 122, 124).

[16] Shapiro, S. L. and Teukolsky, S. A. *Black Holes, White Dwarfs and Neutron Stars: The Physics of Compact Objects*. 1st ed. Wiley-VCH, 1983, p. 672. ISBN: 978-0471873167 (see pp. 7, 71).

[20] Hoard, D. W. *White Dwarf Atmospheres and Circumstellar Environments*. Weinheim, Germany: John Wiley & Sons Ltd, Sept. 2012. ISBN: 9783527636570. DOI: 10.1002/9783527636570 (see p. 7).

[67] Landau, L D and Lifshitz, E M. *Fluid Mechanics*. 2nd ed. Vol. 6. Course of Theoretical Physics. Butterworth-Heinemann, 1987. ISBN: 978-0750627672 (see pp. 14, 19, 85).

[85] Reichl, Linda E. *A Modern Course in Statistical Physics*. 2nd ed. Wiley-VCH, 1998, p. 842. ISBN: 978-0471595205 (see p. 19).

[86] Mihalas, Dimitri and Mihalas, Barbara Weibel. *Foundations of Radiation Hydrodynamics*. 1st ed. Oxford Studies in Physics. Oxford University Press, 1984, p. 752. ISBN: 9780486409252 (see pp. 19, 20).

[91] Prigogine, Ilya. *Introduction to thermodynamics of irreversible processes*. 3rd ed. New York: Interscience, 1967 (see p. 25).

[93] De Groot, S R and Mazur, P. *Non-Equilibrium thermodynamics*. Republication edition by Dover Publication, New-York, 1984; originally published in North-Holland Pub. Co, 1962 (see pp. 25, 27).

[94] Gyarmati, Istvan and Gyarmati, Eve. *Non-equilibrium thermodynamics*. Springer, 1970 (see p. 25).

[95] Fourier, Joseph. *Theorie analytique de la chaleur*. Chez Firmin Didot, 1822 (see p. 25).

[96] Ohm, Georg Simon. *Die galvanische Kette, mathematisch bearbeitet*. Riemann, 1827 (see p. 25).

[101] Landau, L D and Lifshitz, E M. *Statistical Physics - Part 1*. 3rd ed. Vol. 8. Course of Theoretical Physics. Butterworth-Heinemann, 1980. ISBN: 978-0750633727 (see p. 32).

[102] Weiss, Achim, Hillebrandt, Wolfgang, Thomas, Hans-Christoph, and Ritter, Hans. *Cox and Giuli's Principles of Stellar Structure*. 2nd ed. Advances in Astronomy & Astrophysics. Cambridge Scientific Publishers, 2004 (see pp. 33, 70, 121).

[103] Hansen, Carl J, Kawaler, Steven D, and Trimble, Virginia. *Stellar Interiors: Physical Principles, Structure, and Evolution*. 2nd ed. New York: Springer-Verlag, 1994, pp. XII, 526. ISBN: 978-0-387-20089-7. DOI: 10.1007/978-1-4419-9110-2 (see p. 35).

[104] Huebner, Walter F and Barfield, W David. *Opacity*. Springer, 2014 (see p. 37).

[105] Ziman, John Michael. *Electrons and Phonons: The Theory of Transport Phenomena in Solids*. Oxford: Oxford University Press, 1960. ISBN: 9780198507796 (see pp. 38, 39).

[120] Arnett, David. *Supernovae and Nucleosynthesis*. 1st ed. Princeton Series in Astrophysics. Princeton University Press, 1996. ISBN: 978-0691011479 (see pp. 39, 46).

[130] Iliadis, Christian. *Nuclear Physics of Stars*. 1st ed. Wiley-VCH, 2007. ISBN: 978-3527406029 (see p. 40).

[131] Clayton, Donald D. *Principles of stellar evolution and nucleosynthesis*. New York: McGraw-Hill, 1983, p. 612. ISBN: 978-0226109534 (see p. 40).

[138] Bodenheimer, P, Laughlin, G P, Rozyczka, M, Plewa, T, Yorke, H W, and Yorke, H W. *Numerical Methods in Astrophysics: An Introduction*. Series in Astronomy and Astrophysics. Taylor & Francis, 2006. ISBN: 9780750308830 (see p. 57).

[172] Zeldovich, Ya B, Barenblatt, G I, Librovich, V B, and Makhviladze, G M. *The Mathematical Theory of Combustion and Explosions*. 1st ed. Consultants Bureau, 1985. ISBN: 978-0306109744 (see p. 85).

[177] Press, William H, Teukolsky, Saul A, Vetterling, William T, and Flannery, Brian P. *Numerical Recipes 3rd Edition: The Art of Scientific Computing*. 3rd ed. New York, NY, USA: Cambridge University Press, 2007. ISBN: 0521880688, 9780521880688 (see p. 127).

Appendix A

Semi-degenerate Equation of State

As presented by Cox & Giuli [102] (where many useful tables and others references can be found) the general expressions for electron density, pressure, internal energy can be write, in terms of dimensionless variables $\eta = \mu/k_BT$ and the relativistic parameter $\beta = k_BT/m_ec^2$, in parameterized form

$$n_{\text{ele}} = \frac{8\pi\sqrt{2}}{h^3} m_e^3 c^3 \beta^{3/2} \left[F_{1/2}(\eta,\beta) + \beta F_{3/2}(\eta,\beta)\right] \tag{A.1}$$

$$p_{\text{ele}} = \frac{16\pi\sqrt{2}}{3h^3} m_e^4 c^5 \beta^{5/2} \left[F_{3/2}(\eta,\beta) + (1/2)\beta F_{5/2}(\eta,\beta)\right] \tag{A.2}$$

$$u_{\text{ele}} = \frac{8\pi\sqrt{2}}{h^3} \frac{m_e^4 c^5}{\rho} \beta^{5/2} \left[F_{3/2}(\eta,\beta) + \beta F_{5/2}(\eta,\beta)\right] \tag{A.3}$$

where n_{ele}, p_{ele} and u_{ele} are the electrons number density, pressure and energy density, respectively. The functions F_k are the generalized Fermi-Dirac integrals defined by

$$F_k(\eta,\beta) = \int_0^\infty \frac{x^k (1 + 0.5\beta x)^{1/2}}{\exp\left(-\eta + x\right) + 1}\, \mathrm{d}x \tag{A.4}$$

A.1 Evaluation of the $F_k(\eta,\beta)$

In this section we present expansions for the two cases of, respectively, large degeneracy ($\eta \gg 1$) and small degeneracy ($\eta \leq 0$), both for arbitrary values of β. Next, we present a numerical method sufficient to evaluate the integrals for arbitrary values of β, which are necessary for the case of partial degeneracy (arbitrary η).

A.1.1 Large degeneracy ($\eta \gg 1$), arbitrarily relativistic (arbitrary β)

For $\eta \gg 1$ we may obtain asymptotic expansions for $F_k(\eta, \beta)$ by application of Sommerfeld's Lemma. The following proof is taken from [9].

Lemma A.1.1 (Sommerfeld's Lemma)**.** *If $\varphi(u)$ is an sufficiently regular function and vanishes at $u = 0$, thus the following asymptotic expansion is accurate to terms of order $e^{-u_0} = \Lambda^{-1}$, and it can be written as*

$$\int_0^\infty \frac{\mathrm{d}u}{(1/\Lambda)e^u + 1} \frac{\mathrm{d}\varphi(u)}{\mathrm{d}u} = \varphi(u_0) + 2\left[c_2\varphi''(u_0) + c_4\varphi^{(4)}(u_0) + \dots\right], \tag{A.5}$$

with $u_0 = \log\Lambda$ and c_2, c_4, ..., are numeric coefficients defined by

$$c_\nu = 1 - \frac{1}{2^\nu} + \frac{1}{3^\nu} - \frac{1}{4^\nu} + \dots = (1 - 2^{1-\nu})\zeta(\nu) \tag{A.6}$$

where $\zeta(\nu)$ is the Riemann zeta function.

Proof. We can separate the integral into two regions around u_0, as

$$\int_0^\infty \frac{\mathrm{d}u}{(1/\Lambda)e^u + 1} \frac{\mathrm{d}\varphi(u)}{\mathrm{d}u} = \int_0^{u_0} \frac{\mathrm{d}u}{(1/\Lambda)e^u + 1} \frac{\mathrm{d}\varphi(u)}{\mathrm{d}u} + \int_{u_0}^\infty \frac{\mathrm{d}u}{(1/\Lambda)e^u + 1} \frac{\mathrm{d}\varphi(u)}{\mathrm{d}u}$$

$$= \int_0^{u_0} \frac{\mathrm{d}\varphi(u)}{\mathrm{d}u} + \int_0^{u_0} \left(\frac{1}{(1/\Lambda)e^u + 1} - 1\right) \frac{\mathrm{d}\varphi(u)}{\mathrm{d}u}\mathrm{d}u + \int_{u_0}^\infty \frac{\mathrm{d}u}{(1/\Lambda)e^u + 1} \frac{\mathrm{d}\varphi(u)}{\mathrm{d}u}$$

$$= \varphi(u_0) - \int_0^{u_0} \frac{\mathrm{d}u}{1 + \Lambda e^{-u}} \frac{\mathrm{d}\varphi(u)}{\mathrm{d}u} + \int_{u_0}^\infty \frac{\mathrm{d}u}{(1/\Lambda)e^u + 1} \frac{\mathrm{d}\varphi(u)}{\mathrm{d}u}. \tag{A.7}$$

Defining a new variable for each one integral, $u = u_0(1 - t)$ for the first one, and $u = u_0(1 + t)$ for the other one, we have

$$\int_0^\infty \frac{\mathrm{d}u}{(1/\Lambda)e^u + 1} \frac{\mathrm{d}\varphi(u)}{\mathrm{d}u} = \varphi(u_0) - u_0 \int_0^1 \frac{\varphi'[u_0(1-t)]}{1 + e^{u_0 t}}\,\mathrm{d}t + u_0 \int_0^\infty \frac{\varphi'[u_0(1+t)]}{1 + e^{u_0 t}}\,\mathrm{d}t. \tag{A.8}$$

Extending the limit of the first integral to infinity, we add an error term of order e^{-u_0}, which is beyond our accuracy. Then

$$\int_0^\infty \frac{\mathrm{d}u}{(1/\Lambda)e^u + 1} \frac{\mathrm{d}\varphi(u)}{\mathrm{d}u} \simeq \varphi(u_0) + u_0 \int_0^\infty \frac{\varphi'[u_0(1+t)] - \varphi'[u_0(1-t)]}{1 + e^{u_0 t}}\,\mathrm{d}t, \tag{A.9}$$

and expanding φ' around u_0 in the form

$$\varphi'[u_0(1+t)] = \varphi'(u_0) + \varphi''(u_0)(u_0 t) + \frac{1}{2!}\varphi'''(u_0).(u_0 t)^2 + \dots, \tag{A.10}$$

and

$$\varphi'[u_0(1-t)] = \varphi'(u_0) + \varphi''(u_0)(-u_0 t) + \frac{1}{2!}\varphi'''(u_0)(-u_0 t)^2 + \dots, \tag{A.11}$$

we can write the (A.9) as

$$\int_0^\infty \frac{\mathrm{d}u}{(1/\Lambda)e^u + 1}\frac{d\varphi(u)}{\mathrm{d}u} \simeq \varphi(u_0) + 2\sum_{\nu=2,4,6,\dots} \frac{u_0^\nu \varphi^{(\nu)}(u_0)}{(\nu-1)!}\int_0^\infty \frac{t^{\nu-1}}{1+e^{u_0 t}}\,\mathrm{d}t, \tag{A.12}$$

where the odd derivative terms cancel themselves. In other hand, we have

$$\int_0^\infty \frac{t^{\nu-1}}{1+e^{u_0 t}}\,\mathrm{d}t = \int_0^\infty t^{\nu-1}(e^{-u_0 t} - e^{-2u_0 t} + e^{-3u_0 t} - \dots)\,\mathrm{d}t, \tag{A.13}$$

with each term independently resulting in

$$(-1)^{n-1}\int_0^\infty t^{\nu-1}e^{-nu_0 t}\,\mathrm{d}t = \frac{(-1)^{n-1}(\nu-1)!}{u_0^\nu n^\nu}, \tag{A.14}$$

and we get

$$\int_0^\infty \frac{t^{\nu-1}}{1+e^{u_0 t}}\,\mathrm{d}t = \frac{(\nu-1)!}{u_0^\nu}\left(1 - \frac{1}{2^\nu} + \frac{1}{3^\nu} - \frac{1}{4^\nu} + \dots\right). \tag{A.15}$$

Defining $c_\nu = \left(1 - \frac{1}{2^\nu} + \frac{1}{3^\nu} - \frac{1}{4^\nu} + \dots\right)$[1], then we can write

$$\int_0^\infty \frac{\mathrm{d}u}{(1/\Lambda)e^u + 1}\frac{d\varphi(u)}{\mathrm{d}u} = \varphi(u_0) + 2\left[c_2\varphi''(u_0) + c_4\varphi^{(4)}(u_0) + \dots\right], \tag{A.16}$$

which proves the lemma. □

We express the asymptotic formulae for $F_k(\eta,\beta)$ in terms of η and $x = p_0/m_e c$, remembering that p_0 is the momentum value for which the occupation number $q = 1/2$. The corresponding value of kinetic energy is $\epsilon_0/m_e c^2 = \eta\beta$, so that

$$1 + x^2 = (1+\eta\beta)^2 \tag{A.17}$$

from the relativistic dispersion relation. In this context ($\eta \gg 1$), x may be regarded as a relativity parameter: $x \ll 1$ implies the N.R. regime, and $x \gg 1$ the E.R. regime. For given x, the value of β is determined by (A.17).

[1] We may note that

$$c_2 = \frac{\pi^2}{12}, \quad c_4 = \frac{7\pi^4}{720}, \quad c_6 = \frac{31\pi^6}{30240}, \dots$$

The relevant asymptotic expansions for n_e, P_e, and u_e for large degeneracy ($\eta \gg 1$) and x arbitrary, with the existence of $e^{\pm}$ pairs neglected, are then

$$n_{\rm ele} = \frac{8\pi m_e^3 c^3}{3h^3} x^3 \left\{ 1 + 2 \left[c_2 \frac{1}{\eta^2} \frac{3(1+2x^2)(\sqrt{1+x^2}-1)^2}{x^4} + c_4 \frac{1}{\eta^4} \frac{9(\sqrt{1+x^2}-1)^4}{x^8} \right.\right.$$
$$\left.\left. + \; c_6 \frac{1}{\eta^6} \frac{45(7+6x^2)(\sqrt{1+x^2}-1)^6}{x^{12}} + \ldots \right] \right\}, \tag{A.18}$$

$$p_{\rm ele} = \frac{\pi m_e^4 c^5}{3h^3} f(x) \left\{ 1 + 2 \left[c_2 \frac{1}{\eta^2} \frac{24x\sqrt{1+x^2}(\sqrt{1+x^2}-1)^2}{f(x)} \right.\right.$$
$$+ c_4 \frac{1}{\eta^4} \frac{24(2x^2-1)\sqrt{1+x^2}(\sqrt{1+x^2}-1)^4}{x^3 f(x)}$$
$$\left.\left. - \; c_6 \frac{1}{\eta^6} \frac{360\sqrt{1+x^2}(\sqrt{1+x^2}-1)^6}{x^7 f(x)} + \ldots \right] \right\} \tag{A.19}$$

$$u_{\rm ele} = \frac{\pi m_e^4 c^5}{3h^3} g(x) \left\{ 1 + 2 \left[c_2 \frac{1}{\eta^2} \frac{24\left(-1+\sqrt{1+x^2}+x^2(-2+3\sqrt{1+x^2})\right)(\sqrt{1+x^2}-1)^2}{x g(x)} \right.\right.$$
$$+ c_4 \frac{1}{\eta^4} \frac{72\left(-1+\sqrt{1+x^2}+x^2\sqrt{1+x^2}(-1+2x^2)\right)(\sqrt{1+x^2}-1)^4}{x^5 g(x)}$$
$$\left.\left. + \; c_6 \frac{1}{\eta^6} \frac{360\left(x^2(-6+\sqrt{1+x^2})+7(-1+\sqrt{1+x^2})\right)(\sqrt{1+x^2}-1)^6}{x^9 g(x)} + \ldots \right] \right\} \tag{A.20}$$

where

$$f(x) \equiv x(2x^2-3)\sqrt{1+x^2} + 3\sinh^{-1} x \tag{A.21}$$

and

$$g(x) \equiv 8x^3(\sqrt{1+x^2}-1) - f(x) \tag{A.22}$$

are the functions defined by Chandrasekhar [9, Ch. X].

The phase of complete degeneracy can be obtained from these general expan-

sions by taking $\eta \to +\infty$. So we have

$$n_{\rm ele}(\infty,0) = \frac{8\pi m_e^3 c^3}{3h^3} x^3 \tag{A.23}$$

$$p_{\rm ele}(\infty,0) = \frac{\pi m_e^4 c^5}{3h^3} f(x) \tag{A.24}$$

$$u_{\rm ele}(\infty,0) = \frac{\pi m_e^4 c^5}{3h^3} g(x), \tag{A.25}$$

and their mutual relations are simplified as

$$\frac{p_{\rm ele}}{n_{\rm ele} k_B T} = \frac{1}{8}\frac{f(x)}{\beta x^3} = \frac{\eta}{8}\frac{f(x)}{x^3\left(\sqrt{1+x^2}-1\right)} = \begin{cases} (2/5)\eta & x \to 0 \text{ (N.R.)} \\ (1/4)\eta & x \to \infty \text{ (E.R.)} \end{cases}. \tag{A.26}$$

and

$$\frac{p_{\rm ele}}{u_{\rm ele}} = \frac{f(x)}{g(x)} = \begin{cases} (2/3) & x \to 0 \text{ (N.R.)} \\ (1/3) & x \to \infty \text{ (E.R.)} \end{cases}.$$

A.1.2 Small degeneracy ($\eta \leq 0$), arbitrarily relativistic (arbitrary β)

The generalized Fermi-Dirac functions may be written as

$$F_k(\eta,\beta) = e^{\eta}\int_0^{\infty} \frac{x^k e^{-x}(1+0.5\beta x)^{1/2}}{1+e^{\eta-x}} \mathrm{d}x. \tag{A.27}$$

For $\eta < 0$, $e^{\eta-x} < 1$ for all $x \geq 0$, and the factor $(1+e^{\eta-x})^{-1}$ can be expanded in a convergent power series in $e^{\eta-x}$. Expanding and integrating term by term, we obtain

$$F_k(\eta,\beta) = e^{\eta}\sum_{r=0}^{\infty}(-1)^r e^{r\eta}\int_0^{\infty} x^k e^{-(r+1)x}(1+(1/2)\beta x)^{1/2}\mathrm{d}x, \tag{A.28}$$

which also converges at $\eta = 0$. With the change of variable

$$\cosh\theta \equiv 1+\beta x, \tag{A.29}$$

the integral

$$F_k(\eta,\beta) = e^{\eta+\frac{1}{\beta}}\frac{1}{\sqrt{2}}\frac{1}{\beta^{k+1}}\sum_{r=0}^{\infty}(-1)^r e^{r\left(\eta+\frac{1}{\beta}\right)}\int_0^{\infty}(\cosh\theta-1)^{k-\frac{1}{2}}e^{-(r+1)\cosh\theta/\beta}\sinh\theta\ \mathrm{d}\theta, \tag{A.30}$$

can be associate with the Bessel functions of the type $K_\nu(z)$, expressed in terms of

the integrals

$$K_\nu(z) = \int_0^\infty e^{-z\cosh t}\cosh \nu t \; \mathrm{d}t, \tag{A.31}$$

making use of the recursion relations

$$K_{\nu-1}(z) - K_{\nu+1}(z) = -\frac{2\nu}{z}K_\nu(z). \tag{A.32}$$

Then, we have for $\eta \leq 0$ and arbitrary β, in the case $e^\pm$ pairs are being neglected,

$$n_{\mathrm{ele}} = \frac{8\pi m_e^3 c^3}{h^3}\beta e^{\eta+\frac{1}{\beta}} \sum_{r=0}^{\infty}(-1)^r e^{r\left(\eta+\frac{1}{\beta}\right)} \frac{1}{r+1} K_2\left(\frac{r+1}{\beta}\right), \tag{A.33}$$

$$p_{\mathrm{ele}} = \frac{8\pi m_e^4 c^5}{h^3}\beta^2 e^{\eta+\frac{1}{\beta}} \sum_{r=0}^{\infty}(-1)^r e^{r\left(\eta+\frac{1}{\beta}\right)} \frac{1}{(r+1)^2} K_2\left(\frac{r+1}{\beta}\right), \tag{A.34}$$

$$\begin{aligned} u_{\mathrm{ele}} =& \frac{8\pi m_e^4 c^5}{h^3}\beta e^{\eta+\frac{1}{\beta}} \sum_{r=0}^{\infty}(-1)^r e^{r\left(\eta+\frac{1}{\beta}\right)} \\ & \cdot \left\{ \frac{1}{r+1} K_1\left(\frac{r+1}{\beta}\right) + \left[\frac{3\beta}{(r+1)^2} - \frac{1}{r+1}\right] K_2\left(\frac{r+1}{\beta}\right) \right\}. \end{aligned} \tag{A.35}$$

The completely non-degenerate case for arbitrary β is obtained from the general expansions for $\eta \leq 0$ by taking $\eta \to -\infty$, retaining only the first terms of the expansions. Thus, we have

$$n_{\mathrm{ele}} = \frac{8\pi m_e^3 c^3}{h^3}\beta e^{\eta+\frac{1}{\beta}} K_2(1/\beta), \tag{A.36}$$

$$\begin{aligned} p_{\mathrm{ele}} &= \frac{8\pi m_e^4 c^5}{h^3}\beta^2 e^{\eta+\frac{1}{\beta}} K_2(1/\beta) \\ &= n_e k_B T, \end{aligned} \tag{A.37}$$

$$\begin{aligned} u_{\mathrm{ele}} &= \frac{8\pi m_e^4 c^5}{h^3}\beta e^{\eta+\frac{1}{\beta}} \left[K_1(1/\beta) + (3\beta - 1)K_2(1/\beta)\right] \\ &= P_e \left[\frac{K_1(1/\beta)}{\beta K_2(1/\beta)} + 3 - \frac{1}{\beta}\right]. \end{aligned} \tag{A.38}$$

Therefore, the perfect gas law holds in the case of a completely non-degenerate gas composed of non-interacting (or weakly interacting) particles, for any relativistic regime.

In the completely non-degenerate case ($\eta \to -\infty$), for the non-relativistic regime ($\beta \to 0$) and relativistic regime ($\beta \to \infty$) we can make use of the asymptotic expansions for $K_\nu(z)$.

A.1.3 Arbitrarily degenerate and arbitrarily relativistic

In this case, it is reasonable to compute the generalized Fermi-Dirac functions (**??**) by direct integration, using change of variables to obtain a rapidly convergent quadrature. We use the approach from Numerical Recipes [177].

They do the usual transformation $x = \exp(t - e^{-t})$, which maneuver the singularity at $x = 0$ and the exponential decay to large x. For $\eta \gtrsim 15$, the integral can be split into two regions, $[0, \eta]$ and $[\eta, \eta + 60]$, with the contribution beyond $\eta + 60$ being neglected. Each of these integrals being calculated with trapezoidal integration rules.

A.2 Helmholtz Equation of State

Direct evaluation of the electron-positron physics in the EOS is usually accurate enough and thermodynamically consistent, but it is often overly time consuming within the context of a two- or three-dimensional model. Tabular equations of state for the electron-positron plasma are usually efficient enough for multidimensional models, but bring about their own set of difficulties with regard to accuracy and consistency. These difficulties include the need for accurate interpolations, the need for a temperature-density grid which is dense enough to provide sufficient resolution of the thermodynamic variables, and the need for the interpolated values to be thermodynamically consistent with each other (i.e., satisfy the Maxwell relations). In many circumstances the number of points in the temperature-density grid can always be made large enough to keep the accuracy and level of thermodynamic inconsistency at an acceptable level, although in some cases the memory or cache requirement

In this section we present the idea from Timmes & Swesty [140] for an electron-positron equation of state based on table interpolation of the Helmholtz free energy.

A.2.1 Quintic Hermite Interpolation

A quintic Hermite interpolator is a numeric function that is piecewise-defined by polynomial functions where each piece is a quintic-degree polynomial specified in Hermite form, i.e., by its values and ist first and second derivatives at the end points of the corresponding domain interval. These piecewise numeric functions are sometimes called splines.

Hermite splines are typically used for interpolation of numeric data specified at some values $x_1, x_2, \ldots, x_n$, to obtain a smooth continuous function. The data should consist of the desired function value and derivatives at each x_i. The Hermite formula

is applied to each interval interval $[x_i, x_{i+1}]$ independently, being defined by

$$H_5(x) = A + Bx + Cx^2 + Dx^3, \tag{A.39}$$

with the following constraints of the original data $f(x_i)$ and its derivatives at the borders of the interval

$$\begin{aligned} H_5(x_i) &= f_i, \quad H_5(x_{i+1}) = f_{i+1}, \\ H_5'(x_i) &= \left.\frac{\mathrm{d}f}{\mathrm{d}x}\right|_i, \quad H_5'(x_{i+1}) = \left.\frac{\mathrm{d}f}{\mathrm{d}x}\right|_{i+1}, \\ H_5''(x_i) &= \left.\frac{\mathrm{d}^2f}{\mathrm{d}x^2}\right|_i, \quad H_5''(x_{i+1}) = \left.\frac{\mathrm{d}^2f}{\mathrm{d}x^2}\right|_{i+1}, \end{aligned} \tag{A.40}$$

necessary to determine the coefficients A, B, C and D. The three polynomials resulting of these constraints are the quintic Hermite basis functions

$$h_0(z) = 1 - 10z^3 + 15z^4 - 6z^5, \tag{A.41}$$

$$h_1(z) = z - 6z^3 + 8z^4 - 3z^5, \tag{A.42}$$

$$h_2(z) = \tfrac{1}{2}(z^2 - 3z^3 + 3z^4 - z^5), \tag{A.43}$$

and the interpolating quintic Hermite polynomial is

$$\begin{aligned} H_5(x) =& f_i h_0(\widetilde{x}) + f_{i+1} h_0(1-\widetilde{x}) + \left.\frac{\mathrm{d}f}{\mathrm{d}x}\right|_i (x_{i+1} - x_i) h_1(\widetilde{x}) - \left.\frac{\mathrm{d}f}{\mathrm{d}x}\right|_{i+1} (x_{i+1} - x_i) h_1(1-\widetilde{x}) \\ &+ \left.\frac{\mathrm{d}^2f}{\mathrm{d}x^2}\right|_i (x_{i+1} - x_i)^2 h_2(\widetilde{x}) + \left.\frac{\mathrm{d}^2f}{\mathrm{d}x^2}\right|_{i+1} (x_{i+1} - x_i)^2 h_2(1-\widetilde{x}). \end{aligned} \tag{A.44}$$

where

$$\widetilde{x} = \frac{x - x_i}{x_{i+1} - x_i}, \tag{A.45}$$

To use the quintic Hermite interpolant one must tabulate the function $f(x)$ and its first $\mathrm{d}f/\mathrm{d}x$ and second $\mathrm{d}^2f/\mathrm{d}x^2$ derivatives at the grid points. In return for this investment, the values of the function and its first and second derivative are reproduced exactly at the grid points. In addition, the values of the function and the derivatives change continuously as the interpolating point moves from one grid cell to the next. Note the derivative of the Hermite interpolant function is given by the derivative of the basis functions in (A.44).

A.2.2 Bi-quintic Hermite Interpolation

The one-dimensional quintic polynomial can be extended to two dimensions by interpolating each of the parcel of (A.44) in the second dimension.

$$
\begin{aligned}
&H_5(x,y) = \\
&f_{i,j}h_0(\widetilde{x})h_0(\widetilde{y}) + f_{i+1,j}h_0(1-\widetilde{x})h_0(\widetilde{y}) + f_{i,j+1}h_0(\widetilde{x})h_0(1-\widetilde{y}) + f_{i+1,j+1}h_0(1-\widetilde{x})h_0(1-\widetilde{y}) \\
&+ \left.\frac{\partial f}{\partial x}\right|_{i,j}(x_{i+1}-x_i)h_1(\widetilde{x})h_0(\widetilde{y}) - \left.\frac{\partial f}{\partial x}\right|_{i+1,j}(x_{i+1}-x_i)h_1(1-\widetilde{x})h_0(\widetilde{y}) \\
&+ \left.\frac{\partial f}{\partial x}\right|_{i,j+1}(x_{i+1}-x_i)h_1(\widetilde{x})h_0(1-\widetilde{y}) - \left.\frac{\partial f}{\partial x}\right|_{i+1,j+1}(x_{i+1}-x_i)h_1(1-\widetilde{x})h_0(1-\widetilde{y}) \\
&+ \left.\frac{\partial f}{\partial y}\right|_{i,j}(y_{i+1}-y_i)h_0(\widetilde{x})h_1(\widetilde{y}) - \left.\frac{\partial f}{\partial y}\right|_{i+1,j}(y_{i+1}-y_i)h_0(1-\widetilde{x})h_1(\widetilde{y}) \\
&+ \left.\frac{\partial f}{\partial y}\right|_{i,j+1}(y_{i+1}-y_i)h_0(\widetilde{x})h_1(1-\widetilde{y}) - \left.\frac{\partial f}{\partial y}\right|_{i+1,j+1}(y_{i+1}-y_i)h_0(1-\widetilde{x})h_1(1-\widetilde{y}) \\
&+ \left.\frac{\partial^2 f}{\partial x\partial y}\right|_{i,j}(x_{i+1}-x_i)(y_{i+1}-y_i)h_1(\widetilde{x})h_1(\widetilde{y}) - \left.\frac{\partial^2 f}{\partial x\partial y}\right|_{i+1,j}(x_{i+1}-x_i)(y_{i+1}-y_i)h_1(1-\widetilde{x})h_1(\widetilde{y}) \\
&- \left.\frac{\partial^2 f}{\partial x\partial y}\right|_{i,j+1}(x_{i+1}-x_i)(y_{i+1}-y_i)h_1(\widetilde{x})h_1(1-\widetilde{y}) \\
&+ \left.\frac{\partial^2 f}{\partial x\partial y}\right|_{i+1,j+1}(x_{i+1}-x_i)(y_{i+1}-y_i)h_1(1-\widetilde{x})h_1(1-\widetilde{y}) \\
&+ \left.\frac{\partial^2 f}{\partial x^2}\right|_{i,j}(x_{i+1}-x_i)^2h_2(\widetilde{x})h_0(\widetilde{y}) + \left.\frac{\partial^2 f}{\partial x^2}\right|_{i+1,j}(x_{i+1}-x_i)^2h_2(1-\widetilde{x})h_0(\widetilde{y}) \\
&+ \left.\frac{\partial^2 f}{\partial x^2}\right|_{i,j+1}(x_{i+1}-x_i)^2h_2(\widetilde{x})h_0(1-\widetilde{y}) + \left.\frac{\partial^2 f}{\partial x^2}\right|_{i+1,j+1}(x_{i+1}-x_i)^2h_2(1-\widetilde{x})h_0(1-\widetilde{y}) \\
&+ \left.\frac{\partial^2 f}{\partial y^2}\right|_{i,j}(y_{i+1}-y_i)^2h_0(\widetilde{x})h_2(\widetilde{y}) + \left.\frac{\partial^2 f}{\partial y^2}\right|_{i+1,j}(y_{i+1}-y_i)^2h_0(1-\widetilde{x})h_2(\widetilde{y}) \\
&+ \left.\frac{\partial^2 f}{\partial y^2}\right|_{i,j+1}(y_{i+1}-y_i)^2h_0(\widetilde{x})h_2(1-\widetilde{y}) + \left.\frac{\partial^2 f}{\partial y^2}\right|_{i+1,j+1}(y_{i+1}-y_i)^2h_0(1-\widetilde{x})h_2(1-\widetilde{y}) \\
&+ \left.\frac{\partial^3 f}{\partial x^2\partial y}\right|_{i,j}(x_{i+1}-x_i)^2(y_{i+1}-y_i)h_2(\widetilde{x})h_1(\widetilde{y}) \\
&+ \left.\frac{\partial^3 f}{\partial x^2\partial y}\right|_{i+1,j}(x_{i+1}-x_i)^2(y_{i+1}-y_i)h_2(1-\widetilde{x})h_1(\widetilde{y}) \\
&- \left.\frac{\partial^3 f}{\partial x^2\partial y}\right|_{i,j+1}(x_{i+1}-x_i)^2(y_{i+1}-y_i)h_2(\widetilde{x})h_1(1-\widetilde{y}) \\
&- \left.\frac{\partial^3 f}{\partial x^2\partial y}\right|_{i+1,j+1}(x_{i+1}-x_i)^2(y_{i+1}-y_i)h_2(1-\widetilde{x})h_1(1-\widetilde{y}) \\
&+ \left.\frac{\partial^3 f}{\partial x\partial y^2}\right|_{i,j}(x_{i+1}-x_i)(y_{i+1}-y_i)^2h_1(\widetilde{x})h_2(\widetilde{y})
\end{aligned}
$$

$$
\begin{aligned}
&- \left.\frac{\partial^3 f}{\partial x \partial y^2}\right|_{i+1,j} (x_{i+1}-x_i)(y_{i+1}-y_i)^2 h_1(1-\widetilde{x})h_2(\widetilde{y}) \\
&+ \left.\frac{\partial^3 f}{\partial x \partial y^2}\right|_{i,j+1} (x_{i+1}-x_i)(y_{i+1}-y_i)^2 h_1(\widetilde{x})h_2(1-\widetilde{y}) \\
&- \left.\frac{\partial^3 f}{\partial x \partial y^2}\right|_{i+1,j+1} (x_{i+1}-x_i)(y_{i+1}-y_i)^2 h_1(1-\widetilde{x})h_2(1-\widetilde{y}) \\
&+ \left.\frac{\partial^4 f}{\partial x^2 \partial y^2}\right|_{i,j} (x_{i+1}-x_i)^2(y_{i+1}-y_i)^2 h_2(\widetilde{x})h_2(\widetilde{y}) \\
&+ \left.\frac{\partial^4 f}{\partial x^2 \partial y^2}\right|_{i+1,j} (x_{i+1}-x_i)^2(y_{i+1}-y_i)^2 h_2(1-\widetilde{x})h_2(\widetilde{y}) \\
&+ \left.\frac{\partial^4 f}{\partial x^2 \partial y^2}\right|_{i,j+1} (x_{i+1}-x_i)^2(y_{i+1}-y_i)^2 h_2(\widetilde{x})h_2(1-\widetilde{y}) \\
&+ \left.\frac{\partial^4 f}{\partial x^2 \partial y^2}\right|_{i+1,j+1} (x_{i+1}-x_i)^2(y_{i+1}-y_i)^2 h_2(1-\widetilde{x})h_2(1-\widetilde{y})
\end{aligned} \tag{A.46}
$$

where

$$
\widetilde{x} = \frac{x - x_i}{x_{i+1} - x_i} \quad \text{and} \quad \widetilde{y} = \frac{y - y_i}{y_{i+1} - y_i}. \tag{A.47}
$$

A.2.3 Helmholtz free energy interpolation

To use the biquintic Hermite interpolant for a Helmholtz free energy based equation of state, one must tabulate the Helmholtz free energy per unit mass f and its eight partial derivatives $\partial f/\partial T$, $\partial f/\partial \rho$, $\partial^2 f/\partial \rho \partial T$, $\partial^2 f/\partial \rho^2$, $\partial^2 f/\partial T^2$, $\partial^3 f/\partial \rho^2 \partial T$, $\partial^3 f/\partial \rho \partial T^2$, $\partial^4 f/\partial \rho^2 \partial T^2$, as a function of density and temperature.

In return for this nontrivial investment, the values of the function, first partial derivatives, and second partial derivatives are reproduced exactly at the grid points, changing continuously as the interpolating point moves from one grid cell to the next. With (A.46) as the interpolating function, the Helmholtz free energy is given by a biquintic polynomial. The pressure, entropy, and internal energy are given by a biquartic polynomials, and the derivatives of the pressure, entropy, and internal energy are given by bicubic polynomials. Note the partial derivatives of biquintic interpolant are determined by the derivatives of the three basis functions given by (A.43).

Fortunately, five of the eight partial derivatives needed to use the biquintic interpolant can usually be formed from the EoS based upon the free energy relation

$$
f = u - Ts \tag{A.48}
$$

where u is the internal energy per unit mass and s the entropy per unit mass. From

the first law of thermodynamics, the total differential of this free energy is

$$df = -sdT + \frac{p}{\rho^2}d\rho, \tag{A.49}$$

and its partial derivatives are

$$\begin{aligned}
\left.\frac{\partial f}{\partial T}\right|_\rho &= -s, \quad \left.\frac{\partial f}{\partial \rho}\right|_T = \frac{p}{\rho^2} \\
\left.\frac{\partial^2 f}{\partial T^2}\right|_\rho &= -\left.\frac{\partial s}{\partial T}\right|_\rho, \quad \left.\frac{\partial^2 f}{\partial \rho^2}\right|_T = \frac{1}{\rho^2}\left.\frac{\partial p}{\partial \rho}\right|_T - \frac{2p}{\rho^3} \\
\frac{\partial^2 f}{\partial T \partial \rho} &= -\left.\frac{\partial s}{\partial \rho}\right|_T = \frac{\partial^2 f}{\partial \rho \partial T} = \frac{1}{\rho^2}\left.\frac{\partial p}{\partial T}\right|_\rho .
\end{aligned} \tag{A.50}$$

The third and fourth partial derivative are not available directly from the thermodynamic relations. However, these third and fourth partial derivatives can be obtained from techniques which produce accurate numerical derivatives. We use the centered finite difference method, so that

$$\begin{aligned}
\frac{\partial^3 f}{\partial T^2 \partial \rho} = \{&[f(\rho+\delta\rho, T-\delta T) - 2f(\rho+\delta\rho, T) + f(\rho+\delta\rho, T+\delta T)] \\
-&[f(\rho-\delta\rho, T-\delta T) - 2f(\rho-\delta\rho, T) + f(\rho-\delta\rho, T+\delta T)]\} / (2\delta\rho\delta T^2) + \mathcal{O}(\delta\rho^2\delta T^2)
\end{aligned} \tag{A.51}$$

$$\begin{aligned}
\frac{\partial^3 f}{\partial \rho^2 \partial T} = \{&[f(\rho-\delta\rho, T+\delta T - 2f(\rho, T+\delta T) + f(\rho+\delta\rho, T+\delta T)] \\
-&[f(\rho-\delta\rho, T-\delta T) - 2f(\rho, T-\delta T) + f(\rho+\delta\rho, T-\delta T)]\} / (2\delta T\delta\rho^2) + \mathcal{O}(\delta\rho^2\delta T^2)
\end{aligned} \tag{A.52}$$

$$\begin{aligned}
\frac{\partial^4 f}{\partial \rho^2 \partial T^2} = \{&[f(\rho-\delta\rho, T-\delta T) - 2f(\rho-\delta\rho, T) + f(\rho-\delta\rho, T+\delta T)] \\
&-2[f(\rho, T-\delta T) - 2f(\rho, T) + f(\rho, T+\delta T)] \\
+&[f(\rho+\delta\rho, T-\delta T) - 2f(\rho+\delta\rho, T) + f(\rho+\delta\rho, T+\delta T)]\} / (\delta T^2\delta\rho^2) + \mathcal{O}(\delta\rho^3\delta T^2)
\end{aligned} \tag{A.53}$$

which returns the exact derivatives when $\delta\rho \to 0$ and $\delta T \to 0$. The omission of these three terms should allow the second partial derivatives of the interpolant to exhibit spurious oscillations as one moves through the center of a cell, mainly where pair-production dominate the thermodynamic quantities.

The table generated for the EoS interpolation stores the electron-positron Helmholtz

free energy and the needed eight partial derivatives to 16 digits accuracy. The limits of the table were chosen to be $\log(\rho/\mu_e) = [-6; 11]$ and $\log T = [4; 11]$ in cgs units. This range of 17 orders of magnitude in density and 7 orders of magnitude in temperature is large enough to our purpose of thermonuclear supernovae calculations.

The other contributions to the EoS from photons or ions are not included in the table. Of course, these components are very simple - a black-body radiation and an ideal gas, respectively - and we do not need read-off a table to do simple calculations like these.

A.3 Thermodynamic Quantities

Once a table of the Helmholtz free energy and eight of its partial derivatives has been constructed, the thermodynamic quantities and their derivatives are given by

$$\begin{aligned} p &= \rho^2 \frac{\partial f}{\partial \rho}, \quad \left.\frac{\partial p}{\partial T}\right|_\rho = \rho^2 \frac{\partial^2 f}{\partial \rho \partial T}, \quad \left.\frac{\partial p}{\partial \rho}\right|_T = \rho^2 \frac{\partial^2 f}{\partial \rho^2} + 2\rho \frac{\partial f}{\partial \rho}, \\ s &= -\frac{\partial f}{\partial T}, \quad \left.\frac{\partial s}{\partial T}\right|_\rho = -\frac{\partial^2 f}{\partial T^2}, \quad \left.\frac{\partial s}{\partial \rho}\right|_T = -\frac{\partial^2 f}{\partial \rho \partial T}, \\ u &= f + Ts, \quad \left.\frac{\partial u}{\partial T}\right|_\rho = T \frac{\partial s}{\partial T}, \quad \left.\frac{\partial u}{\partial \rho}\right|_T = \frac{\partial f}{\partial \rho} + T \frac{\partial s}{\partial \rho}. \end{aligned} \tag{A.54}$$

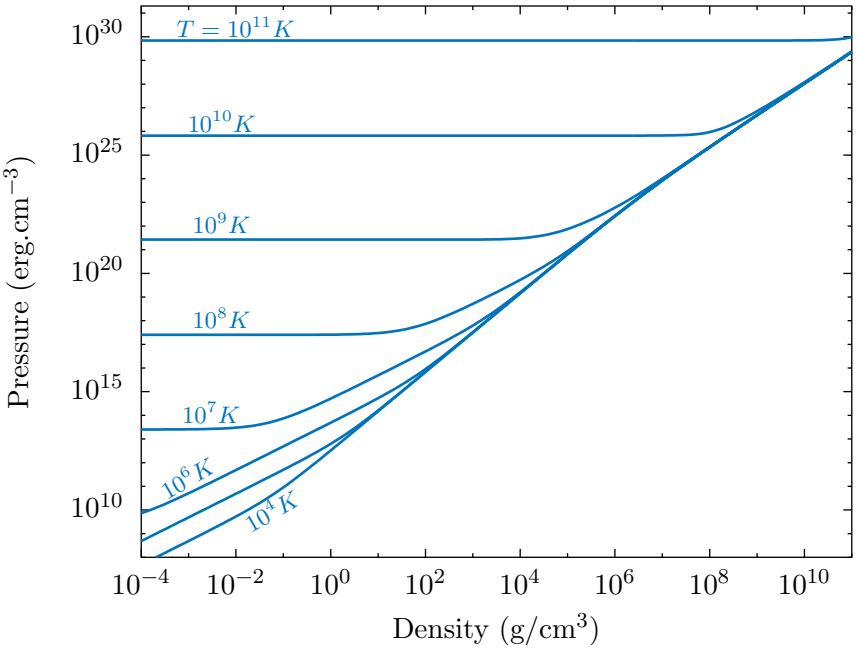

Figure A.1: Pressure as a function of density for different temperatures and a pure ^{12}C composition.

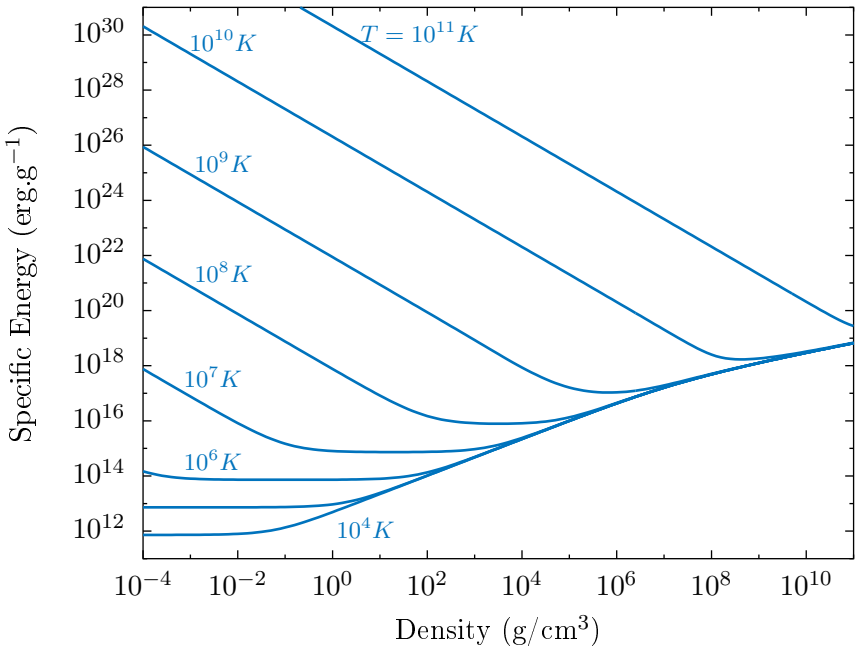

Figure A.2: Internal energy per unit mass as a function of density for different temperatures and a pure ^{12}C composition.

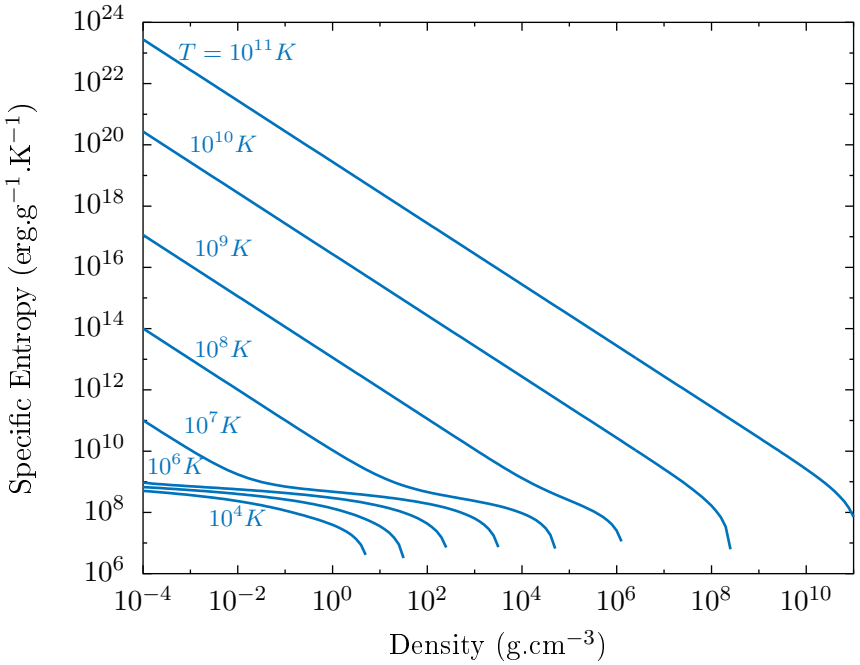

Figure A.3: Entropy per unit mass as a function of density for different temperatures and a pure ^{12}C composition.

As suggest by Timmes *et al.* [139] we investigate if the thermodynamic relations

$$P = \rho^2 \frac{\partial u}{\partial \rho} + T \frac{\partial p}{\partial T} \tag{A.55}$$

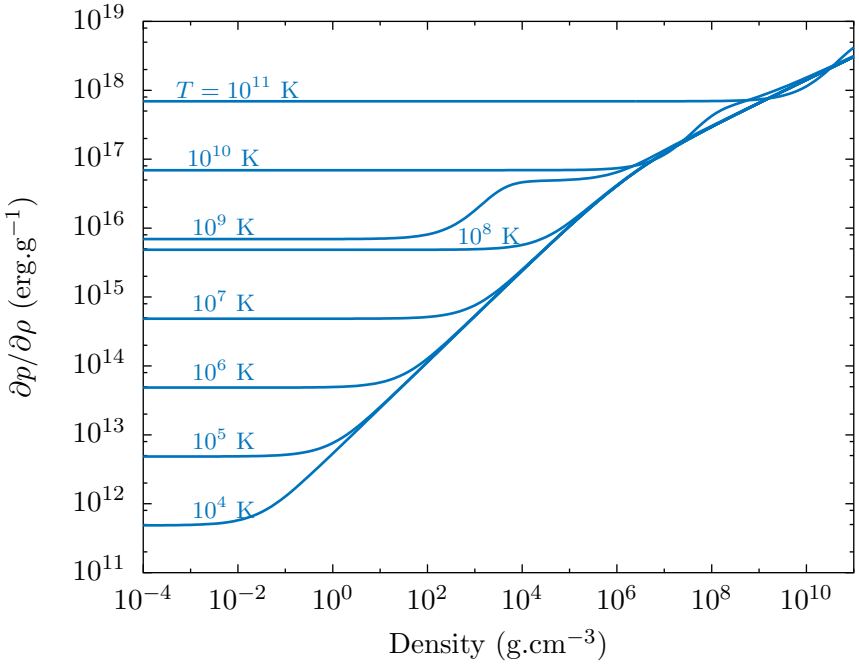

Figure A.4: Partial derivative of the pressure with respect to the density for different constant values of temperature.

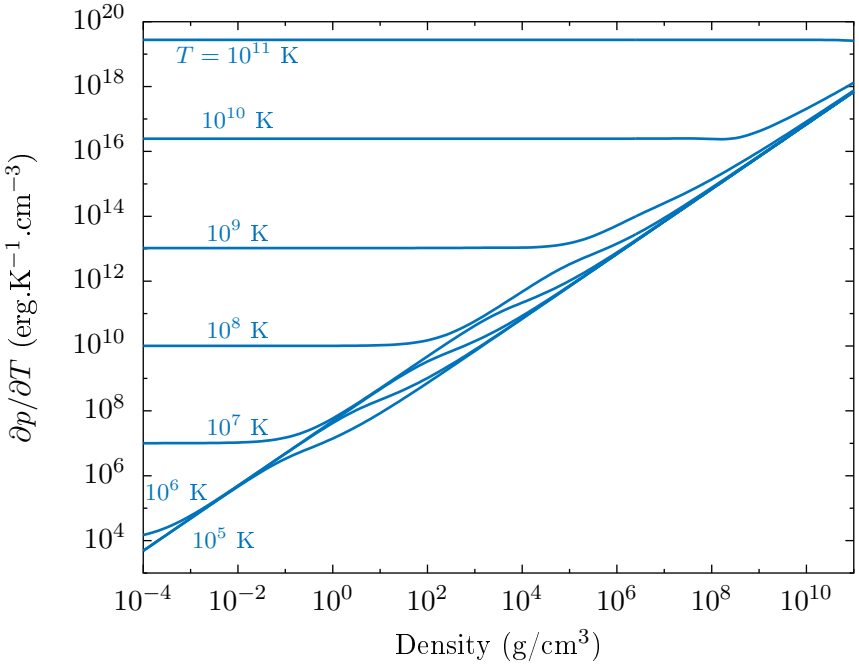

Figure A.5: Partial derivative of the pressure with respect to the temperature for different constant values of density.

$$\frac{\partial u}{\partial T} = T\frac{\partial s}{\partial T} \tag{A.56}$$

$$\frac{\partial s}{\partial \rho} = -\frac{1}{\rho^2}\frac{\partial p}{\partial T} \tag{A.57}$$

are satisfied. An equation of state is thermodynamically consistent if all these three

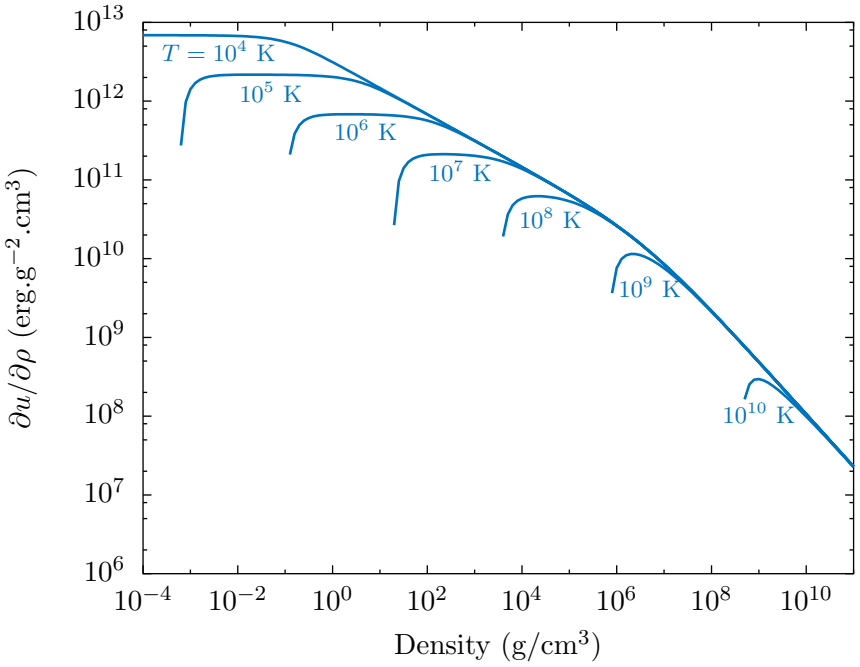

Figure A.6: Partial derivative of the specific internal energy with respect to the density for different constant values of temperature

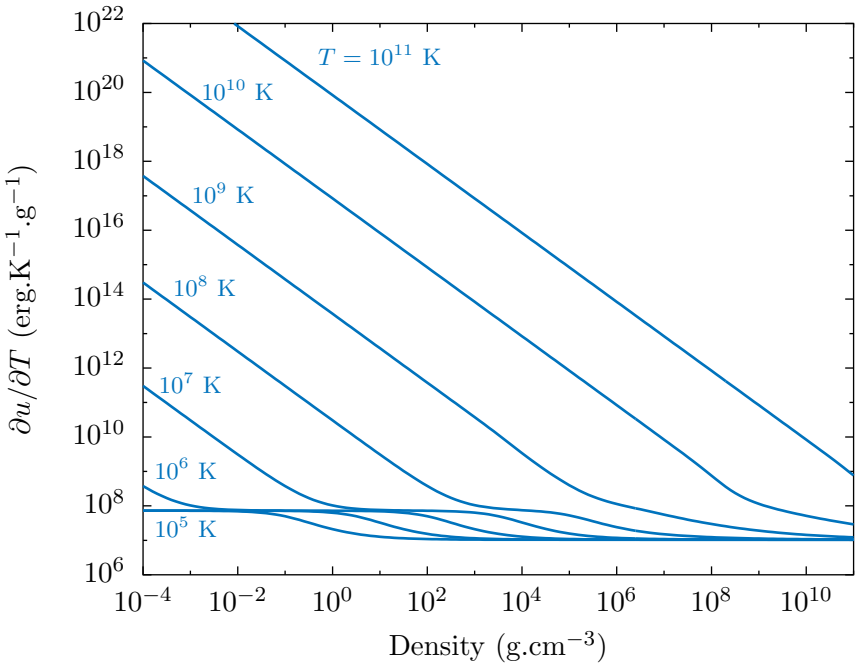

Figure A.7: Partial derivative of the specific internal energy with respect to the temperature for different constant values of density.

identities are true.

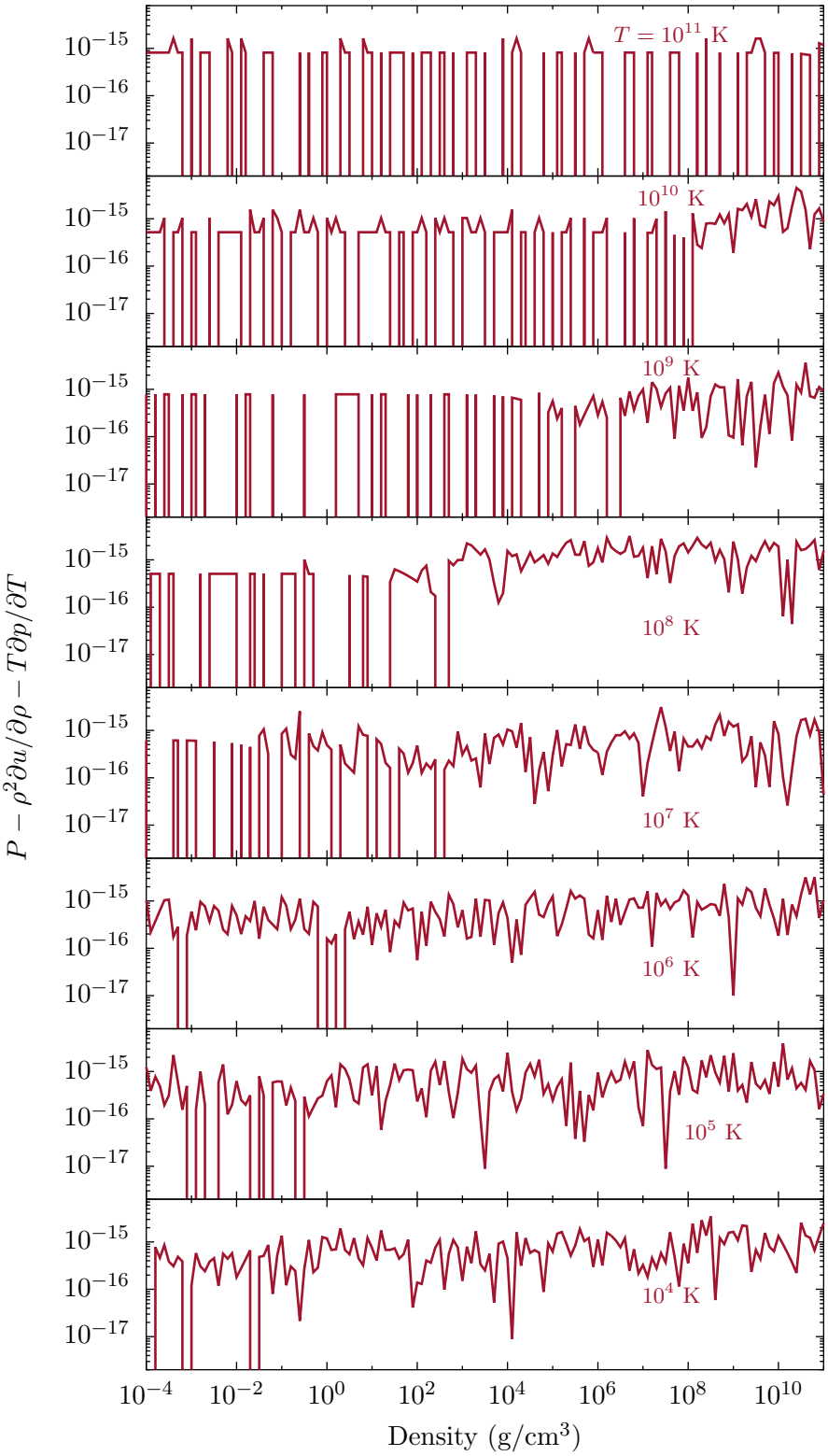

Figure A.8: Numerical deviation of the thermodynamic relation $P = \rho^2 \partial u/\partial \rho + T \partial p/\partial T$. The smaller the deviation, with zero deviation being the perfect case, the closer the equation of state comes to satisfying thermodynamic consistency.

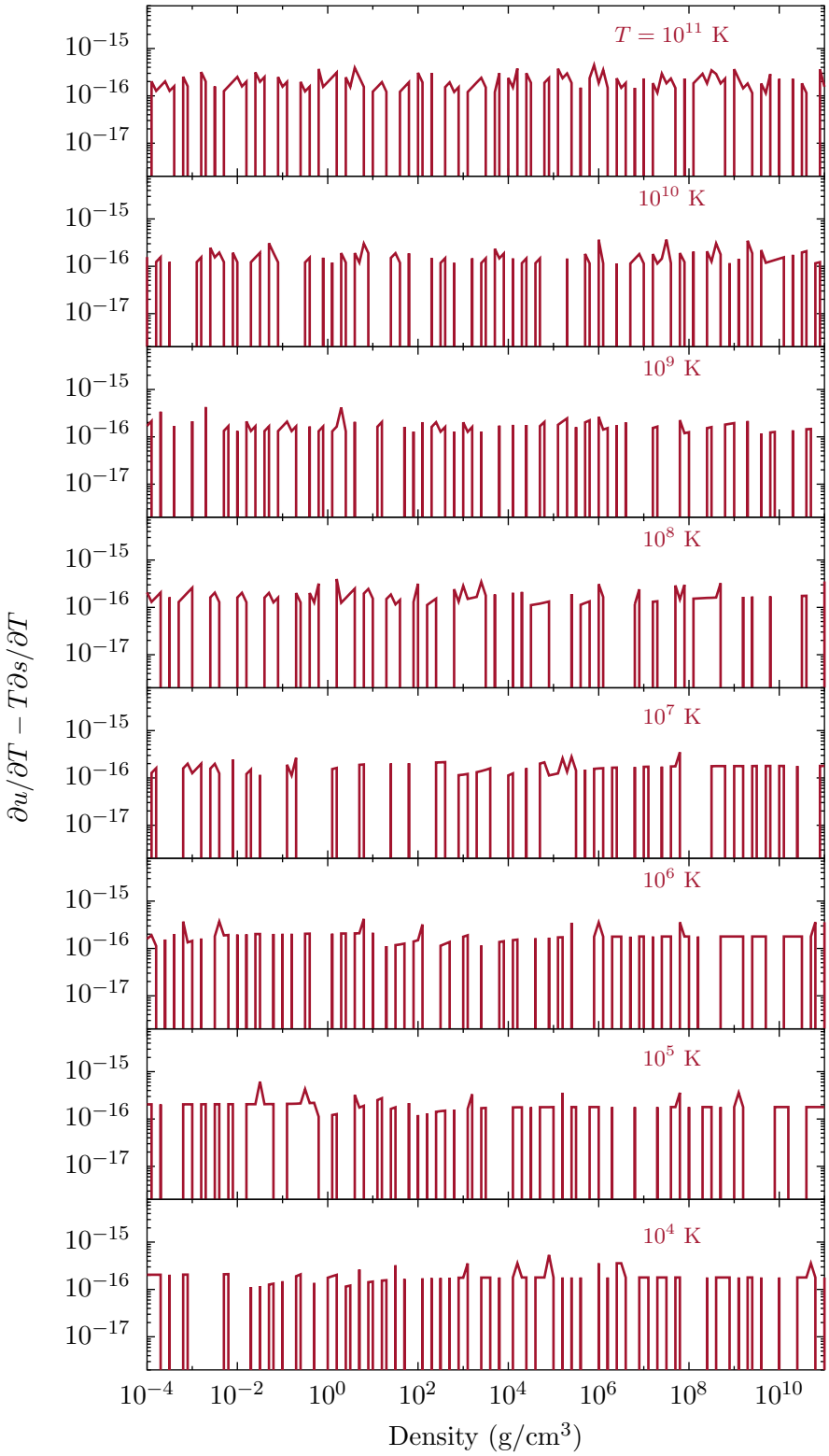

Figure A.9: Numerical deviation of the thermodynamic relation $\partial u/\partial T = T\partial s/\partial T$.

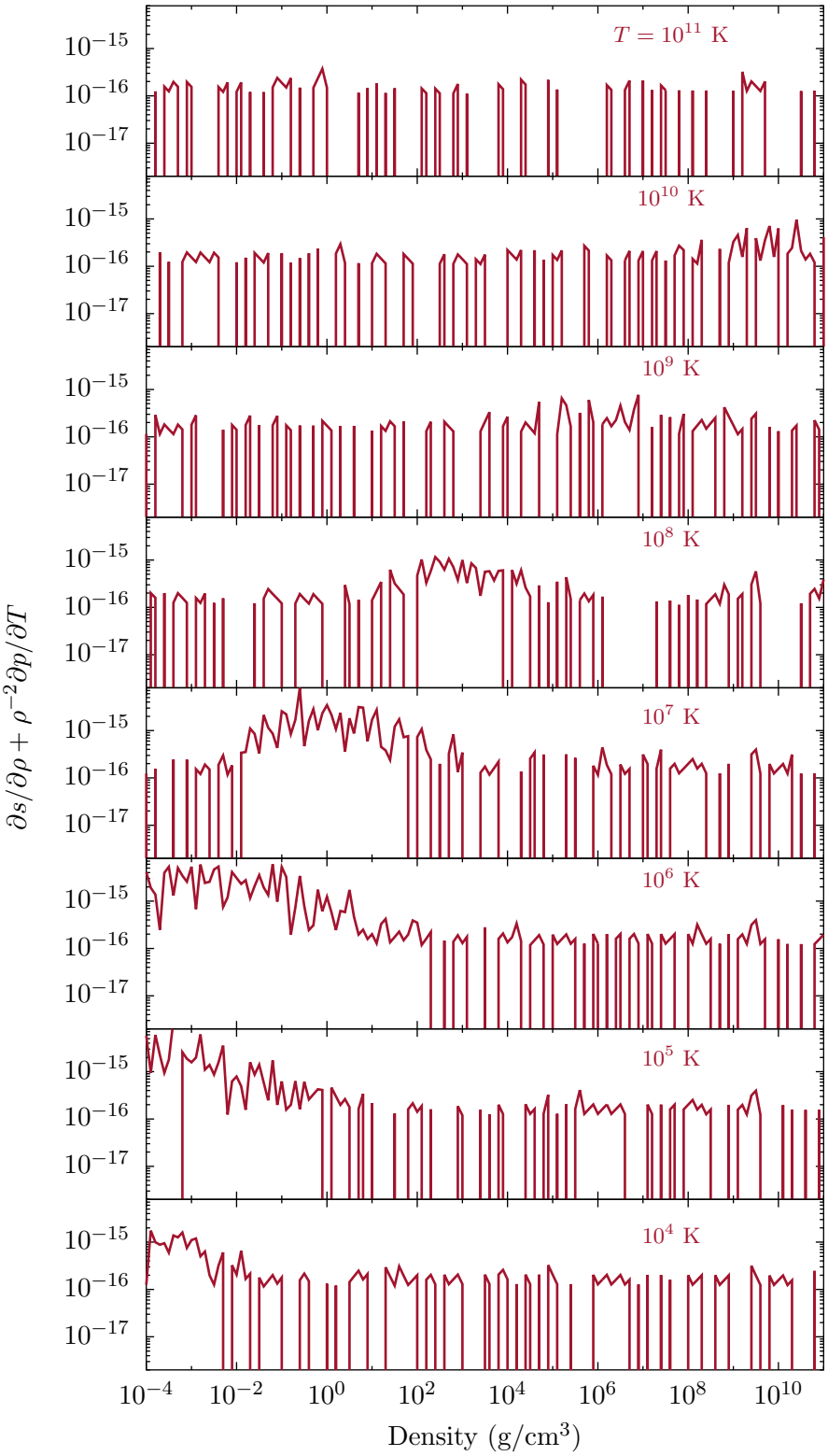

Figure A.10: Numerical deviation of the thermodynamic relation $\partial s/\partial\rho = -\rho^{-2}\partial p/\partial T$.